THE UNIVERSITY OF QUEENSLAND

AUSTRALIA

Frequency-Based Microwave Medical Imaging Techniques

Ali Zamani

B.Sc. (Electronic Eng.), M.Sc. (Electrical Eng.)

A thesis submitted for the degree of Doctor of Philosophy at

The University of Queensland in 2017

School of Information Technology and Electrical Engineering

Abstract

Medical imaging is an important technique in diagnosis and monitoring of a variety of diseases by providing a visual representation of inner organs of the human body. Although existing imaging technologies like Magnetic Resonance Imaging (MRI) and Computational Tomography (CT) can provide high resolution and accurate images, they are still expensive, bulky and time-consuming; and hence, they are not accessible in rural, remote health centres and emergency units such as ambulances. This lack of sufficient imaging tools causes millions of death each year; and therefore, a low-cost, portable, non-invasive and fast imaging device that can be used as a diagnostic and monitoring tool is deemed beneficial.

In this thesis, a study on the development and use of microwave imaging systems for medical applications has been carried out. The study focuses on the development of an imaging algorithm to create images of the human body interior for medical applications. In addition, different techniques to tackle the challenges in microwave medical imaging algorithms are proposed.

A fast frequency-based imaging algorithm is proposed in this thesis to mitigate problems associated with time-domain approaches. This method applies Bessel functions in frequency domain for fast image processing that maps regions of high dielectric contrasts of the imaged domain in a two-dimensional plane. In this algorithm, the Nyquist concept is adopted to reduce the number of sampling frequency utilising limited number of antennas to lower the computational complexity effectively whilst attaining correct detections.

Moreover, a hybrid clutter removal technique to eliminate the effect of strong reflections from the skin on the collected signals in microwave medical imaging systems is developed as a prepossessing technique to the imaging algorithm.

As the efficacy of the imaging algorithm relies on a priori information on the permittivity and boundary of the imaging domain, an antenna-specific permittivity estimation method and a boundary estimation technique by using antenna resonant frequency shifts are proposed to improve the detection accuracy and image quality. In addition, the concept of virtual antenna array to increase the effective number of antenna elements is proposed in this thesis.

The performance of the imaging algorithm and the other proposed techniques are tested via full-wave electromagnetic simulations and experiments on phantoms and healthy human trials, using the head and torso imaging systems developed in the Microwave Imaging Group of the University of Queensland.

Declaration by author

This thesis is composed of my original work, and contains no material previously published or written by another person except where due reference has been made in the text. I have clearly stated the contribution by others to jointly-authored works that I have included in my thesis.

I have clearly stated the contribution of others to my thesis as a whole, including statistical assistance, survey design, data analysis, significant technical procedures, professional editorial advice, financial support and any other original research work used or reported in my thesis. The content of my thesis is the result of work I have carried out since the commencement of my higher degree by research candidature and does not include a substantial part of work that has been submitted to qualify for the award of any other degree or diploma in any university or other tertiary institution. I have clearly stated which parts of my thesis, if any, have been submitted to qualify for another award.

I acknowledge that an electronic copy of my thesis must be lodged with the University Library and, subject to the policy and procedures of The University of Queensland, the thesis be made available for research and study in accordance with the Copyright Act 1968 unless a period of embargo has been approved by the Dean of the Graduate School.

I acknowledge that copyright of all material contained in my thesis resides with the copyright holder(s) of that material. Where appropriate I have obtained copyright permission from the copyright holder to reproduce material in this thesis and have sought permission from co-authors for any jointly authored works included in the thesis.

Publications during candidature

Peer-reviewed Journal Papers:

1. **A. Zamani**, A.M. Abbosh, “Estimation of Frequency Dispersive Complex Permittivity Seen by Each Antenna for Enhanced Multistatic Radar Medical Imaging,” *IEEE Transactions on Antennas and Propagation*, vol. 65, no. 07, 2017.
2. S.A. Rezaeieh, **A. Zamani**, K.S. Bialkowski, A.M. Abbosh, “Novel Microwave Torso Scanner for Thoracic Fluid Accumulation Diagnosis and Monitoring*,” Nature Scientific Reports*, vol. 7, no. 304, 2017.
3. **A. Zamani**, A.M. Abbosh, S. Crozier, “Multistatic Biomedical Microwave Imaging Using Spatial Interpolator for Extended Virtual Antenna Array,” *IEEE Transactions on Antennas and Propagation*, vol. 65, no. 3, pp. 1121-1130, March 2017.
4. **A. Zamani**, A. Mobashsher, A.M. Abbosh, “Fast Frequency-Based Multistatic Microwave Imaging Algorithm with Application to Brain Injury Detection,” *IEEE Transactions on Microwave Theory and Technique*, vol. 64, no. 2, pp. 653-662, Feb. 2016.
5. S.A. Rezaeieh, K.S. Bialkowski, **A. Zamani**, A.M. Abbosh, “Loop-Dipole Composite Antenna for Wideband Microwave-Based Medical Diagnostic Systems with Verification on Pulmonary Edema Detection,” *IEEE Antennas and Wireless Propagation Letters*, vol. 15, no. 1, pp. 838-841, Dec. 2016.
6. **A. Zamani**, and A.M. Abbosh, “Hybrid Clutter Rejection Technique for Improved Microwave Head Imaging,” *IEEE Transactions on Antennas and Propagation*, vol. 63, no. 11, pp. 4921-4931, Nov. 2015.
7. **A. Zamani**, S.A. Rezaeieh and A.M. Abbosh, “Lung cancer detection using frequency domain microwave imaging (Featured),” *IET Electronics Letters*, Vol.51, No.10, pp. 740-741, 2015.
8. S.A. Rezaeieh, **A. Zamani**, K.S. Bialkowski, A.M. Abbosh, “Feasibility of Using Wideband Microwave System for Non-Invasive Detection and Monitoring of Pulmonary Edema,” *Nature Scientific Reports*, vol. 5, no. 14047, 2015.
9. S.A. Rezaeieh, **A. Zamani**, K.S. Bialkowski, A.M. Abbosh, “Foam Embedded Wideband Antenna Array for Early Congestive Heart Failure Detection with Tests Using Artificial Phantom with Animal Organs,” *IEEE Transactions on Antennas and Propagation*, vol. 63, no. 11, pp. 5138-5143, Nov. 2015.

10. S.A. Rezaeieh, **A. Zamani**, K.S. Bialkowski, A.M. Abbosh, “Unidirectional Slot-Loaded Loop Antenna with Wideband Performance and Compact Size for Congestive Heart Failure Detection,” *IEEE Transactions on Antennas and Propagation*, vol. 63, no. 10, pp. 4557-4562, Oct. 2015.
11. S.A. Rezaeieh, **A. Zamani** and A.M. Abbosh, “Three Dimensional Wideband Antenna for Head Imaging System with Performance Verification in Brain Tumor Detection,” *IEEE Antennas and Wireless Propagation Letters*, Vol. 14, pp. 901-914, 2015.
12. S.A. Rezaeieh, A.M. Abbosh, **A. Zamani**, K. Bialkowski, “Pleural effusion detection system using wideband slot-loaded loop antenna,” *Electronics Letters*, Vol. 51, No. 15, pp. 1144-1146, 2015.

Conference papers:

1. **A. Zamani**, A.M. Abbosh, “Permittivity Estimation for Improved Microwave Medical Imaging,” *2017 IEEE Symposium on Antennas and Propagation and Radio Science Meeting*, San Diego, CA, Jul. 9-14, 2017.
2. **A. Zamani**, A.M. Abbosh, “Surface Estimation of Imaged Object in Microwave Medical Imaging,” *2017 IEEE Symposium on Antennas and Propagation and Radio Science Meeting*, San Diego, CA, Jul. 9-14, 2017.
3. **A. Zamani**, S.A. Rezaeieh and A.M. Abbosh, “Improved Microwave Medical Imaging Using Virtual Antenna Array,” *2016 IEEE International Conference on Electromagnetics in Advanced Applications (ICEAA)*, Cairns, QLD, Sep. 19-23, 2016, pp. 652-654.
4. **A. Zamani**, A.M. Abbosh, “Frequency Domain Hybrid Artifact Removal Technique for Multistatic Microwave Head Imaging,” *2015 IEEE International Symposium on Antennas and Propagation (ISAP)*, Hobart, TAS, Nov. 9-12, 2015, pp. 1-3.
5. **A. Zamani**, A.M. Abbosh, “Clutter Rejection Techniques for Microwave Head Imaging,” *2015 IEEE International Symposium on Antennas and Propagation (ISAP)*, Hobart, TAS, Nov. 9-12, 2015, pp. 1-4.
6. A.M. Abbosh, **A. Zamani**, A.T. Mobashsher, “Real-time Frequency-Based Multistatic Microwave Imaging for Medical Applications (Invited),” *2015 IEEE MTT-S 2015 International Microwave Workshop Series on RF and Wireless Technologies for Biomedical and Healthcare Applications (IMWS-BIO)*, Taipei, 2015, pp. 127-128.
7. **A. Zamani** and A.M. Abbosh, “Fast Multistatic Technique for Microwave Brain Imaging,” *2015 IEEE International Symposium on Antennas and Propagation & USNC/URSI National Radio Science Meeting*, Vancouver, BC, 2015, pp. 536-537.

8. **A. Zamani**, A.T. Mobashsher, B.J. Mohammed, and A.M. Abbosh, “Microwave Imaging Using Frequency Domain Method for Brain Stroke Detection,” *2014 IEEE MTT-S International Microwave Workshop Series on RF and Wireless Technologies for Biomedical and Healthcare Applications (IMWS-Bio2014)*, London, 2014, pp. 1-3.
9. **A. Zamani**, S.A. Rezaeieh and A.M. Abbosh, “Frequency domain method for early stage detection of congestive heart failure,” 2014 IEEE MTT-S International Microwave Workshop Series on RF and Wireless Technologies for Biomedical and Healthcare Applications (IMWS-Bio2014), London, 2014, pp. 1-3.

Publications included in this thesis

A. Zamani, A. Mobashsher, A.M. Abbosh, “Fast Frequency-Based Multistatic Microwave Imaging Algorithm with Application to Brain Injury Detection,” *IEEE Transactions on Microwave Theory and Technique*, vol. 64, no. 2, pp. 653-662, Feb. 2016. Various parts of the paper are incorporated in Chapter 3 to Chapter 7.

Contributor	Statement of contribution
A. Zamani (Candidate)	Designed imaging algorithm (90%) Designed experiments (30%) Wrote and edited the paper (60%)
A. Mobashsher	Designed experiments (50%) Designed Antennas (100%)
A.M. Abbosh	Designed imaging algorithm (10%) Designed experiments (20%) Wrote and edited the paper (40%)

A. Zamani, A.M. Abbosh, “Estimation of Frequency Dispersive Complex Permittivity Seen by Each Antenna for Enhanced Multistatic Radar Medical Imaging,” *IEEE Transactions on Antennas and Propagation*, vol. 65, no. 07, 2017. This paper is incorporated in Chapter 6.

Contributor	Statement of contribution
A. Zamani (Candidate)	Designed algorithm (90%) Designed experiments (80%) Wrote and edited the paper (60%)
A.M. Abbosh	Designed algorithm (10%) Designed experiments (20%) Wrote and edited the paper (40%)

A. Zamani, A.M. Abbosh, S. Crozier, “Multistatic Biomedical Microwave Imaging Using Spatial Interpolator for Extended Virtual Antenna Array,” *IEEE Transactions on Antennas and Propagation*, vol. 65, no. 3, pp. 1121-1130, March 2017. This paper is incorporated in Chapter 5.

Contributor	Statement of contribution
A. Zamani (Candidate)	Designed algorithm (90%) Designed experiments (80%) Wrote and edited the paper (40%)
A.M. Abbosh	Designed algorithm (10%) Designed experiments (10%) Wrote and edited the paper (40%)
S. Crozier	Designed experiments (10%) Wrote and edited the paper (20%)

A. Zamani, and A.M. Abbosh, “Hybrid Clutter Rejection Technique for Improved Microwave Head Imaging,” *IEEE Transactions on Antennas and Propagation*, vol. 63, no. 11, pp. 4921-4931, Nov. 2015. This paper is incorporated in Chapter 4.

Contributor	Statement of contribution
A. Zamani (Candidate)	Designed the imaging algorithm (90%) Designed experiments (80%) Wrote and edited the paper (60%)
A.M. Abbosh	Designed the imaging algorithm (10%) Designed experiments (20%) Wrote and edited the paper (40%)

A. Zamani, S.A. Rezaeieh and A.M. Abbosh, “Lung cancer detection using frequency domain microwave imaging (Featured),” *IET Electronics Letters*, Vol.51, No.10, pp. 740-741, 2015. Various parts of the paper are incorporated in Chapter 3, 6 and 7.

Contributor	Statement of contribution
A. Zamani (Candidate)	Designed the imaging algorithm (90%) Designed experiments (40%) Wrote and edited the paper (40%)
S.A. Rezaeieh	Designed experiments (50%) Wrote and edited the paper (20%)
A.M. Abbosh	Designed the imaging algorithm (10%) Designed experiments (10%) Wrote and edited the paper (40%)

Contributions by others to the thesis

I acknowledge the contributions by others to this thesis. Prof. Amin Abbosh as the main supervisor contributed closely in defining the research problem, revising, and directing the thesis. All the antennas and imaging platforms utilised in this thesis are designed partly by Dr. Toaha Ahmed Mobashsher and in a wider scope by Dr. Sasan Ahdi Rezaeieh. Dr. Konstanty Bialkowski contributed in hardware implementations and the design of experiments.

Statement of parts of the thesis submitted to qualify for the award of another degree

“None”

Research Involving Human or Animal Subjects

To analyse the performance of the proposed method in Chapter 7, it is tested on healthy subjects using the torso imaging system explained in Chapter 6. All of the tests were conducted in accordance with the guidelines and protocols approved by the “University of Queensland Human Research Ethics Committee A” with the approval number of “2017000185”.
A copy of the ethics approval letter is included in the appendix 1 of this thesis.

Acknowledgements

This thesis presents not only my work; it is a milestone in more than one decade of work at UQ microwave research group. I am very grateful for the chance that was given to me to do my PhD studies at this group. Undertaking this PhD would not have been possible to do for me without the support and guidance that I received from many people and institutes.
I would like to first thank my Principal Advisor, Prof. Amin Abbosh, for his constant guidance, encouragement and support, without which this work would not have been possible.
I am also grateful to my friends, co-workers, and office-mates that made life at the university as good as it could be.
Last but not the least, I would like to thank my parents and my brother and sister for supporting me spiritually throughout my PhD and my life in general.

Financial support

I gratefully acknowledge the financial supports received towards my PhD from Australian Government through the Australian Endeavour Postgraduate Scholarship. I am also grateful to the funding received from the University of Queensland to undertake my PhD.

Keywords

Microwave imaging, medical imaging, head scanner, torso scanner, brain stroke, pulmonary oedema, radar-based Imaging, beamforming.

Australian and New Zealand Standard Research Classifications (ANZSRC)

ANZSRC code: 090699, Electrical and Electronic Engineering not elsewhere classified, 70%

ANZSRC code: 090399, Biomedical Engineering not elsewhere classified, 30%

Fields of Research (FoR) Classification

FoR code: 0906, Electrical and Electronic Engineering, 70%

FoR code: 0903 Biomedical Engineering, 30%

CONTENTS

1 INTRODUCTION 19
1.1 BACKGROUND AND MOTIVATION 19
1.2 MICROWAVE MEDICAL IMAGING 20
1.3 AIM OF THE THESIS 22
1.4 ORIGINAL CONTRIBUTIONS OF THE THESIS 23
1.5 THESIS ORGANISATION 23
2 OVERVIEW OF MICROWAVE MEDICAL IMAGING ALGORITHMS 25
2.1 MICROWAVE IMAGING TECHNIQUES 25
2.1.1 Microwave Tomography Technique 26
2.1.2 Microwave Beamforming Technique 27
2.2 CHALLENGES IN THE DEVELOPMENT OF A MICROWAVE MEDICAL IMAGING ALGORITHM 30
2.3 SUMMARY 31
3 FAST FREQUENCY-BASED MICROWAVE IMAGING TECHNIQUE 32
3.1 PROPOSED IMAGING ALGORITHM 33
3.2 ALGORITHM VALIDATION 38
3.2.1 Simulation Results 38
3.2.2 Experimental Results 43
3.3 ALGORITHM ACCELERATION 46
3.4 COMPARISON 49
3.5 LUNG CANCER DETECTION USING MONOSTATIC TORSO ROTATION SYSTEM 51
3.6 SUMMARY 54
4 CLUTTER REMOVAL TECHNIQUES 55
4.1 CONVENTIONAL CLUTTER REMOVAL TECHNIQUES 55
4.2 MULTILAYER REFLECTIONS 57
4.3 CLUTTER REMOVAL METHODS IN FREQUENCY-DOMAIN 60
4.3.1 Average Subtraction 60
4.3.2 Differential approach (DA) type A 61
4.3.3 Differential approach (DA) type B 61
4.3.4 Spatial Filtering 62
4.3.5 Entropy-based Filtering 62
4.4 METHODS COMPARISON 63

4.5 PROPOSED HYBRID METHOD 68
4.6 EXPERIMENTAL VALIDATION 71
4.7 SUMMARY 73
5 IMPROVED RADAR-BASED MICROWAVE MEDICAL IMAGING USING EXTENDED VIRTUAL ANTENNA ARRAY 74
5.1 VIRTUAL ARRAY CONCEPT 75
5.1.1 Statistical Model 76
5.1.2 Correlation Function Design 77
5.2 MODEL VALIDATION 80
5.2.1 Simulations 80
5.2.2 Experiments 88
5.3 COMPARISON 89
5.4 SUMMARY 91
6 PERMITTIVITY ESTIMATION AS A PRIORI FOR MICROWAVE MEDICAL IMAGING 92
6.1 PERMITTIVITY ESTIMATION TECHNIQUES: LITERATURE REVIEW 93
6.2 PERMITTIVITY ESTIMATION FROM THE VIEW POINT OF EACH ANTENNA 94
6.3 VERIFICATION 98
6.3.1 Simulations 102
6.3.2 Experiments 109
6.4 SUMMARY 111
7 SURFACE ESTIMATION OF IMAGED OBJECT FOR IMPROVED MICROWAVE MEDICAL IMAGING 112
7.1 SURFACE ESTIMATION USING ANTENNA RESONANT FREQUENCY SHIFT 113
7.2 VALIDATION AND RESULTS 118
7.2.1 Simulations 118
7.2.2 Human Test Results 123
7.3 COMPARISON 125
7.4 SUMMARY 127
8 CONCLUSION 128
9 REFERENCES 131
10 APPENDICES 141

LIST OF TABLES

Table 3.1. Image quality in the two simulated configurations. 43

Table 3.2. Effect of number of samples on the image quality 47

Table 3.3. Performance comparison between proposed, multi-DAS and MAMI methods 51

Table 4.1. Comparison between performance of the proposed and other techniques 71

Table 5.1 . Image quality of the simulated results 85

Table 5.2 . Mutual information between neighbouring antenna elements 87

Table 5.3 . Comparison of image quality 90

Table 6.1. Computation time for different number of samples 100

Table 6.2. Image quality using conventional and proposed methods 109

Table 7.1. Image quality without and with boundary detection using the proposed method 121

Table 7.2. Boundary estimation errors using matched-filter and proposed methods 126

LIST OF FIGURES

Fig. 1.1. Dielectric properties of different tissues at low microwave frequencies. 21

Fig. 1.2. Microwave imaging system schematic. 21

Fig. 2.1. Block diagram of delay-and-sum (DAS) algorithm 28

Fig. 2.2. Block diagram of microwave imaging via space-time (MIST) beamforming algorithm [40] 29

Fig. 2.3. Block diagram of wideband adaptive beamforming algorithm [46] 30

Fig. 3.1. Incident and scattered electric fields in the imaged domain. 34

Fig. 3.2. Block diagram of fast frequency-based microwave imaging algorithm 37

Fig. 3.3. The designed antenna (a) top and (b) side views. Dimensions in (mm) 39

Fig. 3.4. Reflection coefficient of the antenna. 39

Fig. 3.5. Simulation setup using (a) 12-antenna and (b) 8-antenna arrays. 40

Fig. 3.6. Reconstructed images from the simulation environment for unhealthy scenario with 12-antenna array, (a) before and (b) after clutter removal; 8-antenna array, (c) before and (d) after clutter removal; healthy scenario with 8-antenna array, (e) before and (f) after clutter removal. Squares in (a) to (d) show the exact location of the brain injury. 41

Fig. 3.7. Measurement platform indicating 1) realistic head phantom, 2) antenna array 3) measuring platform, 4) microwave transceiver, 5) switch matrix, 6) PC. 44

Fig. 3.8. Photograph of the internal structure of the fabricated 3D realistic human head [60]. 1) Exterior section, 2) spinal cord 3) cerebellum, 4) white matter, 5) Dura, 6) grey matter, 7) CSF. 44

Fig. 3.9. (a, b) Relative permittivity and (c, d) conductivity comparisons of actual and developed head tissues [59]. 45

Fig. 3.10. Experimental results of (a) 2 × 2 × 2 cm3 and (b) 2 × 1 × 1 cm3 bleeding in the head phantom. Black rectangles show exact location of target. 46

Fig. 3.11. The resultant images from experiments using (a) 360, (b) 100, (c) 60, (d) 34, (e) 25 and (f) 15 frequency samples. Black squares are exact location. 48

Fig. 3.12. Reconstructed image of the indicated brain injury for (a) measured data and (b) simulation, using 34 frequency samples. 49

Fig. 3.13. Comparison of reconstructed images using (a) multi-DAS, (b) MAMI. The images on the left side are for measured data and images on the right are for simulated. Black squares illustrate the actual location of the target. 50

Fig. 3.14. Monostatic torso rotation microwave-based imaging system 52

Fig. 3.15. (a) The utilised torso phantom with its inner organs, and (b) the tumour. 52

Fig. 3.16. Assumed imaged domain for monostatic torso rotation system. 53

Fig. 3.17. Imaging results of the torso for (a) infected lung with cancer and (b) healthy lung. Black square shows the exact location of the tumour. 53

Fig. 4.1. Electromagnetic reflections from different head tissue layers using (a) simulations and (b) a simplified diagram. (c) Model of the multilayer head outer layers. 58

Fig. 4.2. PSF, spatial domain signals and corresponding normalised cross-correlation values for (a) reference signal, (b) raw signal, and after using (c) average subtraction, (d) differential approach-A, (e) differential approach-B, (f) spatial filtering, and (g) entropy-based filtering. The vertical red dashed line shows the exact location of the target. 66

Fig. 4.3. Reconstructed images (a) without applying clutter removal techniques, and after using (b) average subtraction, (c) differential approach-A, (d) differential approach-B, (e) spatial filtering, and (f) entropy-based filtering. Black rectangles show the exact location of the target. 67

Fig. 4.4. (a) PSF, typical spatial domain signal and average value of normalised cross-correlation, and (b) reconstructed image, using the hybrid method. Black rectangles show the exact location of the target. 70

Fig. 4.5. Experimental results using (a) the proposed hybrid method, (b) average subtraction, (c) differential approach-A, (d) differential approach-B, (e) spatial filtering, and (f) entropy-based filtering. Black rectangles show the exact location of the target. Left side images are for 2 × 2 × 2 cm3 bleeding in the head phantom and right side images are for 2 × 1 × 1 cm3. Black squares show the exact location of the bleeding. 72

Fig. 5.1. Wave propagation in a round-shaped microwave imaging system. 76

Fig. 5.2 . S-Parameters of real and virtual 12-antenna arrays. 81

Fig. 5.3. Estimation error for the extended 12-antenna array from 8-element array. 82

Fig. 5.4. Reconstructed images for shallow target, deep target and healthy scenarios using frequency-based imaging method with (a) real 8-element array, and virtual (b) 12, (c) 16, and (d) 32 elements. Black squares show the exact location of bleeding. 83

Fig. 5.5. Image intensity variation range for unhealthy and healthy cases. 84

Fig. 5.6. Reconstructed images using (a) real 12-element array and (b) virtual 12-element array using data from a real 8-element array. 85

Fig. 5.7. Reconstructed images from (a) real six-element array with virtual (b) 8, (c) 12, and (d) 16-element arrays. 86

Fig. 5.8. Reconstructed images from (a) real four-element array with virtual (b) 8, (c) 12, and (d) 16-element arrays. 86

Fig. 5.9. Reconstructed images from experimental data, using (a) real eight-element array, and (b) virtual 16-element array. Left images are related to the 2 × 2 × 2 cm3 and right images are related to the 2 × 1 × 1 cm3 bleeding target. Black rectangles show exact location of target. 89

Fig. 5.10. Reconstructed images for shallow target, deep target and healthy scenarios using (a) frequency-based imaging method with virtual 12-element array extracting from 8 real antenna array and (b) multistatic back-projection technique with real 8-element array. 90

Fig. 6.1. The used imaging domain. 94

Fig. 6.2. Flowchart of the proposed method, (a) training and (b) imaging. 97

Fig. 6.3. Training setup. 98

Fig. 6.4. (a) The utilised antenna [25], and (b) its reflection coefficient. 98

Fig. 6.5. Estimation error with number of antennas 99

Fig. 6.6. Estimation error against sampling size, for (a) relative permittivity and (b) conductivity. 101

Fig. 6.7. (a) Dielectric properties of the training samples along with the ranges of variations for dielectric parameters of human torso tissues (coloured boxes), and (b) variation of relative permittivity (solid lines) and conductivity (dash lines) with frequency. 102

Fig. 6.8. Simulation setup to image an object (human torso), (a) side view and (b) cross-section up view. 103

Fig. 6.9. Estimated dielectric properties at 1 GHz for each antenna. (a) Relative permittivity, and (b) conductivity. 104

Fig. 6.10. Estimated dielectric properties for antenna 1 and 4 over the used frequency band. (a) Relative permittivity, and (b) conductivity. 105

Fig. 6.11. Reconstructed images (a), (b) before, and (c), (d) after permittivity estimation. 108

Fig. 6.12. Torso scanner opened to show its structure and then enclosing a torso phantom. 110

Fig. 6.13. Resultant image from experiment. 111

Fig. 7.1. (a) Calculated resonant frequency of an antenna operating in the dipole mode with antenna-ground plane distance, and (b) zoomed-in plot of (a) to include the distances of interest in microwave torso imaging. 115

Fig. 7.2. Measured resonant frequency of antenna operating in the dipole mode with antenna-torso distance for the practical distances used in torso imaging. 116

Fig. 7.3. Scattering parameters of the imaging antenna when facing the imaged object located at different distances. 118

Fig. 7.4. The distance between the antenna and skin as a function of resonance frequency. 119

Fig. 7.5. Constructed surface with (a) 12 real antennas, (b) 24, and (c) 36, virtual antennas. Blue solid lines show the estimated boundary location; red dashed lines show the exact boundary of the torso and green squares show the location of the antennas. 120

Fig. 7.6. Reconstructed images (a), (b) without, and (c), (d) with boundary estimation. 122

Fig. 7.7. Torso scanner system. 123

Fig. 7.8. Constructed surfaces for human subjects. 124

Fig. 7.9. Comparison between the estimated and exact distances in experiments. 124

Fig. 7.10. Estimated torso boundary by matched-filter method (blue solid line), using 12 antennas and proposed method (red dashed line), using 24 virtual antennas extracted from 12 antennas. Grey dotted line shows the exact boundary of the torso. 125

Fig. 7.11. Estimated torso boundary by matched-filter method (blue solid line), and proposed method (red dashed line). Grey dotted line shows the exact boundary of the torso. 126

LIST OF ABBREVIATIONS AND ACRONYMS

2D	Two Dimensional
3D	Three Dimensional
CST	Computer Simulation Technology
CT	Computed Tomography
DA	Differential Approach
DAS	Delay And Sum
DOF	Degree of Freedom
EMF	Electro-Motive Force
FIR	Finite Impulse Response
HFSS	High Frequency Structure Simulator
ICC	Information Correlation Coefficient
MAMI	Multistatic Adaptive Microwave Imaging
MIST	Microwave Imaging via Space-Time
MRI	Magnetic Resonance Imaging
MUSIC	Multiple Signal Classification
MVDR	Minimum Variance Distortion-less Response
PC	Personal Computer
PSF	Point Spread Function
PVC	Polyvinyl chloride
RF	Radio Frequency
SNR	Signal to Noise Ratio
S-parameters	Scattering Parameters
ToF	Time-of-Flight
TSS	Total Sum of Squares
USB	Universal Serial Bus
UWB	Ultra Wide Band
VNA	Vector Network Analyser
WHO	World Health Organization

1 INTRODUCTION

This chapter presents the underlying motivation and theoretical background of microwave medical imaging systems. The aims and original contributions of the thesis along with the organisation of the thesis are also outlined at the final section of this chapter.

1.1 Background and Motivation

Medical Imaging is an effective technique in diagnosis and treatment of a variety of diseases by providing a visual representation of inner organs of the human body. Many surgical interventions can be avoided by utilising diagnostic imaging devices. Medical Imaging can also be used as an assessment tool to monitor treatment effectivity for a diagnosed disease. Therefore, medical imaging is crucial for initiatives to enhance public health for all population groups and at all levels of health care.

Different medical imaging technologies such as ultrasound, computed tomography (CT), magnetic resonance imaging (MRI) and nuclear medicine imaging have developed since last century. However, despite their supreme performances in terms of image resolution and accuracy, these are expensive medical equipment, and hence not available at rural and remote health centres. According to the World Health Organisation (WHO), more than half of the world's population does not have access to diagnostic imaging [1]. Furthermore, there is a high demand on a low-cost and safe imaging system for the detection and continuously monitoring of a variety of diseases. For example, over one million deaths globally each year are caused primarily by lung cancer, which makes it by far the number one cancer killer in the world [2], and unfortunately, to date there is no reliable and affordable screening tool to early diagnose those diseases. In addition, due to the limited permissible exposed dose, most of the existing imaging systems cannot be used frequently by some

patient groups such as pregnant women and children. Consequently, they are not recommended for the follow-up of the diseases that require activity monitoring on a regular short-term basis like torso monitoring of patients with acute lung injuries such as pneumothorax, lung cancer, and pleural effusion that should be performed at least on a daily basis [3].

Furthermore, the conventional imaging tools are not helpful when urgent diagnosis is required. For example, in case of brain injuries fast diagnosis is essential to save the patient. Severe brain injuries include traumatic and acquired brain injuries, which are respectively caused by external forces (like fall or accident) or internal incidences (like stroke and tumours) [4]. It is well known that a patient with brain injury requires immediate medical attention. From the onset of the brain injury, millions of brain cells die every second causing permanent damages, which can even lead to death [4]. Thus, a fast and portable diagnosis system is required on the spot for rapid diagnosis of such injuries.

The underlying motivation of this thesis is to fill the recognised gap by utilising microwave-based imaging techniques as a low-cost, compact, safe, and fast approach in the diagnosis and monitoring of different diseases such as brain stroke, lung cancer, and pleural effusion.

1.2 Microwave Medical Imaging

Microwave imaging is an attractive technique for medical applications that has the potential to create a visual representation of the interior of the human body in a cost-effective and safe manner. The significant difference between the dielectric properties of injured and healthy tissues of the human body at microwave frequencies represents the basis of microwave medical imaging. Fig. 1.1 shows an example of the dielectric properties of the constitutive tissues of a human head [10]. This figure shows the contrast between dielectric properties of different tissues of human head at microwave frequencies. Moreover, it is clear from Fig. 1.1 that a bleeding injured tissue has the highest values of permittivity and conductivity compared to other background tissues. Other investigations on the electromagnetic properties of human tissues also show that there is a high contrast between dielectric properties of cancerous and healthy tissues [11].

When an injured tissue with high permittivity value is exposed to an electromagnetic wave at microwave frequency, a high portion of the wave reflects back to the source. Therefore, the reflected signals can be used to estimate the location and/or dielectric properties of the abnormality. To that end, a microwave imaging system is utilised to send and receive electromagnetic waves to and from the imaged object. A microwave imaging system is usually made up of a control and processing unit, microwave transceiver, switching network, and an antenna array, which surrounds the imaged object (Fig. 1.2). The antenna array is used to send electromagnetic waves at

microwave frequencies generated in the transceiver to the imaging object and capture the scattered signals, which are then processed to create two or three-dimensional images.

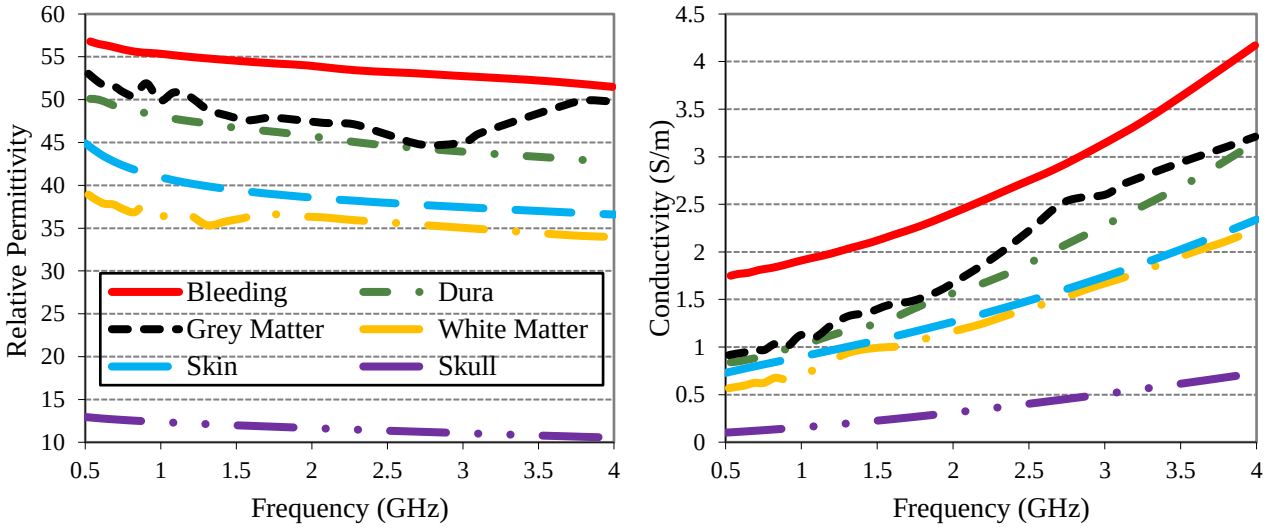

Fig. 1.1. Dielectric properties of different tissues at low microwave frequencies.

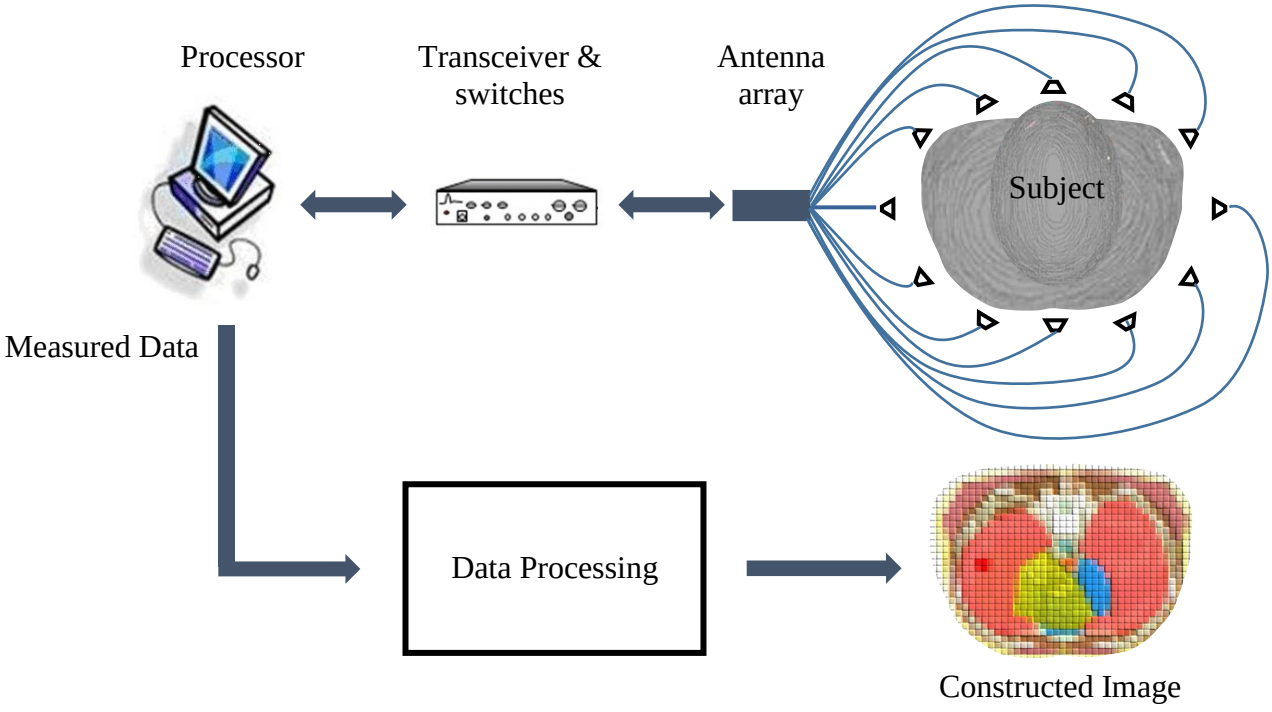

Fig. 1.2. Microwave imaging system schematic.

Study of the literature reveals that there have been extensive efforts to build portable and low-cost microwave imaging systems in recent years. However, there are still numerous challenges to be overcome in the development of a fast and accurate imaging algorithm. The imaging algorithm

plays the most important role in a microwave imaging system and this reported research is mainly focused on the development of a microwave imaging algorithm suitable for medical applications. In this work, the feasibility of using microwave imaging algorithm in medical applications is studied and based on formed conclusions, a novel frequency-based imaging algorithm is developed. Then, the challenges of using the imaging algorithm in realistic scenarios are addressed by enhancing the proposed algorithm using different techniques.

1.3 Aim of the Thesis

This project aims to develop a microwave imaging algorithm suitable for different medical applications that is fast and effectively detects the probable location of abnormalities inside the imaged object, such as human torso and head. There are several challenges that should be addressed to reach a comprehensive solution for a microwave imaging algorithm. The following steps are taken into account to successfully achieve the goals of this project:

i. **Behaviour of electromagnetic waves inside the human body**: A comprehensive study on dielectric properties of human tissues and their effects on electromagnetic waves at microwave frequencies is required in order to establish a microwave imaging algorithm.

ii. **Data acquisition setup**: Depending on the imaging object (torso or head) and imaging scenario, different platforms and data acquisition setups, including monostatic and multistatic, with circular, elliptical, or linear array configurations, are used. Array configuration, required number of antennas, operating frequency and bandwidth are the important factors in data acquisition step that should be considered before developing the image reconstruction algorithm.

iii. **Signal pre-processing**: The received signals from the data acquisition system are usually distorted due to the multilayer structure of the human body and strong reflections from the skin. In addition, in order to accurately detect an abnormality, a set of priori information on the wave's propagation speed and the boundary location of the imaged object are required. Therefore, different pre-processing techniques should be utilised to remove the signal clutter and estimate the permittivity and boundary of the imaged object.

iv. **Verification**: The proposed methods and algorithms need to be tested through simulations and experiments by using realistic human models and phantoms. In addition, in order to validate the performance of the proposed method in realistic environments, they should be tested on human subjects.

1.4 Original Contributions of the Thesis

The following original contributions are the results of the research undertaken toward addressing the aforementioned challenges:

i. Developing a fast frequency-based algorithm to mitigate problems associated with time-domain approaches.

ii. Developing a hybrid clutter-removal technique to eliminate the effect of strong reflections from the skin on the collected signals in microwave medical imaging systems.

iii. Introducing the Information Correlation Coefficient (ICC) to find the required number of antennas for medical imaging systems.

iv. Proposing the antenna-specific permittivity estimation method to enhance the performance of the microwave imaging algorithms.

v. Developing a boundary estimation technique by using antenna resonant frequency shifts to improve the detection accuracy and image quality.

vi. Theoretical analysis and simulation of electromagnetic wave behaviour in human body.

vii. Conducting full-wave electromagnetic simulations for different imaging configurations to analyse and test the proposed algorithms in different applications.

viii. Performing experimental verification of the proposed methods on different applications with different imaging platforms.

1.5 Thesis Organisation

The rest of this thesis is organised as follows:

Chapter 2 overviews the existing microwave imaging algorithms for medical applications. Current microwave-based imaging algorithms are discussed and a comparison on the advantages and disadvantages of different techniques is provided. The challenges faced by the imaging algorithms are described in this chapter.

Chapter 3 discusses the development of the proposed fast frequency-based microwave-imaging algorithm. The Nyquist theorem as a solution to accelerate the algorithm is explained in this chapter. The results of testing the proposed method on head injury and lung cancer detection are provided at the end of this chapter.

Chapter 4 overviews existing clutter removal techniques used in microwave medical imaging. The existing clutter removal techniques are modified to be used in frequency-domain and then a thorough comparison between those techniques is performed in this chapter. The chapter ends with proposing and testing a new clutter removal technique for microwave medical imaging algorithms.

Chapter 5 presents a new technique based on virtual antenna array to address the challenge of limited number of antennas in multistatic imaging modalities and to enhance the resultant images. The proposed technique is tested in head imaging system.

In Chapter 6, the permittivity estimation problem, one of the most important challenges in microwave imaging, is addressed by introducing a technique to estimate the permittivity seen by each imaging antenna. The proposed method is tested in torso imaging system with the purpose of lung cancer detection.

Chapter 7 introduces a surface estimation technique to enhance the imaging model and improve the detection accuracy and image quality of the imaging algorithm. Performance analysis of the proposed method is performed on healthy human trials at the end of this chapter.

Chapter 8 concludes the thesis with the suggestions for future works.

2 Overview of Microwave Medical Imaging Algorithms

An overview of the state-of-the-art microwave-based imaging systems utilised in medical applications is provided in this chapter. Different techniques are detailed and the challenges to be tackled for a development of a successful microwave medical imaging algorithm are described in this chapter.

2.1 Microwave Imaging Techniques

Depending on the configuration of imaging system, different imaging algorithms have been developed to extract the information from measurements of the scattered fields. There are mainly two types of configurations (monostatic and multistatic) in which one or multiple spatially diverse antennas are used as transmitters and receivers. In monostatic approach, one antenna is used as both transmitter and receiver. The antenna can be moved to different positions to obtain more information about the imaging domain. In multistatic, two or more antennas are used. In this configuration, a microwave signal is transmitted by each antenna, and in turn, the scattered signals are captured by all the antennas. This process is repeated for every antenna to record all the required signals. While the multistatic configuration is more complex than the monostatic approach, it can provide more information about the imaged domain by transmitting/receiving signals into/from all parts of the imaged domain.

The imaging algorithm can be categorised based on the utilised frequency bandwidth e.g., single frequency, narrow-band multi-frequency, or ultra-wideband (UWB). In this case, the microwave-based imaging techniques can be divided into two main types of tomography [6]-[33] and beamforming [34]-[48]. Due to time-consuming nature of tomography-based techniques, they are mostly applicable to single frequency or narrow-band multi-frequency signals, while beamforming methods require wideband signals to create accurate images.

2.1.1 Microwave Tomography Technique

In microwave tomography technique, which is also known as quantitative technique, the dielectric permittivity map of the imaged domain is estimated by solving an inverse scattering problem. In this method, the measured electric fields are used as input to an electromagnetic inverse problem derived from Maxwell's equations. The inverse problem is nonlinear in terms of unknown parameters and hence, it is ill-posed i.e. more than one solution satisfies the equations. Therefore, additional information and/or estimations are required to mitigate the intrinsic ill-posed nature of the inverse problem. In most cases, iterative Newton-based methods [19] such as Gauss-Newton [20]-[21], inexact Newton [22], and conjugate-gradient [23], are used to solve the nonlinear inverse problem. Optimisation-based methods [24]-[14], Born/distorted Born iterative methods [27]-[28] and compressive sensing [28]-[29] are other solutions that can solve the ill-posed inverse problem in a more efficient way with minimal number of antennas. In those algorithms, the forward and inverse problems are iteratively solved to reach a threshold level in parameter estimation error. In each iteration, the calculated field from the current permittivity distribution is compared with the measured field. The success of these techniques is highly dependent on the quality of the used model for forward problem solving. Therefore, an alternative class of methods based on the contrast source inversion method [30] with capability of solving the ill-posed inverse problem without a forward solver are proposed [31]-[33]. In these techniques, two sets of linear equations are solved in each iteration instead of solving the forward problem.

The abovementioned techniques are mostly applied to single- or multi-frequency measurement setups, which usually use matching medium to reduce skin reflections. In [6]-[8], different authors used single-frequency tomography at 2.45 GHz for head and heart imaging, respectively. The results were promising for a homogeneous head model, especially in the area of differential imaging. However, there were some limitations in the detection of large dielectric contrasts, which is the main purpose of microwave medical imaging. Authors in [9] proposed a microwave tomographic breast scanner operating in multiple frequencies over the band of 300-1000 MHz. Frequency-hopping approach [13] is another kind of multi-frequency technique, in which low

frequencies are used to image high-contrast tissues with large structures. The calculated values from lower frequencies are then used as priori information for the proceeding iterations at higher frequencies to improve the resolution and detect smaller objects. A time-domain inversion algorithm was also proposed in [14], where a narrowband pulse with centre frequency of 6 GHz and bandwidth of 300 MHz was synthesised from frequency domain data to detect breast cancer.

As described earlier in this section, tomography-based techniques involve solving ill-posed equations of the inverse electromagnetic problem, which are computationally complex and time-consuming. Therefore, they are not used for medical emergency applications like brain injury detection, where fast diagnosis is required.

2.1.2 Microwave Beamforming Technique

Microwave beamforming is a radar-based technique in which significant scatterers profile of the imaging domain is mapped on a two- or three-dimensional image by processing the scattered signals across a wide microwave frequency band. This method is more applicable when using ultra-wide bands for fine resolution due to its relatively simpler and faster processing than tomography. However, the variation of dielectric properties of human tissues with frequency, known as frequency dispersion, should be considered to enable the detection of abnormalities in realistic scenarios by utilising this method. The obtained image from this method can shows the location of significant scatterers, which are the imaged domain pixels with high contrasts in the dielectric properties with respect to other tissues; such high contrast areas represent the abnormalities. The created images in addition to physical, cognitive, and behavioural symptoms can help paramedics to confirm the existence of an injury and give proper medical intervention.

This method was firstly utilised in microwave medical imaging by using delay-and-sum (DAS) algorithm [35]-[39]. In this method, a UWB signal is transmitted to the imaging object and the received signals in time-domain are used to create the map of scattered fields in the imaged domain. Assuming the focal points inside the imaging domain as point scatterers, the received signals $x[n]$ are delayed by a time delay $n(\mathbf{r}_0)$, which is calculated based on the wave traveling distance from transmitter to the individual point scatterers and to the receiver, $\mathbf{r}_0$. The sum of the delayed signals $z[n]$ at all the focal points are then used to calculate the scattered energy $p(\mathbf{r}_0)$ and obtain the resultant image. Fig. 2.1 shows the flowchart of this method.

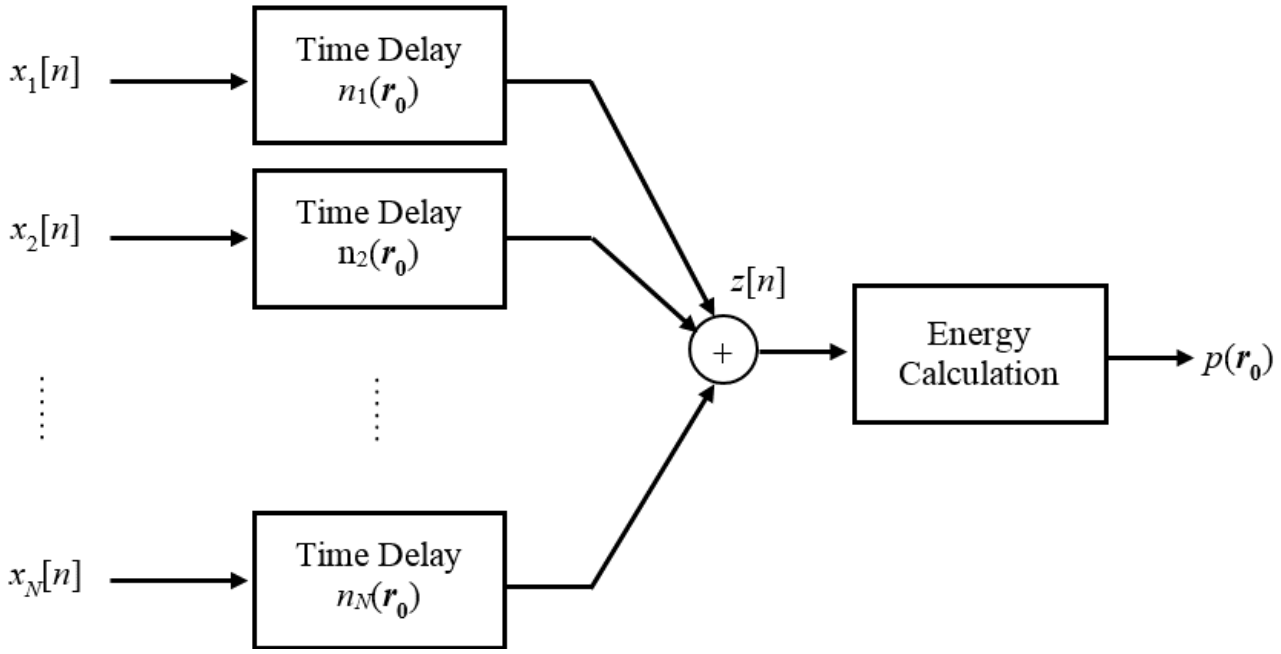

Fig. 2.1. Block diagram of delay-and-sum (DAS) algorithm

The DAS method does not consider the interaction between scatterers and hence is highly susceptible to outer layer reflections and internal layer refractions that consequently result in false detection in heterogeneous environments such as human body. To that end, microwave imaging via space-time (MIST) beamforming technique [40]-[41], which uses time windowing and finite-impulse response filters to discriminate between target and clutter/noise signals, was developed (Fig. 2.2). In this method, the delayed signals are firstly windowed to remove interference and clutter using the window function $g[n]$. Then, the signals are filtered by a finite-impulse response filter, FIR $\mathbf{w}(\mathbf{r}_0)$, to equalise path length and compensate for the dispersion and attenuation inside the imaged object. The output signal $z[n]$ is windowed with $h[\mathbf{r}_0, n]$ to ensure that the output energy is calculated by only samples of the sum of aligned signals $z[n]$ and eliminate additional clutter. This method was designed for monostatic modalities. The quasi-multistatic MIST beamforming is also developed to enhance the performance of the MIST method for the early stage detection of breast cancer [42]. Those methods are tested on numerical breast models that show promising results in both cases. However, the applicability of those methods in realistic heterogeneous environments and multistatic approaches is questionable [43].

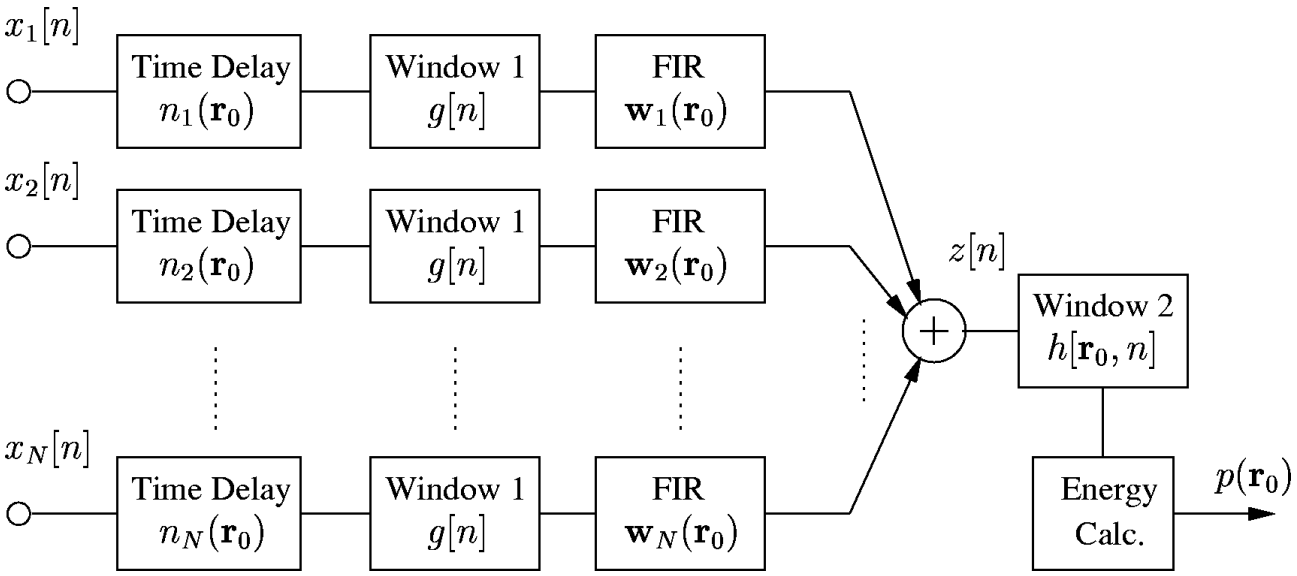

Fig. 2.2. Block diagram of microwave imaging via space-time (MIST) beamforming algorithm [40]

Multistatic adaptive microwave imaging (MAMI) [43] is another beamforming technique to address the shortcomings of aforementioned techniques. This technique utilizes data-adaptive Capon beamformer to mitigate the skin interferences and to achieve high resolution images. The obtained results from using this method for breast cancer detection via numerical models and subsequently, through measurements on homogenous breast phantoms [44] show successful detection of tumours in three-dimensional homogeneous breast models and phantoms.

In order to improve the imaging capability of MAMI technique in heterogeneous environments, a time-domain wideband adaptive beamforming technique [46] is proposed that use multiple filter banks and data adaptive processing (Fig. 2.3). This technique utilises multi-stage time-domain data-adaptive beamformer based on minimum variance distortion-less response (MVDR) method. In the first stage of this technique, the influence of skin on the obtained signals are mitigated by using a mechanical differential scanning calibration technique. The pre-processed signals are then equalised to compensate for attenuation and phase errors by using an *L*-tap finite impulse response (FIR) filter, which is adapted from the MIST beamforming technique. Finally, the filtered signals are processed using the MVDR method.

Promising results have been reported for experimental and clinical measurements in [46] using the wideband adaptive beamforming technique. However, the multi-stage calibration and filtering techniques are complex and time consuming.

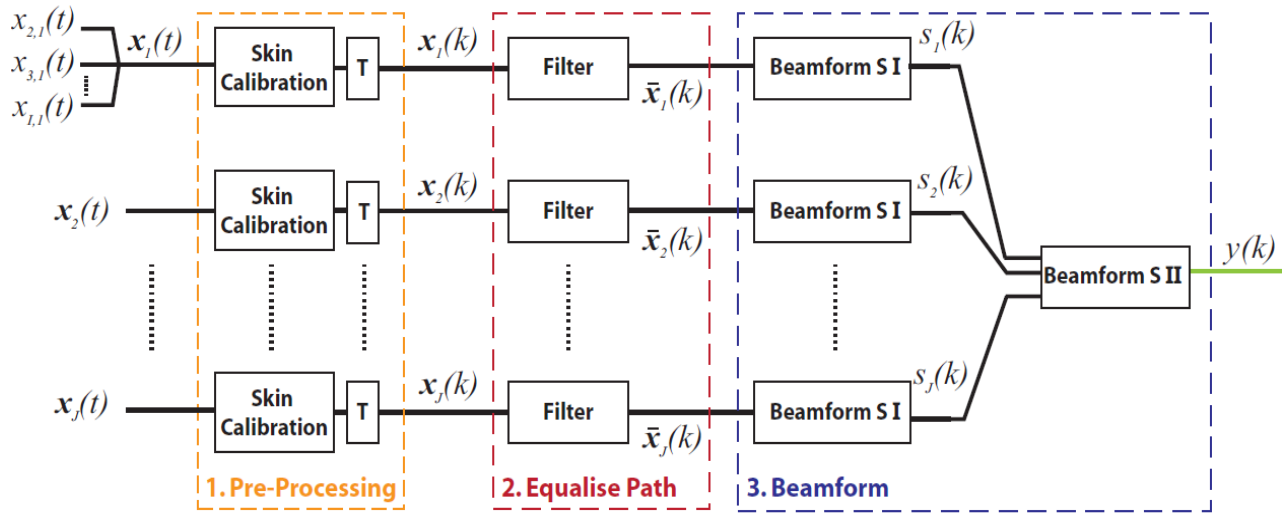

Fig. 2.3. Block diagram of wideband adaptive beamforming algorithm [46]

In another approach, an algorithm based on machine learning and statistical classification was adopted [47]. However, that detection method requires significant computational power and time and is still a work in progress to improve accurate localisation of target.

2.2 Challenges in the Development of a Microwave Medical Imaging Algorithm

As mentioned in the previous section, the current time-domain methods were tested mostly in breast imaging, which has a simpler imaging domain compared with other human body parts, such as head imaging domain that contains skin, skull, fat, and muscle tissues around a complex distribution of different brain tissues. Applying time windowing and spatial filtering on multilayer domains like head imaging domain cannot properly reject clutter from backscattered signals because of the time-domain overlap of received signals. In addition, variation of penetration ability of signals at different frequencies through the human body affects the effectiveness of those filters and consequently, accuracy of the imaging procedure. Therefore, a sophisticated clutter removal technique that mitigates the signal clutter from multilayer imaging domains is required.

To establish a fast diagnostic imaging system, a fast imaging algorithm is required. The presented time-domain algorithms are usually time-consuming due to the use of multi-stage calibration and filtering techniques. Therefore, a new imaging algorithm that detects the location of injuries and abnormalities inside the imaging domain in a fast and consistent way is essential. In the development of such an imaging algorithm, the frequency dispersion of dielectric properties of human tissues should also be considered. The frequency dispersion results in the distortion of the wideband pulses used in the time-domain radar-based imaging methods.

The required number of antennas is another challenge that needs to be carefully addressed in microwave medical imaging area. The accuracy of microwave imaging is highly dependent on the number of antennas used for data acquisition. The number of antennas is usually determined based on the antenna size, available space for antennas, and acceptable hardware complexity to use as many antennas as practically possible. However, using a large number of antennas can complicate the process and hence make the data acquisition and processing greatly time-consuming. Therefore, it is crucial to specify the minimum and maximum number of antennas required for the imaging algorithms to detect targets and satisfy high quality image requirements.

Another challenge in the development of a microwave medical imaging technique is to find the effective dielectric properties of the imaged domain as a priori information. All of the presented microwave imaging algorithms need a priori information on the wave's propagation speed in the imaging domain. Thus, the average dielectric constant of the domain is typically assumed in the homogeneous propagation models employed by those algorithms. Those methods estimate the average permittivity of the imaging domain by averaging the dielectric properties of the constitutive tissues of the imaged model. However, this method is not practical in realistic scenarios where the size and hence dielectric properties of tissues differs from patient to patient. Therefore, a method to accurately predict the dielectric properties of the imaged domain is required for successful imaging algorithms.

Furthermore, a microwave imaging algorithm requires boundaries of the imaged object as a priori information. While it might be possible to manually measure that boundary in a controlled lab environment, this cannot be achieved in the clinical environment due to the impracticality of such a measurement in addition to the effect of the natural subject's movement. Therefore, a method for boundary identification of the imaged object at the same time of imaging is needed.

2.3 Summary

This chapter discussed different microwave imaging techniques for medical diagnosis. The existing state-of-the-art imaging technologies are categorized into two different types of tomography and beamforming techniques. Advantages and limitations of the two types of methods are described and it is noted that beamforming microwave imaging have the potential of overcoming those limitations. It is noted that in the literature the current beamforming techniques are usually complex and time consuming. In addition, those methods are tested with simplified models or phantoms. Challenges in the development of a microwave medical imaging algorithm are described in the last section of this chapter.

3 FAST FREQUENCY-BASED MICROWAVE IMAGING TECHNIQUE

As mentioned in the previous chapter, current radar imaging methods utilize processing techniques based on delay-and-sum (DAS), which might be susceptible to outer layer reflections and internal layer refractions that consequently result in false detection. In addition, the applicability of those methods in realistic heterogeneous environments and multistatic approaches is questionable.

In order to address the aforementioned issues, a frequency domain algorithm is proposed in this work. It is demonstrated that the frequency-based calculations can properly mitigate multiple reflections by considering the frequency-dependent propagation effects without the need to rely on wave path estimations. This method applies Bessel functions [48]-[49] in frequency domain for fast image processing that maps regions of high dielectric contrasts of the imaged domain in a two dimensional plane. In this algorithm, the Nyquist concept is adopted to reduce the number of sampling frequency utilising minimal number of antennas to lower the computational complexity effectively whilst attaining correct detections.

This chapter is organised into six sections. Section 3.1 contains the explanation of the proposed algorithm. In Section 3.2, the proposed method is tested through realistic simulations and experiments to verify its efficacy in locating targets in different scenarios. The procedure to accelerate the algorithm is outlined in Section 3.3. In Section 3.4, the proposed method is compared favourably with two important multistatic time-domain imaging methods (multistatic delay-and-

summation multi-DAS [39] and multistatic adaptive microwave imaging MAMI [43]). Finally, a summary is presented in Section 3.5.

3.1 Proposed Imaging Algorithm

Low frequency microwave signals (around 1-2 GHz) have higher penetration depths inside lossy head tissues. Nevertheless, the difference between the dielectric properties of skin tissue layer and air interface causes strong reflections in the received signals. Furthermore, the signals are deteriorated by the multiple reflections from different outer layers (skin, skull, fat, and muscle) caused by the dielectric contrast between different tissues. One solution to the strong interface reflections is to use a suitable matching medium to fill the air gap between the antennas and the imaged object to improve signal penetration through that object. However, this solution is not preferable due to added practical complications and an added interface that may contribute to reflections and losses especially in patients with dense hair.

There are different methods to remove the reflections in radar imaging approaches, like Average Trace Subtraction [50], Spatial Filtering [51], Subspace Projection [52] and Differential Approach [53]. Considering a constant distance between the position of the antennas and the skin layer and uniform thicknesses for the outer layers of the head (skin, skull, fat, and muscle), the contributions of clutter and reflections to all of the antennas are similar. To that end, the reflections can be separated by removing a constant value from the received signals. The average-trace subtraction technique, which subtracts the calculated average value from the received signals, is a simple method that can effectively mitigate this type of reflections. The technique is applied on the reflected (S_{ii}) and transmitted signal (S_{ij}) separately. The average of all the received signals in each type is deducted from corresponding signal of the antenna at each frequency step (f_k):

$$S\left(rx_i, tx_j; f_k\right) = \begin{cases} S_{meas}(rx_i, tx_i; f_k) - \frac{1}{N_a}\sum_{i=1}^{N_a} S_{meas}(rx_i, tx_i; f_k) \\ S_{meas}\left(rx_i, tx_j; f_k\right) - \frac{1}{N_a(N_a-1)}\sum_{\substack{i,j=1 \\ i\neq j}}^{N_a} S_{meas}\left(rx_i, tx_j; f_k\right) \end{cases} \tag{3.1}$$

rx and *tx* in (3.1) represent the receiver and transmitter indexes, respectively. This method estimates the reflection by averaging the signal along antenna locations instead of through inverse scattering. In addition, applying trace subtraction in every frequency step enables this method to consider the variation of penetration capability of microwave waves at different frequencies.

By eliminating the boundary reflections, the imaged domain can be considered as a homogeneous medium. Thus, the scattered power intensity in the imaged region is calculated by solving time-

dependent Maxwell's equations. Lastly, the final image is produced by stacking of the estimated power intensities over all frequency samples and antenna positions.

The aim of the presented system is to image a cross section of the 3D head, located at the phase centre of the antenna. Due to the unidirectivity of the utilised antennas, the majority of the radiated power propagates through that cross section in front of the antenna. Thus, the scattering profile of that cross section can be estimated by considering 2D electromagnetic approaches. The considered imaging domain is shown in Fig. 3.1 where an incident electromagnetic wave E_{inc}, propagates from the transmitter to the head cross section that has an effective dielectric constant ε. The scattered field from different point scatterers inside the imaged domain is then measured by an observer, E_{meas}, outside the boundary.

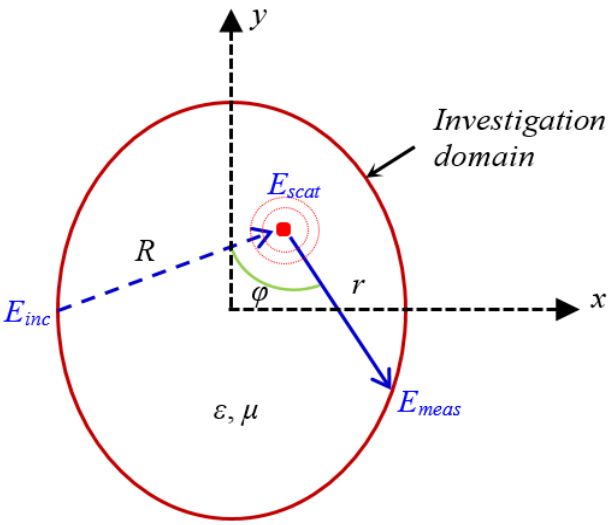

Fig. 3.1. Incident and scattered electric fields in the imaged domain.

The scattered electric field E_{scat} is calculated by estimating the back-propagated signal from the measured field at distance r from the observer [54]. To that end, the target response at each receiving antenna is correlated with the incident field and synthetically propagated to the imaged domain. The scattered field is calculated by

$$E_{scat}(r, \varphi; f_k) = E_{meas}(rx_i, tx_j; f_k) G^*(r, \varphi; f_k) \tag{3.2}$$

where, G is the two-dimensional Green's function of the point scatterer and $G^*(r, \varphi; f_k)$ is the conjugated received fields at the rx_i-th receiver due to an excitation at tx_j-th transmitter and propagation via the point scatterer (r, φ) at f_k-th frequency location of the tx_j-th transmitter and rx_i-th receiver defines the parameters r and φ (see Fig. 3).

The scattered field at a far-field distance r ($r>2D^2/\lambda$, where D is diameter of the point scatterer and λ is the effective wavelength inside the imaged domain [55]) behaves as a spherical wave.

Considering a cross section of the wave in the *x*-*y* plane, the conjugated field at one frequency sample can be specified by

$$G(r,\varphi) = f(r,\varphi)e^{ikr} \tag{3.3}$$

$f(r, \varphi)$ represents the complex scattering parameter which contains the wave properties at the location of scatterer. The Maxwell's equation corresponding to the scattering parameter is

$$\frac{d^2 f(r,\varphi)}{dr^2} + k^2 f(r,\varphi) = 0 \tag{3.4}$$

where k is the wavenumber.

Using variables separation technique, the scattering parameter can be separated as $f(r, \varphi) = U(r)V(\varphi)$ where two single variables of U and V can be solved using:

$$V"(\varphi) + n^2 V(\varphi) = 0 \tag{3.5}$$

$$r^2 U"(r) + rU'(r) + (k^2 r^2 - n^2)U(r) = 0 \tag{3.6}$$

where n is a constant value. The solution for (3.3) is

$$V(\varphi) = a_n \cos n\varphi + i\, b_n \sin n\varphi \tag{3.7}$$

Since there should be only one value for the scattered field in one point and according to the shape of the cylindrical wave, $V(\varphi)$ is single-valued for φ and periodic with 2π; hence, n=1 is the only value that satisfies the boundary condition, which makes (3.5) an equation of ellipse:

$$V(\varphi) = a \cos \varphi + i\, b \sin \varphi \tag{3.8}$$

From the physical point of view, $V(\varphi)$ demonstrates how the scattered wave varies with φ, while the constants a and b represent the observed electromagnetic fields over φ. Assuming the imaged region to be homogeneous and the back-propagated field as a cylindrical wave, a and b are identical. This can be explained by the fact that a point scatterer scatters the wave uniformly to all directions [56]. In other words, the magnitudes of the fields from different point scatterers at the same observer's distance are equal, but their phases change with the observation angle φ; thus, the solution for V can be calculated by assuming $a = b = 1$:

$$V(\varphi) = cos\,\varphi + i\ sin\,\varphi = e^{i\varphi} \tag{3.9}$$

On the other hand, by assigning the produced value for *n* from in (3.4), it can be written as:

$$r^2\frac{d^2U}{dr^2} + r\frac{dU}{dr} + (k^2r^2 - 1)U = 0 \tag{3.10}$$

Following the approximation used in microwave medical imaging algorithms [34] in ignoring the effect of losses (imaginary part of *k*), (3.10) is the differential equation for 1st kind, 1st order Bessel function [$U(r) = J_1(kr)$]. Consequently, $f(r, \varphi)$ is:

$$f(r,\varphi) = U(r)V(\varphi) = J_1(kr)e^{i\varphi} \tag{3.11}$$

and the Green's function can be written as:

$$G(r,\varphi) = J_1(kr)e^{i(kr+\varphi)} \tag{3.12}$$

Then, the point-scatterer field can be calculated by assigning the conjugated field from (3.12) in (3.2):

$$E_{scat}(r,\varphi) = E_{meas}(rx_i, tx_j)\,J_1(kr)e^{-i(kr+\varphi)} \tag{3.13}$$

where the Bessel function [$J_1(kr)$] can be defined by its polynomial approximation [57]:

$$J_1(kr) = \sum_{i=1}^{n}\frac{(-1)^{i+1}(2n)^{1-2i}(i+n-1)!}{(i-1)!(n-i)!i!}(kr)^{2i-1} = \frac{1}{\pi}\sum_{i=0}^{n} cos\left[\frac{\pi}{n}i - kr\,sin\left(\frac{\pi}{n}i\right)\right],\ n \geq \frac{kr}{2} \tag{3.14}$$

Scattered power density inside the imaging domain can be calculated using measured S-parameters, $S(rx_i, tx_j)$:

$$S_{scat}(r,\varphi) = \frac{1}{2}[E_{scat}(r,\varphi) \times H^*_{scat}(r,\varphi)] = \frac{\varepsilon v}{2}E^2_{scat}(r,\varphi) = \frac{\varepsilon v}{2}E^2_{meas}(rx_i, tx_j)\,J_1^2(kr)e^{-i2(kr+\varphi)} = S(rx_i, tx_j)\,J_1^2(kr)e^{-i2(kr+\varphi)} \tag{3.15}$$

and

$$S(rx_i, tx_j) = \frac{\varepsilon v}{2}E^2_{meas}(rx_i, tx_j) \tag{3.16}$$

where $v = 1/\sqrt{\varepsilon\mu}$ is the average wave speed in the medium.

It worth noting that based on the working frequency and imaging domain dimensions, the imaging process is in both near and far field regions. Therefore, the scattered power can be estimated for both regions by using the calculations in one of them. Since the purpose of the technique is to detect the targets inside the human body, far-field calculations are performed in (3.15) and (3.16).

The total power density at an arbitrary location (x, y) inside the cross section is estimated by the summation of the calculated powers from different angles, φ, and corresponding receiver positions, rx_i (i=1 to N_a) around the head [55]:

$$S_{total}(x,y) = \int_{2\pi} S_{scat}(r,\varphi)d\varphi \approx \sum_{i=1}^{N_a} S_{scat}(r,\varphi,rx_i) = \sum_{i=1}^{N_a} S(rx_i,tx_j)\, J_1^2(kr)e^{-i2(kr+\varphi)} \quad (3.17)$$

To compensate for the lack of discrete observation points, different scattered profiles from different transmitters and frequencies are superposed and presented as the final image:

$$I(x,y) = \frac{1}{{N_a}^2}\left\|\sum_{k=1}^{Nf}\sum_{j=1}^{Na}\sum_{i=1}^{Na} S\left(rx_i,tx_j,f_k\right) J_1^2(kr)e^{-i2(kr+\varphi)}\right\| \quad (3.18)$$

where N_a and N_f are respectively number of antennas and frequency samples.

Fig. 3.2 shows the block diagram of the proposed microwave imaging algorithm for multistatic approach.

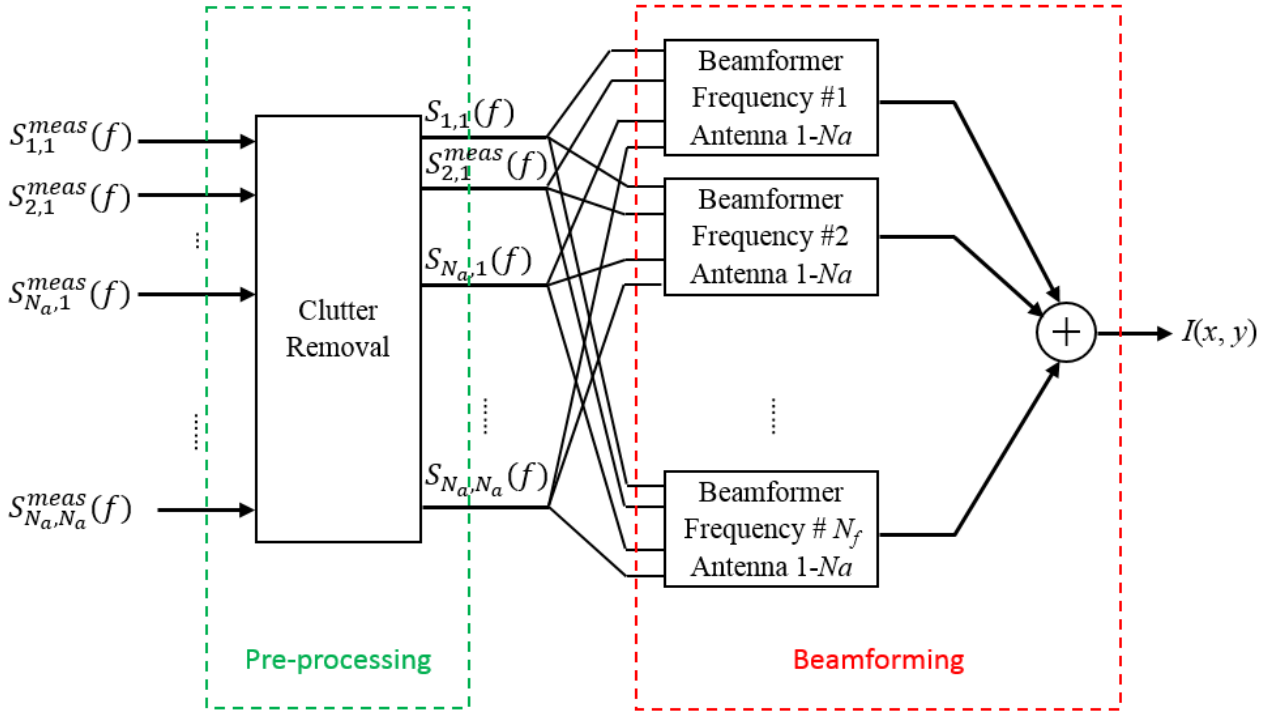

Fig. 3.2. Block diagram of fast frequency-based microwave imaging algorithm

The proposed algorithm can be used in monostatic measurement setups by inserting $\varphi = 0$ and changing the triple summation operator to double one in (3.18):

$$I_{mono}(x,y) = \frac{1}{N_a}\left\|\sum_{k=1}^{Nf}\sum_{j=1}^{Na} S(tx_j, f_k)\, J_1^2(kr) e^{-i2(kr)}\right\| \quad (3.19)$$

The reconstructed image illustrates the intensity of significant scatterers by the summation of all discrete powers that emphasises substantial powers and diminishes negligible powers. It should be mentioned that this procedure does not provide the detailed image of the internal powers and shows only regions of contrasts in the dielectric properties, which is enough for detection purposes. Obviously, the proposed procedure differs considerably from microwave tomography, which usually struggles to find the electrical properties of the tissues due to the need to solve ill-posed inverse problems. In comparison to the time-domain methods (confocal, space-time beamforming MIST, and adaptive beamforming imaging algorithms), the proposed method performs all the calculations in the frequency domain, and thus it is more immune against multiple reflections produced by multilayer structures and faster to process.

3.2 Algorithm Validation

In order to verify the imaging algorithm, an integrated imaging system is needed. Therefore, a multistatic antenna array and a 3D human head phantom are used in full-wave electromagnetic simulations. Moreover, an experimental setup is built and used to verify the method. The monostatic form of the developed method is also used for the feasibility study of lung cancer detection using a monostatic microwave-based torso imaging system.

3.2.1 Simulation Results

In multistatic imaging, the realisable angular space between antennas, final image resolution, mutual coupling limitations, hardware complexity, and image acquisition time are important factors that determine the number of antennas and frequency samples. Synthesising a multistatic array with all the aforementioned requirements is challenging. However, according to the size and coupling limitations of the utilised antenna, which is a modified version of the antenna presented in [58], two elliptical shape arrays consisting of twelve and eight compact ultra-wideband antennas are investigated.

The used antenna is depicted in Fig. 3.3. It has the dimensions of 7 × 3 × 1.5 cm^3 which is equivalent to 0.24 × 0.1 × 0.05 λ_0^3, where λ_0 is is the wavelength of lowest operating frequency. From the mechanism perspective, the antenna's structure includes a dipole and folded parasitic

structure. The dipole is responsible for the upper band of operation. The folded parasitic structure along with the dipole forms a loop-like geometric structure, which assists the antenna to attain the lower operating frequencies. The top printed layer of the antenna contains two T-shaped slots along X-axis. These slots increase the effective current paths and serve in achieving relatively lower frequencies of operation with the same space.

This antenna is revised to operate in an elliptical shape array surrounding the head with improved performance in terms of bandwidth and directionality compared to the previously reported antenna [58]. The performance of the antenna is simulated and measured. As illustrated in Fig. 3.4, the modified antenna operates from 1 to 3.2 GHz with the return loss of more than 10 dB in free space. An extended measurement of the radiation patterns shows that over the whole operating band, the antenna is unidirectional and steadily radiates along Z-axis (θ = 0°, φ = 0°) with an average gain of 3.5 dBi. The mutual coupling between any two neighbouring array antennas is less than -20 dB, which shows the limited impact of array elements on each other.

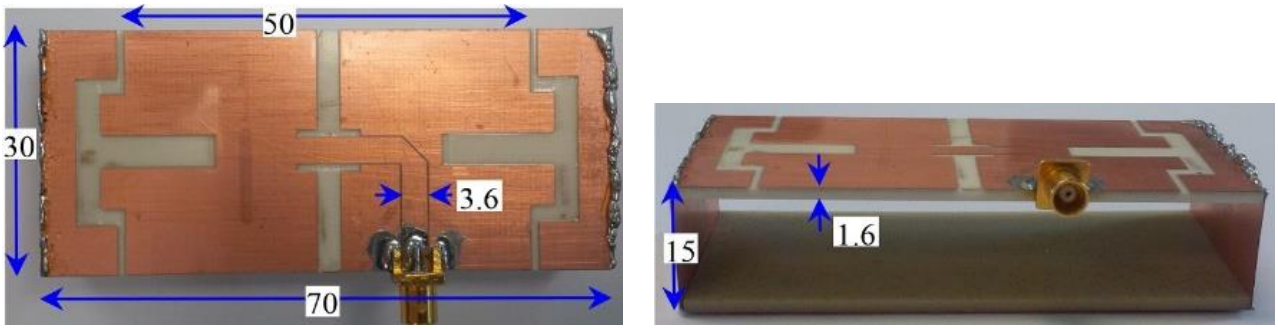

(a) (b)

Fig. 3.3. The designed antenna (a) top and (b) side views. Dimensions in (mm).

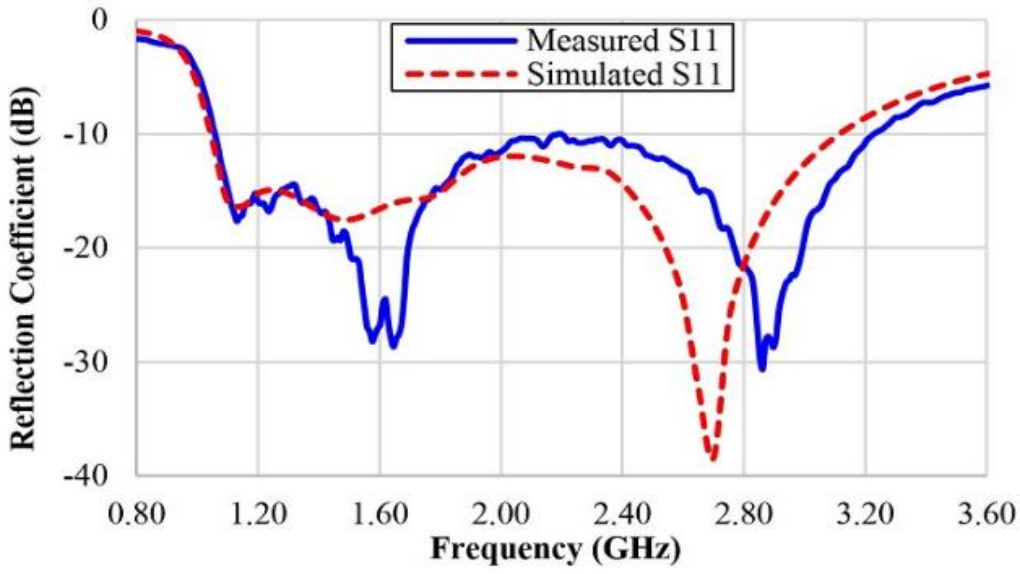

Fig. 3.4. Reflection coefficient of the antenna.

To build a realistic simulation environment, a 3D numerical human head phantom containing realistic tissue distributions based on MRI scans with frequency dispersive dielectric properties [59] is used. The ranges of permittivity values for various head tissues over the operating frequency range are illustrated in Fig. 3.5. The brain injury (bleeding) is emulated by inserting a block ($2 \times 2 \times 2$ cm^3) of blood inside the head phantom. To verify the possibility of using small number of antenna elements in the proposed method, two configurations are used in the simulations as depicted in Fig. 3.5. The first one uses twelve antenna elements to surround the head, whereas the other uses eight antenna elements. In both cases, a signal covering the frequency band 1.1-3.2 GHz is transmitted by one antenna, while the backscattered signal is received by all the antennas. This process is repeated for all of the antennas and the received signals from 365 frequency samples are recorded and processed using the proposed algorithm. The total image reconstruction time of the proposed algorithm using general-purpose PC having 3.4 GHz CPU and 16 GB RAM is about 13 and 25 seconds for eight- and twelve-element antenna arrays, respectively. Fig. 3.6 shows the imaging results from the two configurations before and after clutter removal. It is to be noted that the reconstructed images are normalised to the maximum intensity within the imaged area.

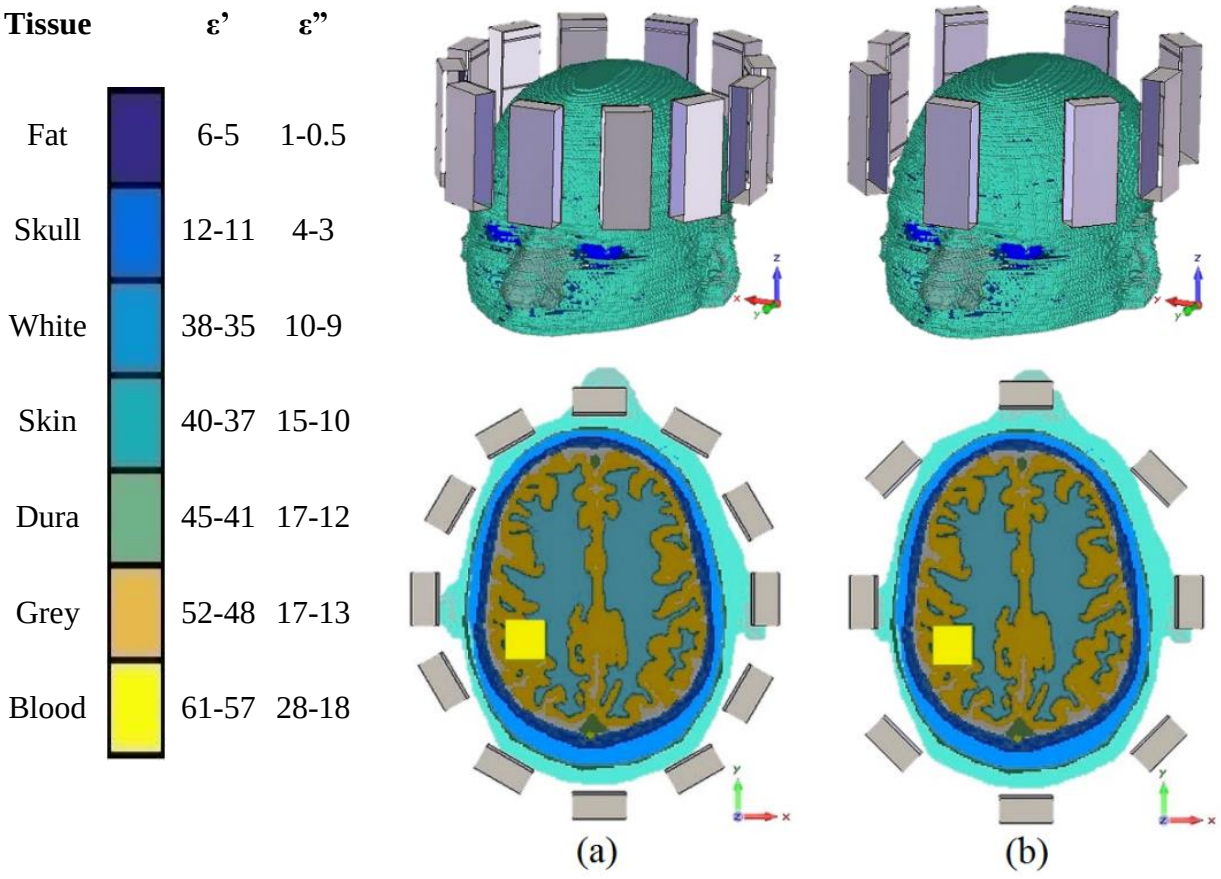

Fig. 3.5. Simulation setup using (a) 12-antenna and (b) 8-antenna arrays.

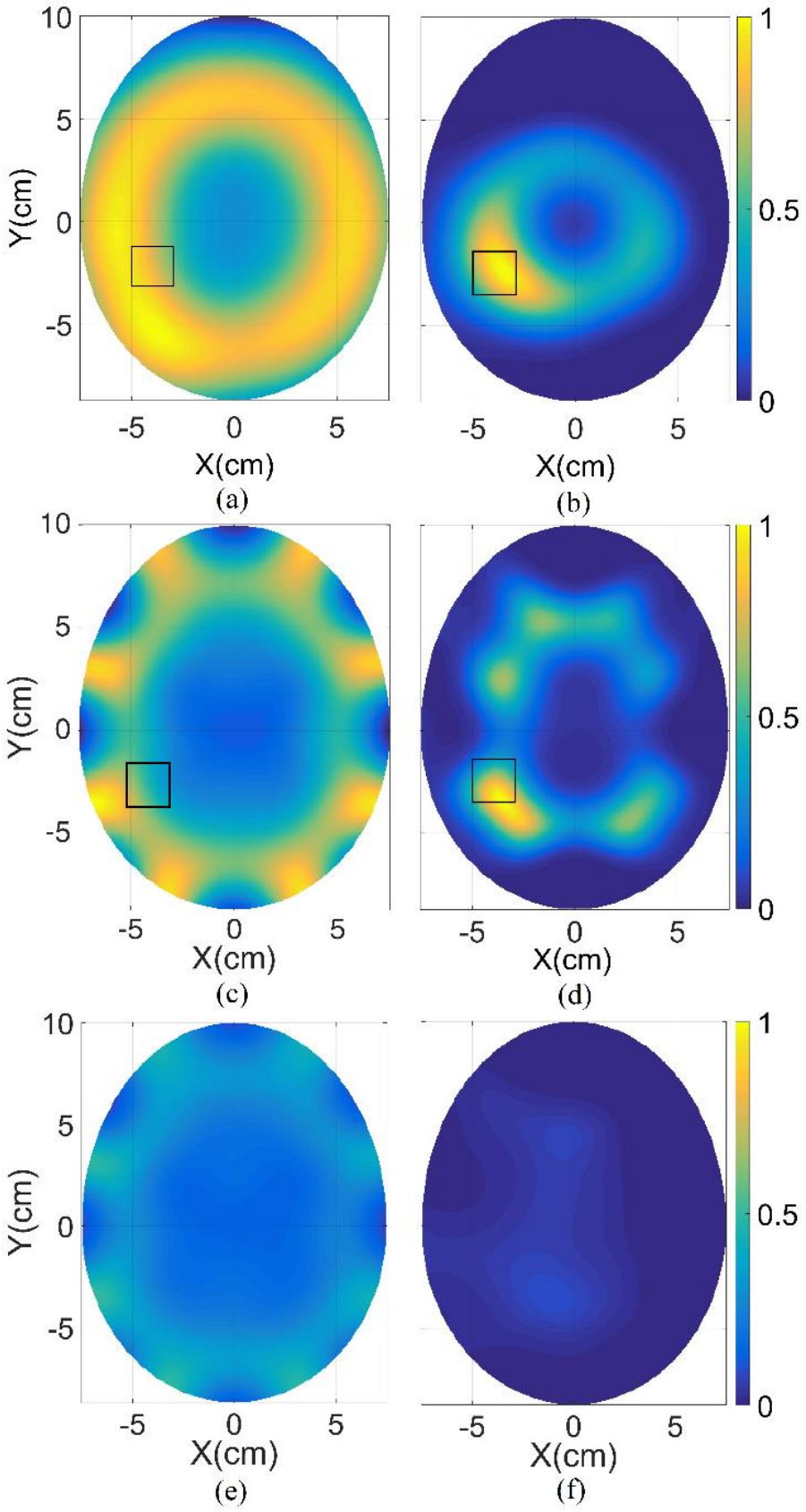

Fig. 3.6. Reconstructed images from the simulation environment for unhealthy scenario with 12-antenna array, (a) before and (b) after clutter removal; 8-antenna array, (c) before and (d) after clutter removal; healthy scenario with 8-antenna array, (e) before and (f) after clutter removal. Squares in (a) to (d) show the exact location of the brain injury.

Fig. 3.6 (a) and (c) demonstrate that the target can be masked by strong background reflections. From Fig. 3.6 (b) and (d), it can be seen that the average subtraction method can properly mitigate the effect of the strong clutter. In these figures, the exact location of bleeding is indicated by a square. The effectiveness of the proposed method in detection and localisation of the injury can be realised from these reconstructed images, though with a slight shift in position, the target in the two configurations. However, some insignificant ghost targets appear in the reconstructed image (Fig. 3.6 (d)), which are attributed to the residual skin reflections due to the assumption of uniform thicknesses of the outer head layer.

To demonstrate the capability of the method in distinguishing between healthy and unhealthy cases, images of a healthy scenario before and after the clutter removal using the eight-antenna array are depicted in Fig. 3.6 (e) and (f). It is clear that the image before a clutter removal includes suspected false targets, whereas the image after the clutter removal indicates a healthy case with very low intensity areas.

In order to investigate the quality and accuracy of the reconstructed images, three quantitative functions which are presented in [58] are computed. The first parameter is the average target to clutter ratio:

$$Q = \frac{\overline{I(p)}}{\overline{I(q)}} \qquad \begin{matrix} \forall p \in S \\ \forall q \in H \,\&\, q \notin S \end{matrix} \,, \tag{3.20}$$

which calculates the contrast of the target with respect to the whole imaging domain by dividing the average intensity of the target region, *S*, over the average intensity of the rest of the head. $Q>1$ is an acceptance value for a high contrast detection. The second parameter is the maximum target to clutter ratio:

$$\gamma = \frac{\max[I(p)]}{\max[I(q)]} \qquad \begin{matrix} \forall p \in S \\ \forall q \in H \,\&\, q \notin S \end{matrix} \,, \tag{3.21}$$

which compares the maximum intensity of the known target region, *S*, with the maximum intensity at any other place within the whole imaging region, *H*. $\gamma > 1$ means that the target is accurately detected, $\gamma < 1$ means a wrong detection and $\gamma = 1$ means there is a clutter as strong as the target.

The last parameter, Δ is the difference between the actual center of the target, α, and the calculated one p^*:

$$\Delta = \|p^* - \alpha\|. \tag{3.22}$$

Low values of Δ represent better-reconstructed images and Δ=0 means an ideal case.

Knowing the assumed bleeding size and location, the aforementioned metrics are analysed for the reconstructed images in Fig. 3.6, and listed in Table 3.1. Since $\gamma > 1$, the resultant images for both of the two configurations enable the correct detection. The γ, Q and Δ values in this table show that the 12-antenna configuration has obviously higher contrast and is more accurate than the eight-antenna structure. However, the eight-antenna configuration has acceptable metrics values and even Q = 4.8 presents a higher contrast than the reported values in [58], which uses the same simulation environment with even larger number of antennas (72 monostatic antennas) and confocal imaging method. Based on the resultant values and due to the simplicity and fast data acquisition and image reconstruction processes, the challenging eight-antenna array is selected for the experiments.

Table 3.1. Image quality in the two simulated configurations.

Number of Antennas	Q	γ	Δ (mm)	Figure
12	6.3	1.60	5.7	Fig. 3.6 (b)
8	4.8	1.13	9.8	Fig. 3.6 (d)

3.2.2 Experimental Results

In this section, the measurement setup and experimental results of brain injury detection using eight-antenna array and the proposed imaging method is described. To collect multistatic data, the antenna array is integrated with an imaging system including Agilent N7081A microwave transceiver, which has a maximum dynamic range of 80 dB, a USB-8SPDT-A18 Mini-Circuits microwave switch matrix and an adjustable measuring platform. Fig. 3.7 shows the construction of the system hardware.

A realistic human head phantom (Fig. 3.8) is utilised in the experimental system in order to emulate the actual scenario of a patient with bleeding. The head phantom is anatomically realistic along with the realistic electrical properties of the actual human head. The realistic anatomical structure of the phantom is confirmed as the exterior and the internal casts of the phantom is based on MRI-scanned data of a real human head. The details of the composition of the fabricated tissues are described in [59]. The dielectric properties of the developed tissue-mimicking materials along with the actual ones are provided in Fig. 3.9. The exterior part of the phantom represents the combined effect of fat, skin, muscular parts and skull. The eye cavity is filled with the eye representing materials. The interior portion has tissue-imitating properties of the main brain tissues. Blood emulating materials are placed inside the head as brain injury target.

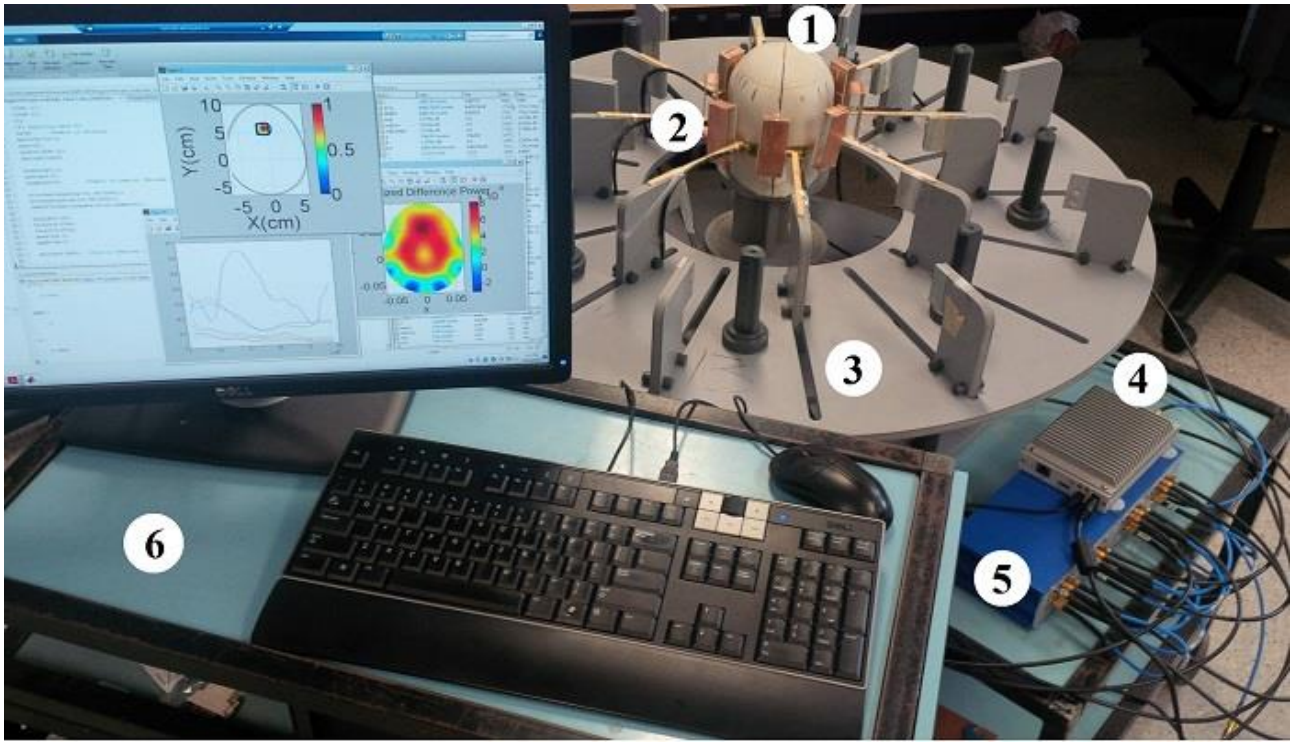

Fig. 3.7. Measurement platform indicating 1) realistic head phantom, 2) antenna array 3) measuring platform, 4) microwave transceiver, 5) switch matrix, 6) PC.

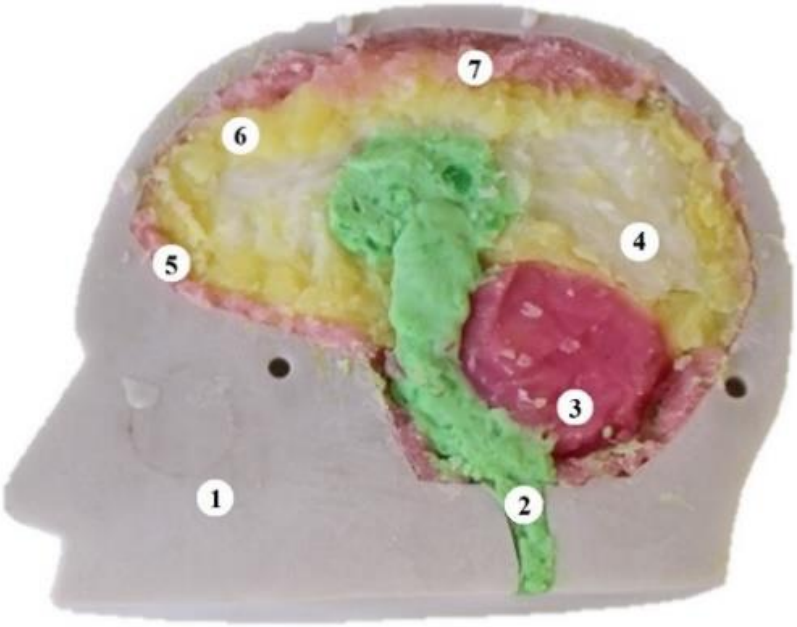

Fig. 3.8. Photograph of the internal structure of the fabricated 3D realistic human head [60]. 1) Exterior section, 2) spinal cord 3) cerebellum, 4) white matter, 5) Dura, 6) grey matter, 7) CSF.

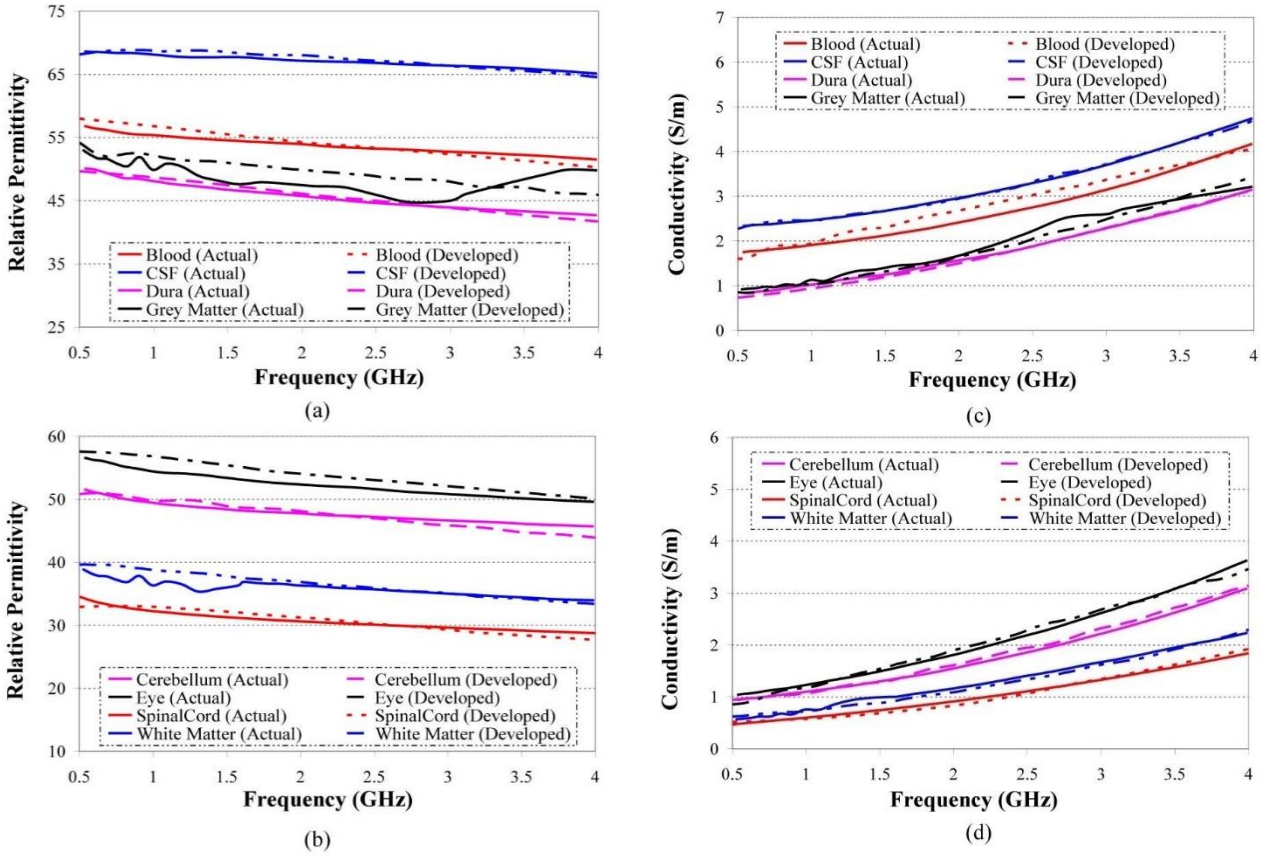

Fig. 3.9. (a, b) Relative permittivity and (c, d) conductivity comparisons of actual and developed head tissues [59].

To investigate the performance of the imaging algorithm, two different sizes of bleeding are inserted in two different locations of the head phantom. In the first case, a $2 \times 2 \times 2$ cm^3 part of the grey matter in the frontal position of the head is replaced by a blood-emulating material. In the second scenario, the white matter is replaced with a smaller target ($2 \times 1 \times 1$ cm^3) i that is located at the backside of the phantom. After initial procedure of microwave sensor calibration using the standard open-short-matched load steps, the phantom is located in front of the array. All the antennas of the array are located 1 cm away from the head. In each step, a microwave signal across the band from 1.1 to 3.2 GHz is transmitted by each antenna, whereas the scattered signals are recorded in all the antennas including the transmitting antenna. The received signals are recorded in every 6 MHz step and thus 365 frequency samples are recorded. With eight antennas, 36 independent signals are captured in 2 seconds. These data sets are imported in the imaging program and the final images are generated for the two scenarios as illustrated in Fig. 3.10.

According to Fig. 3.10, the proposed technique can successfully detect the targets in both of the two scenarios. Fig. 3.10 (b) shows that the reduction in the size of the target has affected the accuracy of the image. Although there is a slight error in the localisation of the smaller target, the calculated accuracy metric $\gamma > 1$ keeps it in the acceptance range.

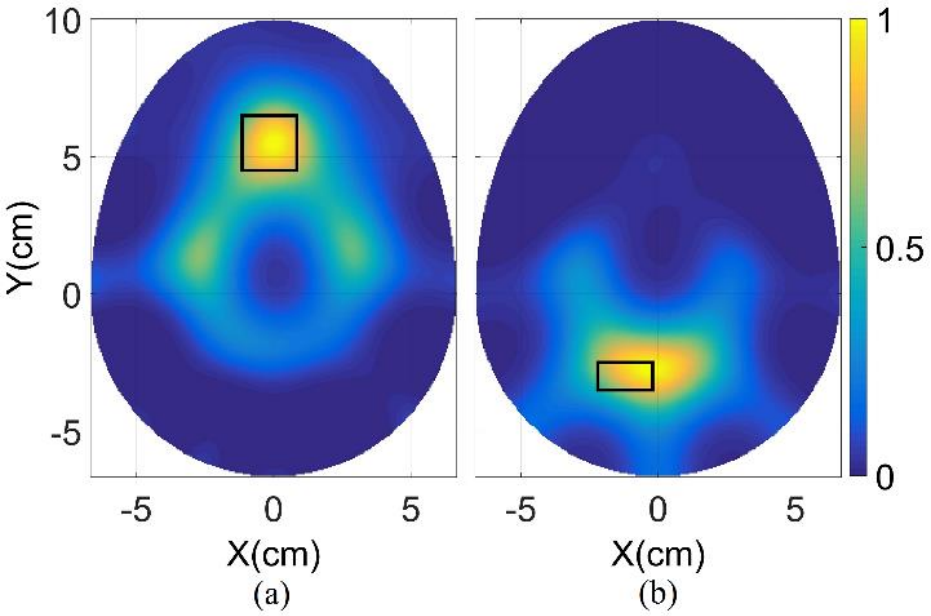

Fig. 3.10. Experimental results of (a) 2 × 2 × 2 cm3 and (b) 2 × 1 × 1 cm3 bleeding in the head phantom. Black rectangles show exact location of target.

The calculated quality metrics γ=1.3 and Q=6.5 for the experimental results with 365 samples show a better contrast than the simulation results (γ=1.13 and Q=4.8) using the same number of antennas, frequency samples and target size. It is also evident from the reconstructed images from simulations (Fig. 3.6 (d)) and measurements (Fig. 3.10) that less ghost targets appear in the experimental results than the simulations. The better performance of the algorithm in the measurements is due to the different residual reflections originated from different simulation and measurement environments. The head model in the simulations consists of all the individual realistic layers of skin, skull, fat and muscles, whilst due to the unavailability of equivalent 3D printing materials, these layers are modelled by one combined layer in the fabricated phantom [59]. However, the ghost targets do not significantly affect the image quality and the positions of brain injuries can be easily detected in both investigated scenarios.

3.3 Algorithm Acceleration

The total computational time for the general-purpose computer (3.4 GHz CPU, 16 GB RAM) to generate the image with 365 samples is 13 seconds for both of the simulations and experiments, which makes the system a quasi-real-time detection and monitoring tool.

One of the possible ways to speed up the algorithm is to decrease the number of frequency samples. It can be done by increasing the samples intervals. Thus, it is critical to find the minimum number of frequency samples that produces an image without any deficiency in the quality. To that end, the Nyquist theorem is applied in the frequency domain to find the maximum frequency step (and thus

minimum number of frequency samples) for a reconstructive sampling. It is worthwhile pointing out that this theory is applied in the frequency domain because of the time-limited feature of the received signals.

According to the Nyquist theorem, to theoretically be able to recover the whole data, the sampling step δf should be less than $1/2\tau$, where τ is time-width of the time-limited signal. If the Nyquist criterion is not satisfied (under-sampling), a portion of the data will be missed causing overlapping of the reconstructed signals and resulting in an image with wrong and/or multiple targets. Oversampling (sampling with higher rate than the Nyquist rate) improves resolution and helps avoid overlapping, but requires additional time for measurements and processing.

By considering the time-width of the received signals equal to the data acquisition time, which is roughly around (8 ns) in the considered imaging domain, the sampling step is:

$$\delta f < \frac{1}{2\tau} = 62.5 \text{ MHz}, \tag{3.23}$$

and according to the signal bandwidth *B*, the minimum number of samples is:

$$n_s > \frac{B}{\delta f} = \frac{2.1 \text{ GHz}}{62.5 \text{ MHz}} \approx 34 \tag{3.24}$$

To examine the effect of number of samples on the reconstruction time and image quality, the proposed method is applied on the case depicted in Fig. 3.10 (a) using different numbers of frequency samples. The obtained images are depicted in Fig. 3.11, whereas their quantitative metrics are presented in Table 3.2.

Table 3.2. Effect of number of samples on the image quality

Number of Samples	Q	γ	Δ (mm)	Computation Time (s)	Figure
365	6.50	1.30	1.50	13.0	Fig. 3.11 (a)
100	6.30	1.26	1.50	4.0	Fig. 3.11 (b)
50	6.17	1.24	2.12	2.2	Fig. 3.11 (c)
34	5.96	1.18	2.69	1.6	Fig. 3.11 (d)
25	5.36	0.91	45.9	1.3	Fig. 3.11 (e)
15	3.98	0.75	44.7	0.9	Fig. 3.11 (f)

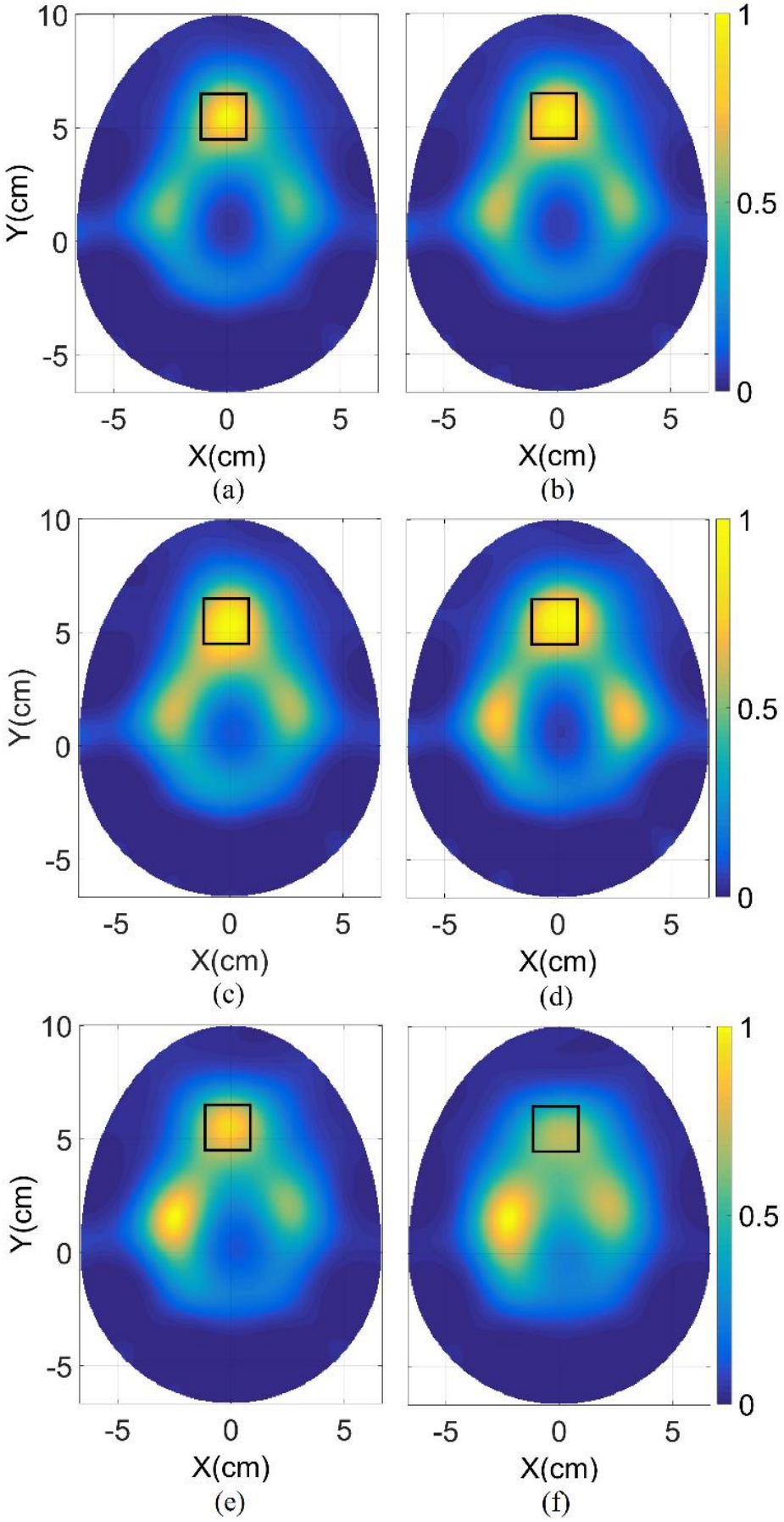

Fig. 3.11. The resultant images from experiments using (a) 360, (b) 100, (c) 60, (d) 34, (e) 25 and (f) 15 frequency samples. Black squares are exact location.

It is clear from Fig. 3.11 and Table 3.2 that reducing the number of frequency samples surely reduces the quality of the obtained image. However, Fig. 3.11 (d) shows that using a minimum of 34 frequency samples (Nyquist rate) can successfully enable the detection of the target in short time deeming the approach quasi-real-time. To further demonstrate the adequacy of the proposed number of frequency samples, the proposed algorithm is applied to the case of small target (Fig. 3.10 (b)) and the simulation data (Fig. 3.6 (d)) using 34 samples. The obtained images in Fig. 3.12 confirm the successful detection of brain injuries with limited number of samples in experiment with small sized injuries and in simulations with more complicated environment.

The total computational time to generate the images with 34 samples is less than two seconds, which makes the algorithm seven times faster than using the full data set (365 samples).

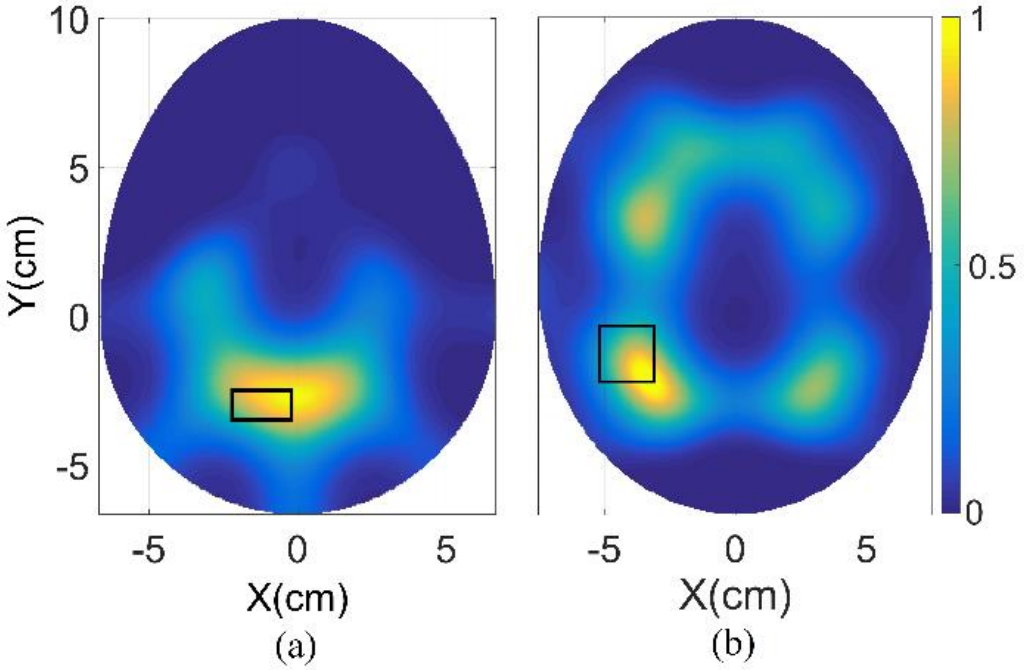

Fig. 3.12. Reconstructed image of the indicated brain injury for (a) measured data and (b) simulation, using 34 frequency samples.

3.4 Comparison

For comparison purposes, two multistatic time domain methods (multistatic delay-and-sum (multi-DAS) [39] and multistatic adaptive microwave imaging (MAMI) [43]) are used to process the same simulated and measured datasets. The multi-DAS and MAMI methods use data-independent weight vectors to estimate the backscattered energy from the focal point inside the imaging region. In comparison to multi-DAS, MAMI uses two steps robust capon beamforming to compensate for the dispersive effects. Fig. 3.13 shows the obtained images using the aforementioned methods to process the simulated and measurement data. It is obvious from Fig. 3.13 that both multi-DAS and

MAMI methods can detect the target in the measured scenario, though with some error in localisation. However, those methods cannot detect the target in the simulated scenario, which has the realistic complex environment with all the head's tissues. The presence of maximum values on the edge of the depicted images implies that those methods cannot completely cancel multiple tissues' reflections and thus the target is buried in the clutter. In comparison, the proposed method can accurately detect the target in the same simulated environment (Fig. 3.6 d).

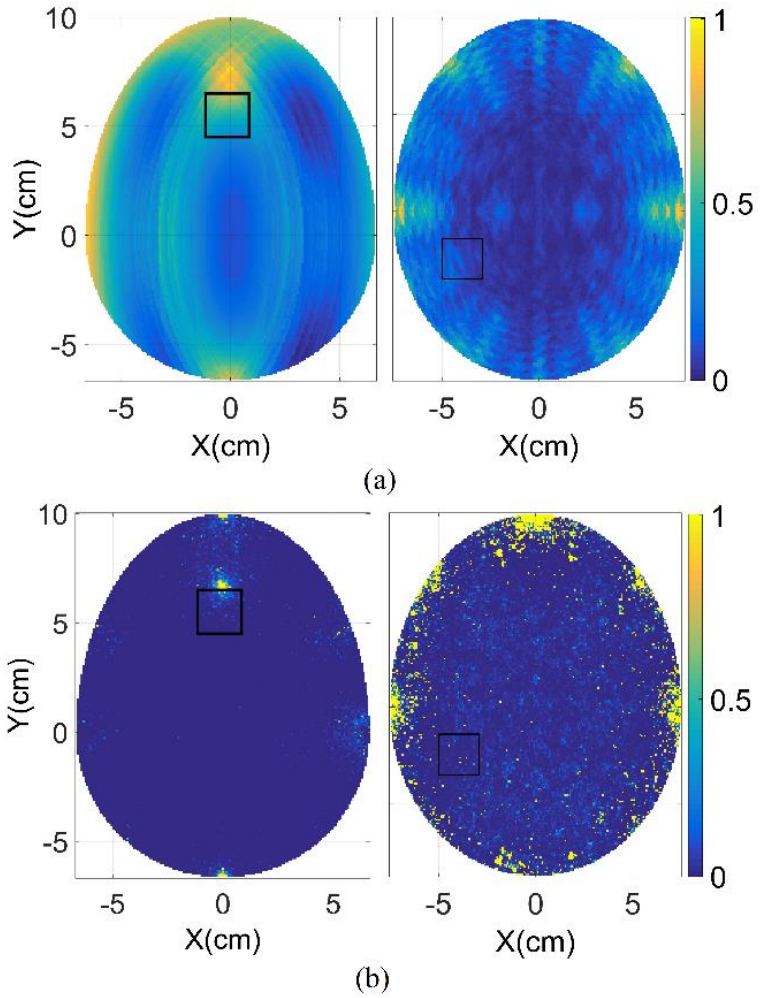

Fig. 3.13. Comparison of reconstructed images using (a) multi-DAS, (b) MAMI. The images on the left side are for measured data and images on the right are for simulated. Black squares illustrate the actual location of the target.

The images' metrics (left images in Fig. 3.13), which show a detected target, obtained using multi-DAS and MAMI with their processing time are calculated and compared with the proposed method counterparts as shown in Table 3.3. The MAMI and multi-DAS methods fail to detect the target as $\gamma<1$ with relatively large values for Δ. For the processing time, it is clear that the proposed method is much faster than multi-DAS and MAMI, which are quite slow due to the need to apply different stages of beamforming. In summary, the proposed method achieves images that are more accurate in a faster way than the existing multistatic time-domain algorithms.

Table 3.3. Performance comparison between proposed, multi-DAS and MAMI methods

Method	Q	γ	Δ (mm)	Computation Time (s)	Figure
Proposed	5.96	1.18	2.69	1.6	Fig. 3.11 (d)
Multi-DAS	1.20	0.3	22.7	19	Fig. 3.13 (a)
MAMI	7.81	0.1	11.4	61	Fig. 3.13 (b)

3.5 Lung cancer detection using monostatic torso rotation system

After validating performance of the proposed algorithm in simulations and experiments for the multistatic head imaging application, it was also tested in monostatic microwave-based torso imaging systems. The system, which is depicted in Fig. 3.14, consists of a rotating platform and is designed for the lung cancer detection scenarios. In this design, a three-dimensional slot-rotated antenna with 0.11 $\lambda \times 0.23\ \lambda \times 0.05\ \lambda$ dimensions (λ is the wavelength of the lowest operating frequency of the antenna), peak front to back ratio of 9 dB and peak gain of 2.6 dBi [61] is used to send microwave signals across one octave band (1.5 to 3 GHz) and collect the backscattered waves using N7081A Agilent portable microwave sensor. A laptop is used for control, processing, and image generation.

The experiments are performed on an artificial phantom which comprises of ribs, muscles, skin, heart, lungs and abdomen block [62] (Fig. 3.15). The phantom is rotated in every 30˚ angle step, while the antenna is fixed to get the mono-static data in 12 positions. The experiments are performed on healthy and unhealthy cases. To mimic the unhealthy case, a sphere-shaped artificial cancer with 1 cm radius (Fig. 3.15 (b)) is inserted inside the torso phantom. The used cancer is made of a mixture of water, corn flour, Gelatin, Agar, Sodium Azaide, Propelene Glysol and NaCl salt. It has the dielectric properties of lung cancer with average dielectric constant of 34 and conductivity of 0.9 (S/m) across the used band. The dielectric permittivity and conductivity of other tissues are in the range of 3 to 7 and 0.04 to 0.3 (S/m), respectively.

The measured S-parameters at 20 MHz frequency steps within the band 1.5-3 GHz at different antenna positions are then utilised by the monostatic imaging algorithm to generate an image of the significant scatterers within the torso. After manually measuring the boundary of the phantom in front of the antenna port, the calculations are performed on the assumed imaging domain depicted in Fig. 3.16. The obtained images of the cross section of the torso in front of the antenna are shown in Fig. 3.17.

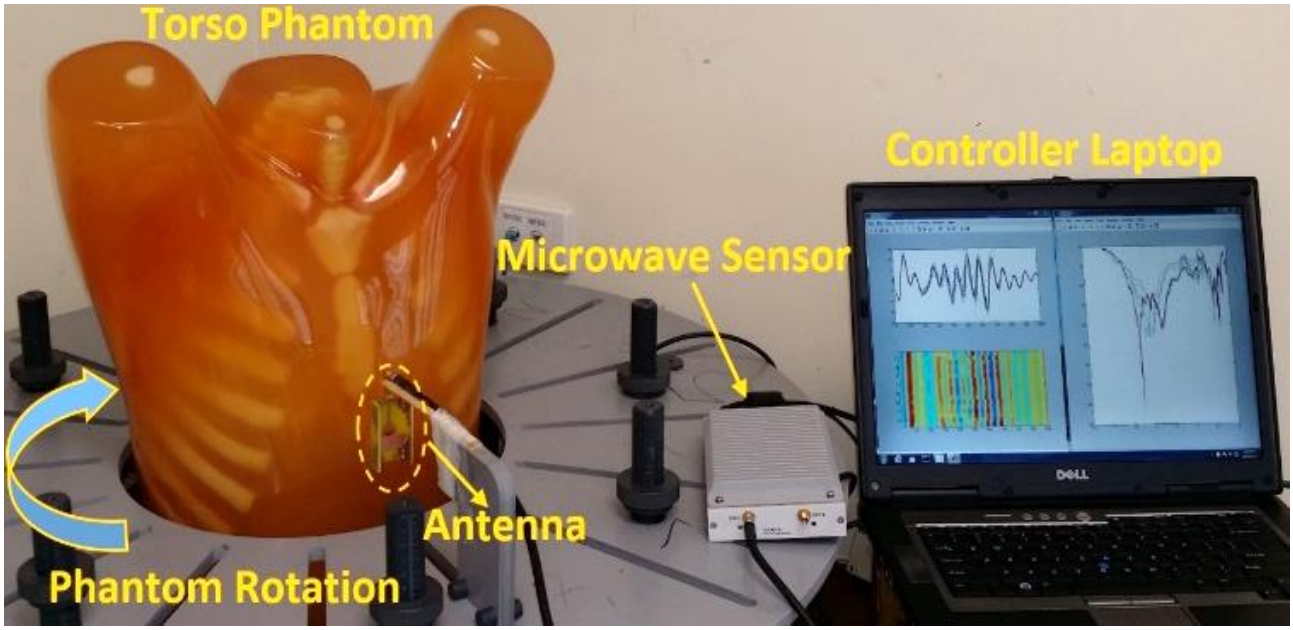

Fig. 3.14. Monostatic torso rotation microwave-based imaging system

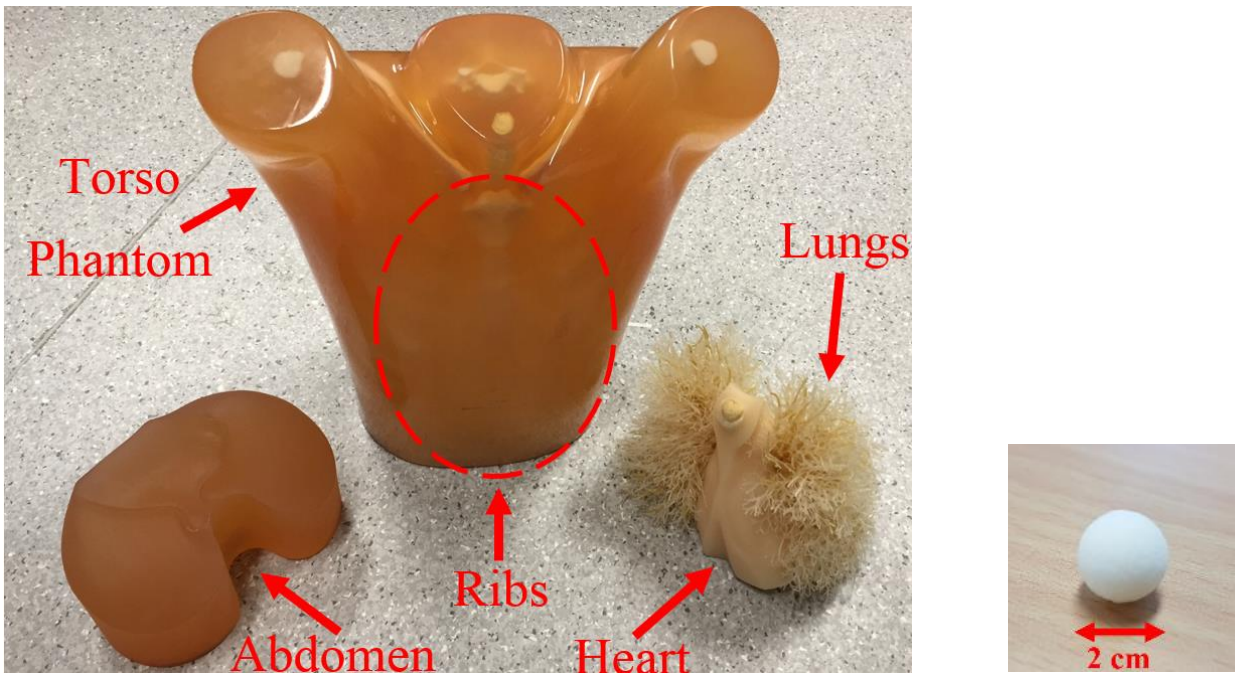

(a) (b)

Fig. 3.15. (a) The utilised torso phantom with its inner organs, and (b) the tumour.

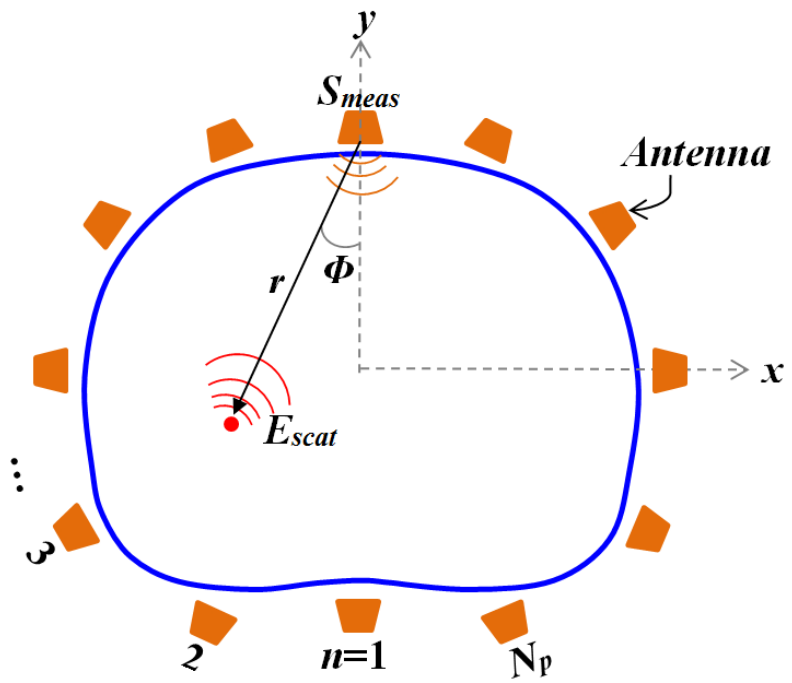

Fig. 3.16. Assumed imaged domain for monostatic torso rotation system.

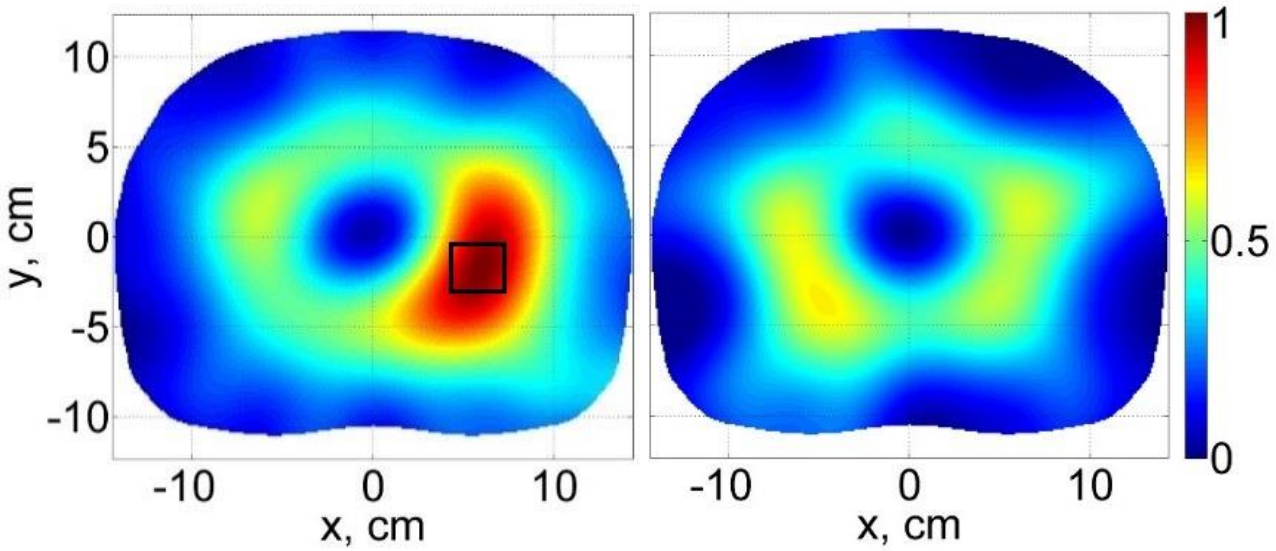

(a) (b)

Fig. 3.17. Imaging results of the torso for (a) infected lung with cancer and (b) healthy lung. Black square shows the exact location of the tumour.

The images are normalised to the maximum value of both the healthy and malignant cases. It is obvious from Fig. 3.17 (a) that the proposed method can precisely detect and localise the cancer with a high resolution inside the complex torso medium. On the other hand, the obtained image for the healthy case, Fig. 3.17 (b), does not show any significant scatterer which confirms the capability of the proposed algorithm in lung cancer detection with the ability of differentiating between healthy and unhealthy cases.

3.6 Summary

A frequency-based processing and image reconstruction algorithm aimed at brain and torso injuries detection has been presented. In the first step, the algorithm uses the average trace subtraction to remove the strong skin interface and background reflections. The second step of the algorithm involves using the first kind of first order Bessel function in the frequency domain to calculate power distributions inside the imaged domain using the measured data. Lastly, superposition of different intensity factors at different antenna locations and different frequency steps is adopted as the final image to illustrate the location of significant scatterers. Thus, the presented approach removes the need to solve time domain or nonlinear inverse problems. The fast computation, simplicity, and stability of the results are the main advantages of the proposed algorithm over the conventional ones. The proposed approach has been validated using realistic simulation and experimental environments. It has been shown that using data from only 34 frequency samples, which meets Nyquist limit, within the band 1.1-3.2 GHz, can successfully detect different sizes of brain injury at different locations. The proposed approach can be considered a quasi-real-time imaging technique as its computation time using a general-purpose computer is less than two seconds. It has also been shown that the proposed frequency domain method is faster, more accurate with better clutter rejection capability than existing multistatic time-domain methods. The proposed imaging algorithm has also been tested on a monostatic torso imaging system for the purpose of lung cancer detection. The obtained images validate the capability of the presented technique to detect an artificial lung cancer inserted into a torso phantom by using monostatic data. However, further modification is required to address some clutter in the obtained images.

Although the proposed imaging algorithm can successfully detect and locate targets in different applications, there are still challenges to be overcome in the use of that technique in realistic scenarios. For example, the required number of antennas for different imaging systems is still unknown. In addition, physical limitation such as the antenna size and available space for antennas limit the usable number of antennas, which affect the accuracy of microwave imaging. Moreover, a set of priori information including the wave's propagation speed, boundary thickness, and location of the imaged object is required, which are subject to vary from patient to patient. Different methods are introduced in the next four chapters to address the aforementioned challenges and enhance the proposed imaging algorithm.

4 CLUTTER REMOVAL TECHNIQUES

In the previous chapter, a microwave imaging algorithm with the capability of detecting medical targets with high permittivity values is presented. In that algorithm, the simple average-trace subtraction technique, which subtracts the calculated average value from the received signals, is used to mitigate the effect of the skin reflections. In that technique, the antennas should be located at the same distance from the skin and the thickness of the outer layer (skin) is supposed to have a uniform thickness around the imaged object. However, as it is shown in the resultant images, this assumption affects the accuracy of the reconstructed images, even in simulations and controlled environments.

In this chapter, different clutter removal techniques are modified for the multistatic frequency-based imaging and a comparison between those methods is provided. Based on the explored performance of different methods in the frequency domain, a hybrid technique, which combines the benefits of average subtraction and entropy-based filtering methods, is proposed.

4.1 Conventional Clutter Removal Techniques

As mentioned in Chapter 2, different imaging algorithms have been developed in recent years to remove the clutter effects during signal pre-processing. The time-widowing (time-gating) [63], which is utilised in breast microwave imaging via space-time [40] and adaptive beamforming [43] techniques is the simplest way to remove the clutter from a raw data in microwave medical imaging. According to the early-time artefact removal approach, the outer layer reflections of the imaged domain are assumed to arrive before the target signal; hence, the clutter can be removed by

filtering the first part of the received signal in the time domain. However, the signal overlap due to the time delay of the wave in multilayer structures of medical applications is a major hindrance to this method. Moreover, time-gating may remove the signals of shallow targets which are close to the outer layer.

To address the aforementioned problem, an entropy-based metric to discriminate between clutter and target signals was introduced [64], [65]. In this case, the signals over a tolerance threshold are considered as a clutter and thus removed. Although the entropy-based windowing algorithm does not affect the target response as much as in the simple time-gating method, it still requires a compensation procedure to restore the erased target signals, especially when early-stage artefact and tumour responses overlap in time [66]. A method that combines entropy-based time windowing and Wiener filtering [67] was proposed to improve the performance of the time-windowing technique [66]. The presented results show better performance than the single entropy based algorithm for a homogeneous breast model. However, the performance of this method in realistic complex scenarios was not investigated.

Analysing the received data in the spatial domain [68] suggests a spatial filtering method, which removes the spatial zero- and low-frequency components corresponding to skin reflections. Assuming equal thickness of the outer layer (skin), reflected signals from the outer layer are either constant or have low-frequency values, whereas the reflected signals from the target inside the imaged domain are variant from the antennas' perspective. Therefore, low-pass finite-impulse-response or spatial delay-line canceler filters can be used to suppress the outer-layer reflections. This method however, also affects the target signals and a careful consideration is needed to repair the data.

The differential approach (DA) is another method which relies on subtracting the healthy and unhealthy scenarios of the same imaged object [45]. Since an image of the healthy case is most probably not available, several modifications to that approach were proposed. For example, the similarity between the left and right side of the head was utilised in the differential imaging presented in [53]. Due to the subtraction process and unknown position of the target, the approach in [53] might result in the presence of ghost targets in the final image and thus cause a wrong detection, especially in multi-target cases.

In [37], the average subtraction method, in which the average measured value (over all antenna elements in an array or at all antenna positions) is subtracted from the received signals by each antenna, was utilised. Subtracting the average value of the signals removes the effects of similar artefacts in different antenna signals due to the symmetric structure of the skin of the imaged

domain. However, applying this method on non-uniform structures such as in head imaging can result in images with false targets.

In the remaining sections of this chapter, a hybrid method that utilizes the benefits of some of the aforementioned techniques for multistatic head imaging application is presented. To that end, those methods are firstly modified to make them applicable in a frequency-domain multistatic imaging algorithm. Then, an investigation into the pros and cons of the available techniques in the head imaging is discussed based on a realistic simulation environment. Analysing the available clutter removal techniques in the frequency domain illustrates their features in that domain and helps develop a new effective approach. The proposed hybrid method combines the best attributes of entropy-based filtering and average subtraction methods. Finally, the ability of the proposed method in clutter removal is tested and validated through simulations and experiments. Addressing the time and frequency overlapping problems are the main merits of the proposed clutter removal method over the conventional ones, which are developed for the time domain.

4.2 Multilayer Reflections

Low frequency microwave signals (around 1-2 GHz) have higher penetration depths inside lossy tissues. Nevertheless, the difference between the dielectric properties of skin tissue layer and air interface causes strong reflections in the received signals. Furthermore, the signals are deteriorated by the multiple reflections from different outer layers (skin, skull, fat, and muscle) due to the dielectric difference between different tissues. One solution to the strong interface reflections is to use a suitable matching medium to fill the air gap between the antennas and the imaged object to improve signal penetration through that object. However, this solution is not preferable due to added practical complications and an added interface that may contribute to reflections and losses especially in patients with dense hair.

To illustrate the effects of different body layers on the transmitted signals, the z-component of the transmitted electric fields into the multilayer head model is calculated using CST simulation environment. The distribution of the field in skin and skull layers in front of an antenna at different time steps are depicted in Fig. 4.1 (a), which illustrates how the field is reflected and trapped between layers. This type of reflection is usually stronger than the target response and thus masks the signals emanated from the target. Therefore, a proper pre-processing method should be adopted to remove the clutter effect of different layers. For this purpose, characteristics of a multilayer slab (Fig. 4.1 (b)) and its effect on the transmitted signal is investigated.

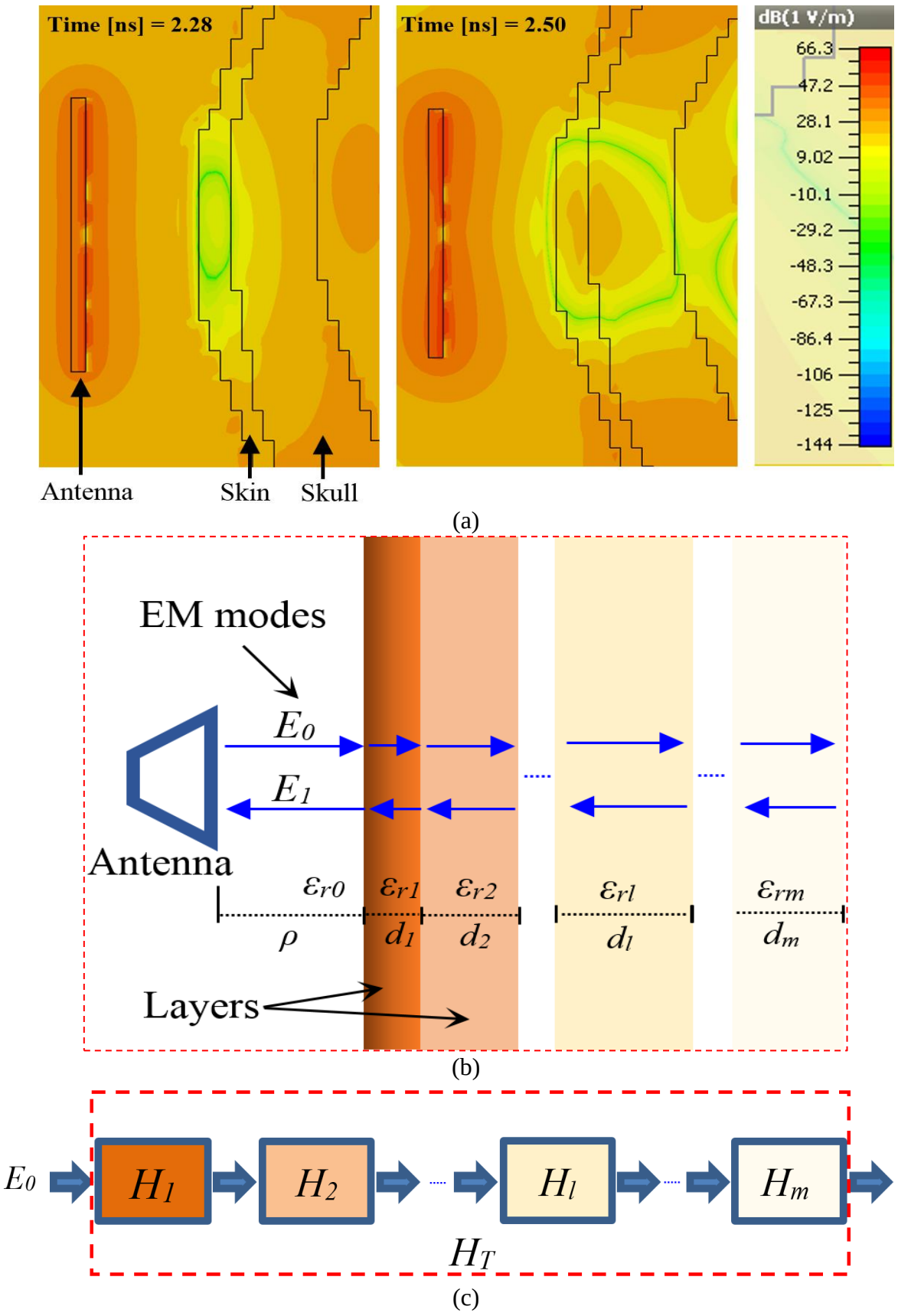

Fig. 4.1. Electromagnetic reflections from different head tissue layers using (a) simulations and (b) a simplified diagram. (c) Model of the multilayer head outer layers.

Assuming a multilayer dielectric slab as a multi-level system (Fig. 4.1 (c)), with *m* independent series connected systems, the impulse response function of *l-th* slab with thickness d_l (l=1 to m) can be derived from [69]:

$$H_l(r,\omega) = -\frac{n_l d_l}{cR_l} e^{\frac{i\omega r}{c}} + \frac{n_l d_l}{c}\frac{R_l^2-1}{R_l}\sum_{p=1}^{\infty}\frac{1}{R_l^{2p}} e^{\frac{i\omega}{c}(r-2pn_l d_l)}, \tag{4.1}$$

where r is the distance of the antenna from the outer layer, ω is the angular frequency, c is the speed of wave propagation in free space, and

$$R = \frac{n_l+1}{n_l-1}, \tag{4.2}$$

where

$$n_l = \sqrt{\varepsilon_{r,l}} \tag{4.3}$$

is dielectric index of refraction and $\varepsilon_{r,l}$ is the relative permittivity of *l-th* slab.

Consequently, the response function of the whole system $H_T(r, \omega)$ can be calculated by multiplication of response functions of m layers:

$$H_T(r,\omega) = \prod_{l=1}^{m} H_l(r,\omega). \tag{4.4}$$

For instance, the response function of a two-layer slab can be written as:

$$H_2(r,\omega) = \frac{n_1 n_2 d_1 d_2}{c^2 R_1 R_2}\left[e^{\frac{i2\omega r}{c}} + (R_2^2-1)\sum_{p=1}^{\infty}\frac{1}{R_2^{2p}} e^{\frac{i\omega}{c}(r-2pn_2 d_2)} - (R_1^2-1)\sum_{q=1}^{\infty}\frac{1}{R_2^{2q}} e^{\frac{i\omega}{c}(r-2qn_1 d_1)} + \right.$$

$$\left.(R_1^2-1)(R_2^2-1)\sum_{q=1}^{\infty}\sum_{p=1}^{\infty}\frac{1}{R_1^{2p}R_2^{2q}} e^{\frac{i2\omega}{c}(r-pn_1 d_1-qn_2 d_2)}\right] \tag{4.5}$$

The exponential parts in the response function represent a delay in the wave propagation in a multilayer slab. In other words, the duration of reflections from a multilayer slab is much longer than the duration of wave propagation in one layer slab with equal thickness. This delay causes layers' and target's reflections to overlap in time and thus creates a clutter in the air gap between the antenna and the outer layer of the imaged object, resulting in the possibility of masking the target. Therefore, applying simple time-windowing methods are not effective in clutter removal from such

a multilayer medium. Additionally, due to the change in the penetration capability of electromagnetic waves with frequency, the produced clutter varies with frequency. This type of clutter, which is caused by overlapping the frequency responses of target and layers, implies ineffectiveness of simple filtering methodologies. However, compensation methods can partly fix the shortfalls of filtering methods as explained later.

4.3 Clutter removal methods in frequency-domain

The performances of five common clutter removal techniques are verified in the investigated domain. Those techniques are modified in this work to make them applicable for multistatic, frequency-domain systems.

4.3.1 Average Subtraction

According to 4.1, the clutter impact is a function of distance of the antenna from the outer layer of the imaged domain, and thickness and properties of its layers. Hence, by assuming that the antennas are located at the same distance from the imaged object's boundary and that the skin, skull, fat and muscles have a uniform thickness around the object, the clutter influences does not vary with the antenna position, whilst target reflections have different impacts on each antenna. In this case, the clutter removal can be achieved by separating a constant value from the signals. One of the simple but effective methods that support this type of clutter removal, is average subtraction in which the average value of signals (S_{avg}) over all receivers (N_a) and transmitters (N_a) is subtracted from each antenna's signal in each frequency sample (S_{meas}):

$$S(f_k) = S_{meas}(f_k) - S_{avg}(f_k)\ , \qquad k = 1 \text{ to } N_f \tag{4.6}$$

where

$$S_{avg}(f_k) = \frac{1}{N_a^2}\sum_{j=1}^{N_a}\sum_{i=1}^{N_a} S_{meas}(R_i, T_j;\ f_k), \quad k = 1 \text{ to } N_f \tag{4.7}$$

Note that the averaging process is not applied over frequency samples, because of the variation of the clutter behaviour with frequency.

Generation of ghost and/or false targets due to the assumption of uniform structure of different layers affects accuracy of the reconstructed images using this method.

4.3.2 Differential approach (DA) type A

This method also assumes an identical distance between the antennas and the imaged domain. In this method, the clutter is removed by subtracting two adjacent traces:

$$S(R_i, T_j) = S_{meas}(R_i, T_j) - S_{meas}(R_{i-1}, T_{j-1}) \tag{4.8}$$

for i, j = 1 to $\frac{N_a}{2}$ with $R_0 = R_{N_a}$, $T_0 = T_{N_a}$

$$S(R_i, T_j) = S_{meas}(R_i, T_j) - S_{meas}(R_{i+1}, T_{j+1}) \tag{4.9}$$

for $i, j = \frac{N_a}{2}+1$ to N_a with $R_{N_a+1} = R_1$, $T_{N_a+1} = T_1$

The advantage of this method over average subtraction is the assumption of constant thicknesses of the layers in front of two adjacent antennas rather than the whole imaged domain, which is more realistic. However, this method creates ghost targets due to the subtraction process.

4.3.3 Differential approach (DA) type B

Due to the anatomically symmetrical structure of the human head over the left and right sides, the interface reflections are almost identical in symmetrical antenna locations on the left and right sides of the head. Therefore, another type of DA can be developed by performing subtraction over two symmetrical antennas:

$$S(R_i, T_j) = S_{meas}(R_i, T_j) - S_{meas}(R_{N_a+2-i}, T_{N_a+2-j}) \tag{4.10}$$

for i, j = 1 to N_a , with $R_{N_a+1} = R_{\frac{N_a}{2}+1}$, $T_{N_a+1} = T_{\frac{N_a}{2}+1}$ and $R_{\frac{N_a}{2}+1} = R_1$, $T_{\frac{N_a}{2}+1} = T_1$.

The difference between the two differential methods is in the selection of antennas for subtraction. In *DA–A*, signals of each pair of neighbouring antennas are subtracted from each other, while in *DA–B*, the signals from any pair of antennas symmetrically facing each other are subtracted. However, the symmetrical subtraction also causes ghost targets. The ghost targets caused by *DA-A* are spread over the image near the antennas' locations, whereas *DA-B* produces mirrored ghost targets in the left or right side of the image.

4.3.4 Spatial Filtering

Due to the different distances between the target and antenna positions and by neglecting the effect of layers' thicknesses, the target's effect on each antenna's signal significantly differs from the clutter behaviour from the spatial point of view. To that end, the received signals are analysed in the spatial domain, in which the time/frequency domain signals are transformed to their angular spectrum using 2-D Fourier transform:

$$S(k_x, k_y; f) = \iint_s S_{meas}(x, y; f) e^{-i2\pi(xk_x + yk_y)} dxdy \tag{4.11}$$

where k_x and k_y are spatial frequencies.

In this case, the clutter removal is equivalent to separating spatial zero and low frequency signals from the signals across all the antennas. This step can be performed using a spatial notch filter [69]:

$$H_{NF}(k) = \frac{1 - e^{-i2\pi k}}{1 - \alpha e^{-i2\pi k}}, \tag{4.12}$$

in which $0<\alpha<1$ determines the width of the filter notch. It is worth mentioning that the average subtraction method is a special kind of spatial filtering, in which the single spatial frequency component (zero-frequency) is removed without changing other components.

Although this method might appear to have more advantages than the average subtraction, the time overlapping is not considered in the Fourier calculations. In addition, finding the optimum value for α needs initial knowledge about the properties and dimensions of the layers and thus makes this method difficult to use.

4.3.5 Entropy-based Filtering

According to the fact that the reflections from the outer layers are stronger than the target signals, the clutter can be removed by applying a proper filter. However, as mentioned in the previous section, the time and frequency overlapping features of the measured data make it difficult to discriminate between the clutter and target signals. In that regard, entropy metric is defined, in which the amount of uncertainty of the data is calculated by summing the probability density function (P) of the measured data over all antennas:

$$H_\alpha(f_k) = \frac{1}{1-\alpha} log\left(\sum_{j=1}^{Na} \sum_{i=1}^{Na} [P(R_i, T_j; f_k)]^\alpha\right) \tag{4.13}$$

H_α is known as the αth-order Renyi entropy [70] and

$$P(R_i, T_j; f_k) = \frac{|S_{meas}(R_i, T_j; f_k)|^2}{\sum_{j=1}^{Na}\sum_{i=1}^{Na}|S_{meas}(R_i, T_j; f_k)|^2} \tag{4.14}$$

which satisfies $P(R_i, T_j; f_k) \geq 0$ and $\sum_{j=1}^{Na}\sum_{i=1}^{Na} P(R_i, T_j; f_k) = 1$ for $k = 1$ to N_f.

The Renyi entropy (H_α) assigns large values (maximum *log* N_a) to clutter signals (high value signals), while target signals (low value signals) are diminished. After discriminating between target and clutter signals, the clutter can be removed by filtering high values of $e^{H(f)}$ which is between 1 and $(N_a)^2$:

$$S(R_i, T_j; f_k) = \begin{cases} 0 & e^{H(f_k)} \geq N_0 \\ S_{meas}(R_i, T_j; f_k) & otherwise \end{cases}, \tag{4.15}$$

where $1<N_0<(N_a)^2$ is the entropy threshold, which is suggested to be half of the number of received signals [64].

Applying the entropy-based filtering in the frequency domain makes it resilient to time delay and overlapping. However, filtering some frequency components does not remove the clutter in other frequencies. In fact, this method only removes strong reflections without manipulating the low value clutter signals, which might be in the same range of the reflections emanating from the target. In addition, due to the frequency response overlapping, entirely eliminating a frequency component also erases a portion of the target data. Therefore, the removed target data should be restored.

4.4 Methods comparison

To evaluate the effectiveness of the aforementioned methods in removing the clutter in realistic imaging scenarios, they are applied to process signals collected using the aforementioned simulation environment for head imaging in the previous chapter. Those pre-processed signals are then compared with the target response in a clutter-free (homogeneous) environment. This environment is created in the simulations by changing the material properties of the imaged domain to be a constant value, which is equal to the average value of all the tissues.

The effect of the clutter removal techniques on the target response can be visually inspected using the point spread function (PSF), which can be defined in functional terms as the spatial domain version of the transfer function of the imaging system [71]. The PSF is calculated by finding the response of the imaging system due to a point target as a function of its spatial variations. Thus, the

PSF can be presented by the 2D spatial domain transformation of the received signals at all possible target positions. In the head imaging case, the target (bleeding) is considered as a point target and the PSF of a target in a homogeneous medium is calculated. To that end, the 2D Fourier transformation of received signals are calculated according to the down-range and cross-range resolutions of each antenna and the total PSF is calculated by superposing all of the PSFs according to their corresponding positions:

$$PSF(R_i, T_j; x, y) = \int_{k_r} \int_{k_u} S(R_i, T_j; f) e^{i(k_u u + k_r r)} dk_u dk_r \tag{4.16}$$

$$PSF_{total}(x, y) = \sum_{i=1}^{Na} \sum_{j=1}^{Na} PSF(R_i, T_j; x, y), \tag{4.17}$$

where k_u and k_r are spatial cross-range and depth-range angular frequencies. The image of PSF from clutter-free data is used as a benchmark for a visual comparison with clutter removal techniques.

To quantitatively compare the target response from the ideal clutter-free environment and other pre-processed signals, the maximum cross-correlation between those signals and the ideal response is calculated as a measure of similarity with the clutter-free signal. To that end, the signals are transformed to spatial domain using the Fourier transformation:

$$s(R_i, T_j; r) = \mathcal{F}\{S\} = \int_f S(R_i, T_j; f) e^{i2\pi \frac{f}{v} r} df. \tag{4.18}$$

where v is the wave speed in the medium. The maximum cross-correlation (C_{max}) for each signal is then calculated by

$$C_{max}(s_t, s) = max[(s_t * s)(\rho)] = max[\int_{-\infty}^{\infty} {s_t}^*(r)\, s(r + \rho)\, dr] \tag{4.19}$$

where s_t and s are the target and pre-processed signals, and (*) denotes the convolution operation along the r direction. In (4.19), the receiver and transmitter indexes are removed for simplicity. The calculated cross-correlations are then normalised to (0-1) range, using their autocorrelations:

$$C_{norm}(s_t, s) = \frac{C_{max}(s_t, s)}{\sqrt{C_{max}(s_t, s_t) C_{max}(s, s)}}. \tag{4.20}$$

There would be N_a^2 normalised cross-correlation values for the recorded multistatic data with N_a antennas. In order to have a number to compare the different methods, the average normalised cross-correlation value over all signals is calculated for each method by:

$$\eta = \frac{1}{N_a^2}\sum_{j=1}^{Na}\sum_{i=1}^{Na} C_{norm}\big(s_t(R_i, T_j; r), s(R_i, T_j; r)\big) \tag{4.21}$$

The average normalised cross-correlation, η, changes from 0, for fully distorted signals, to 1, for ideal scenarios.

Fig. 4.2 shows the total PSF (left side images) and the corresponding calculated η before and after applying the clutter removal techniques. The spatial domain signals for a sample signal received by an antenna facing a 4 cm target inside the used head models are also provided in Fig. 4.2. Fig. 4.2 (a) shows the reference signal recorded in the homogeneous region. It is obvious from Fig. 4.2 (b) that the clutter due to outer layer reflections is much stronger than, and thus masks, the target response in the raw data. The corresponding low average cross-correlation value (η = 0.37) also proves that the multilayer structure of the realistic head strongly distorts the received signal. It is obvious from Fig. 4.2 (b) that the target cannot be revealed by applying time-windowing methods, due to the signal overlapping in time. Using the average subtraction method in the frequency domain reveals the target response at its real location (Fig. 4.2 (c)). In fact, applying the average subtraction approach at each frequency component compensates for the time-overlapping due to the penetration of wideband signals in the heterogeneous medium by considering the penetration ability of microwave signals at each frequency. However, there are other strong responses, which cause a reduction in the corresponding value for η and therefore the appearance of ghost targets in the final image. The two differential methods (Fig. 4.2 (d) and (e)) are not well successful in removing early-stage clutters. The spatial filtering (Fig. 4.2 (f)) on the other hand mitigates early-stage clutters, but the level of the target signal is decreased to the level of delayed clutters causing a low value for the η and the appearance of ghost targets in the final image. As shown in Fig. 4.2 (g), the early stage and delayed clutters are mitigated using the entropy-based method, but the target signal is still dominated by clutters. The PSF images and calculated values of η show that the average subtraction and entropy-based methods return signals that almost resemble the target signal. It can be concluded from those results that only a limited part of the target data is removed by the average subtraction and entropy-based methods, while the other methods corrupt the target response significantly.

To better highlight the effects of the various types of clutter rejection algorithms, they are used to reconstruct 2D images. The accuracy of those images in detection and locating an emulated brain injury is then verified. The reconstructed images are shown in Fig. 4.3.

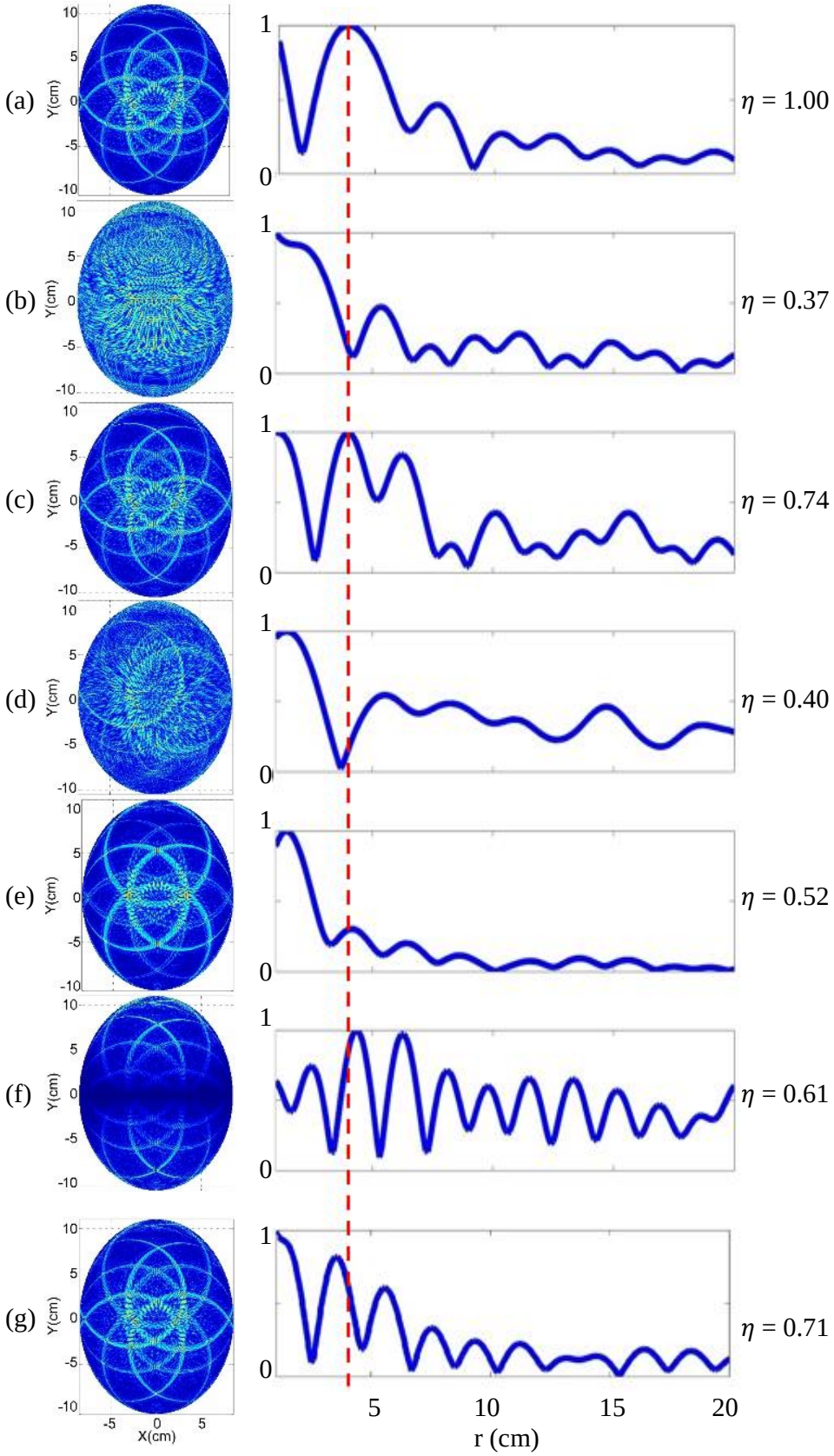

Fig. 4.2. PSF, spatial domain signals and corresponding normalised cross-correlation values for (a) reference signal, (b) raw signal, and after using (c) average subtraction, (d) differential approach-A, (e) differential approach-B, (f) spatial filtering, and (g) entropy-based filtering. The vertical red dashed line shows the exact location of the target.

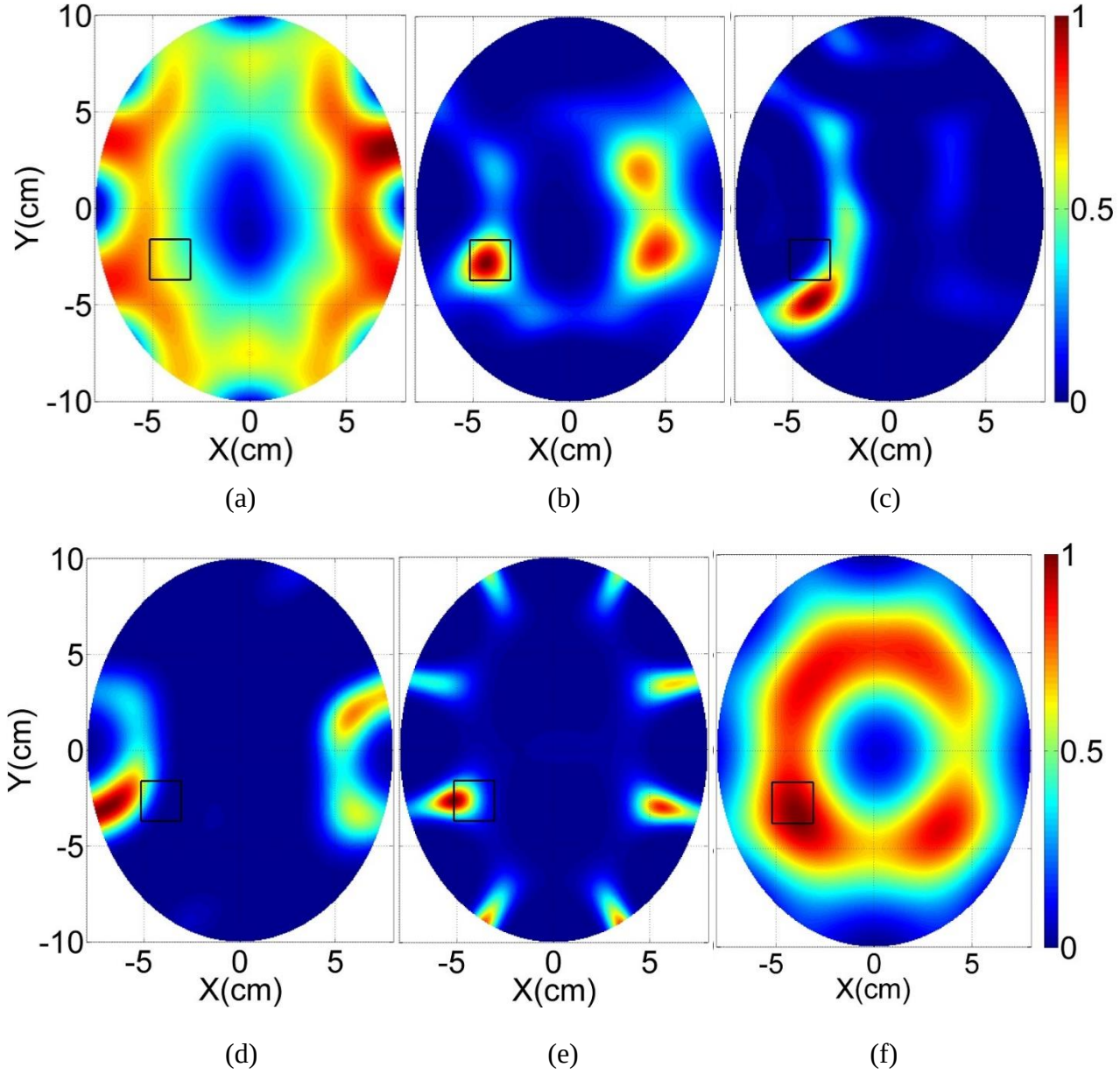

Fig. 4.3. Reconstructed images (a) without applying clutter removal techniques, and after using (b) average subtraction, (c) differential approach-A, (d) differential approach-B, (e) spatial filtering, and (f) entropy-based filtering. Black rectangles show the exact location of the target.

To ease the detection process and comparison between different methods, the images' intensities are normalised to the highest obtained intensity in each image. Fig. 4.3 (a) shows the obtained image without applying any clutter removal technique. This image demonstrates how the target is completely masked by the strong clutter. As expected, average subtraction method (Fig. 4.3 (b)) can locate a target, but also produces false targets due to the slightly different effects of the clutter on different antennas. Fig. 4.3 (c) and (d) show the results of the two differential methods. Both of the methods have small errors in locating the target, which can be interpreted as the effect of the

subtraction step on the target signals. In addition, the reconstructed images are affected by ghost targets in the opposite side of the real target, especially in method *B* of this approach (Fig. 4.3 (d)). The resulted image for spatial filtering with α=0.9 is shown in Fig. 4.3 (e). This best value for α is selected based on trial-and-error approach on the resultant images. This method can reveal the target; however, the presence of a ghost targets and small error in localisation degrades its efficiency. Comparing this method with the average subtraction shows that filtering low spatial frequencies effectively mitigates the ghost targets, but shifts the target's location, which means a significant effect on the target response. As shown in Fig. 4.3 (f), the entropy-based filtering significantly reduces, but does not completely remove the clutter. The resultant effect of non-filtered frequencies is a reconstructed image that has a halo along the target location.

In summary, the spatial domain signals and reconstructed images show the enhanced capability of several known time-domain techniques when modified to operate in the frequency domain. The serious problems associated with those techniques, when applied to remove clutters in the time-domain analysis such as time overlapping, are alleviated when they are modified to frequency domain methods.

4.5 Proposed hybrid method

Although all the aforementioned methods are effective in clutter removal for simple one homogeneous layer structures, they often fail in removing the clutter from multi-layer heterogeneous structures. This mainly happens due to the incomplete removal of clutter or removing part of the target response during the filtering procedure. To tackle these problems and in order to take better advantage of the available methods, a hybrid method is proposed to avoid the weaknesses of current techniques.

As explained earlier, the average subtraction method tries to remove the clutter by separating an average value from all the antennas in every frequency step after assuming a uniform thickness for different layers seen from different positions or angles. The real non-uniform thickness of the layers affect accuracy of the final image by producing ghost targets. On the other hand, the entropy-based method tries to filter out the clutter that dominates the recorded signals; however, the incomplete removal of the clutter causes a halo effect in the image resulting in an inaccurate or difficult detection of the target. Hence, the proposed hybrid method aims to combine the two aforementioned methods for the effective utilization of their benefits, while at the same time overcoming their shortfalls. In addition, any deletion of the target signal in the utilised entropy-based filters is compensated by replacing the over-threshold signals with the average value of the signals passing the filter.

In the hybrid method, the raw scattered signals are firstly filtered in the spatial domain by subtracting their average value. Then, the probability density function of the filtered signals is calculated for every frequency step:

$$P(R_i, T_j; f_k) = \frac{[S_{meas}(R_i,T_j;f_k) - S_{avg}(f_k)]^2}{\sum_{j=1}^{Na}\sum_{i=1}^{Na}[S_{meas}(R_i,T_j;f_k) - S_{avg}(f_k)]^2}, \quad (4.22)$$

for k = 1 *to* N_f . Then, the entropy criterion (H) is calculated by using the third order of Renyi entropy (α=3) which is known to be the best entropy for a broad class of signals [70]:

$$H_3(f_k) = -\frac{1}{2}\log\left(\sum_{j=1}^{Na}\sum_{i=1}^{Na}\left[P(R_i, T_j; f_k)\right]^3\right) \quad (4.23)$$

The entropy-based filtering (4.19) is then applied to find the high value signals. Finally, the filtered over-threshold signals are replaced by the average value of the signals that passes from the filter (S^*_{avg}):

$$S(R_i, T_j; f_k) = \begin{cases} S^*_{avg}(f_k) & e^{H(f_k)} \geq N_0 \\ S_{meas}(R_i, T_j; f_k) & otherwise \end{cases}, \quad (4.24)$$

The resultant images using the hybrid method on the same raw data utilised to create Fig. 4.2 and Fig. 4.3 is demonstrated in Fig. 4.4. The resulted PSF and signal from the proposed hybrid method (Fig. 6 (a)) shows that it effectively cancels early- and late-stage clutters. In addition, this method has negligible effect on the target response compared to the other investigated methods, as it very well resembles the reference PSF.

To investigate the performance of the proposed hybrid method in removing the clutter in head imaging and compare its effect on the obtained image using other techniques, the signal-to-noise ratio (SNR) [72] is used as a metric to quantify the obtained images:

$$SNR = 10\ log_{10}\left(\frac{I_t - I_b}{C_b}\right) \quad \text{dB}, \quad (4.25)$$

where I_t and I_b are the mean values of the detected target and background regions, respectively, and C_b is the standard deviation of the background. *SNR* reflects the contrast between the target and background. Higher values of *SNR* for a reconstructed image using a certain algorithm means better clutter removal and thus more accurate detection.

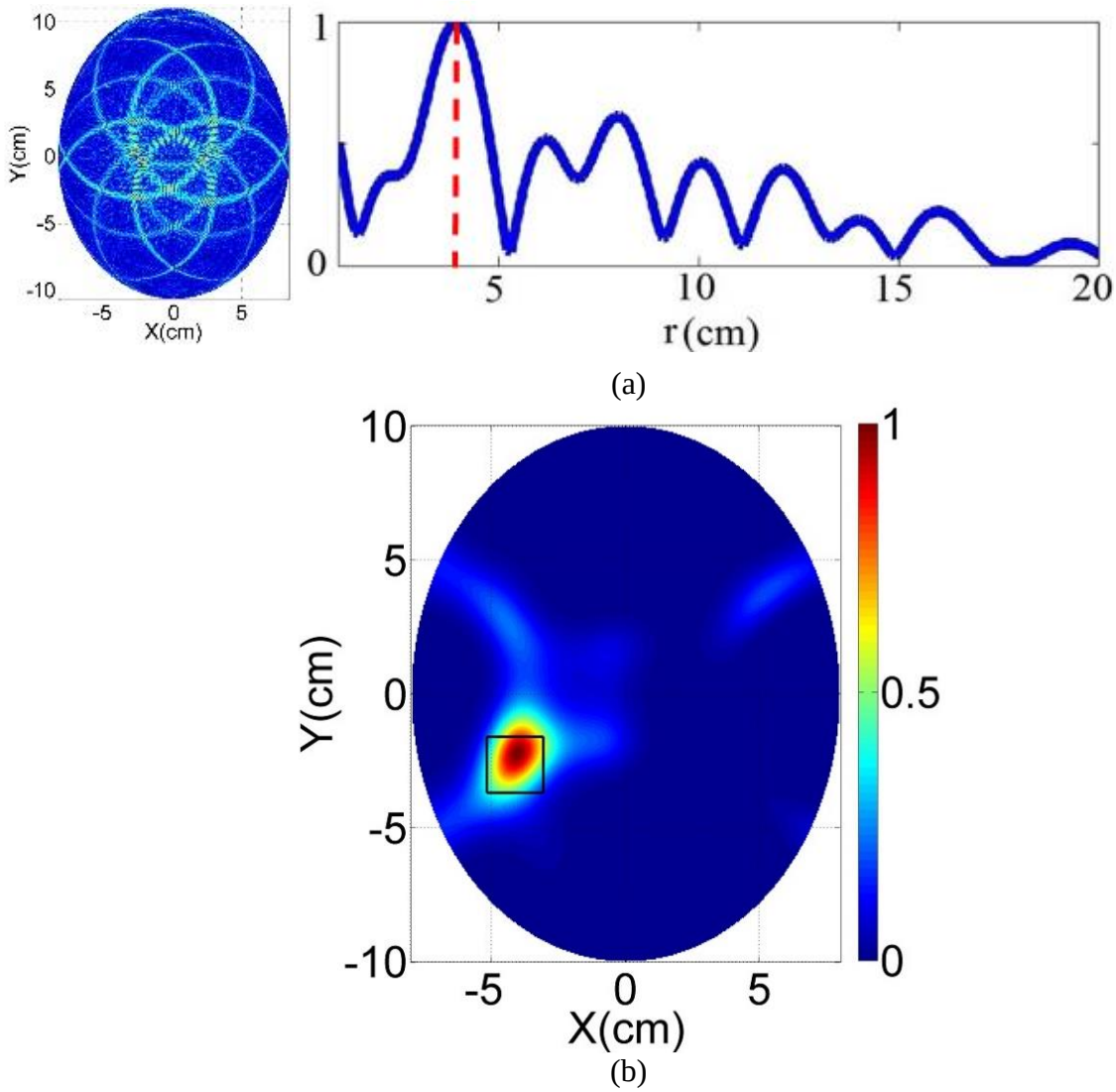

Fig. 4.4. (a) PSF, typical spatial domain signal and average value of normalised cross-correlation, and (b) reconstructed image, using the hybrid method. Black rectangles show the exact location of the target.

Also, for performance evaluation of a clutter removal method in target's data manipulation, Δ, the distance between the real center and the center of the detected target is calculated by (3.22). Lower Δ means that the clutter removal algorithm has lower effect on the target's data and Δ=0 represents an ideal scenario, i.e. accurate localisation of the target. The above mentioned parameters are calculated for the images in Fig. 4.3 and Fig. 4.4 (b), and listed in Table 4.1.

Table 4.1. Comparison between performance of the proposed and other techniques

Method	*SNR* (dB)	Δ (mm)	Figure
Proposed (Hybrid)	5.9	2.2	Fig. 4.4 (b)
Average subtraction	2.5	5.7	Fig. 4.3 (b)
Differential approach-A	5.5	21.5	Fig. 4.3 (c)
Differential approach-B	4.8	34.5	Fig. 4.3 (d)
Spatial filtering	2.6	11.6	Fig. 4.3 (e)
Entropy-based filtering	0.8	9	Fig. 4.3 (f)

The *SNR* values in this table show that the proposed hybrid method has obviously higher contrast and is the most successful method in the clutter removal. Moreover, according to the values of Δ, the hybrid method is the most accurate method in locating the target. The more accurate results of the hybrid method than the single entropy-based filtering method demonstrates the effectiveness of the adopted data compensation. It is also obvious from Fig. 4.4 that the proposed method not only removes the clutter, but also strongly reduces the ghost targets produced by the time and frequency overlaps. From the physical point of view, electromagnetic waves that pass through similar tissues with similar permittivity values have a high correlation and hence deliver lower variogram values, while the waves that pass through different tissues are uncorrelated and deliver higher variogram values. The adopted approach in replacing the high value signals with the average value helps in the partial compensation for any removal of part of the target data.

4.6 Experimental validation

To experimentally validate the proposed hybrid method for clutter removal, it is applied to the recorded data from the mentioned head imaging setup in Chapter 3 – Section 3.2.2. To compare the proposed method with the previously mentioned algorithms, the reconstructed images using those methods along with their resultant metrics are depicted in Fig. 4.5. As can be observed from Fig. 4.5 (a), the proposed method can successfully remove the effect of the clutter and thus accurately detect the targets in both of the investigated cases. A comparison between the metrics values indicate that the resultant images from the proposed hybrid method deliver the highest value of SNR and lowest value of Δ for both of the investigated experimental scenarios. These metric values confirm superiority of the proposed method in clutter rejection compared with other methods in the investigated multistatic frequency-domain microwave imaging system.

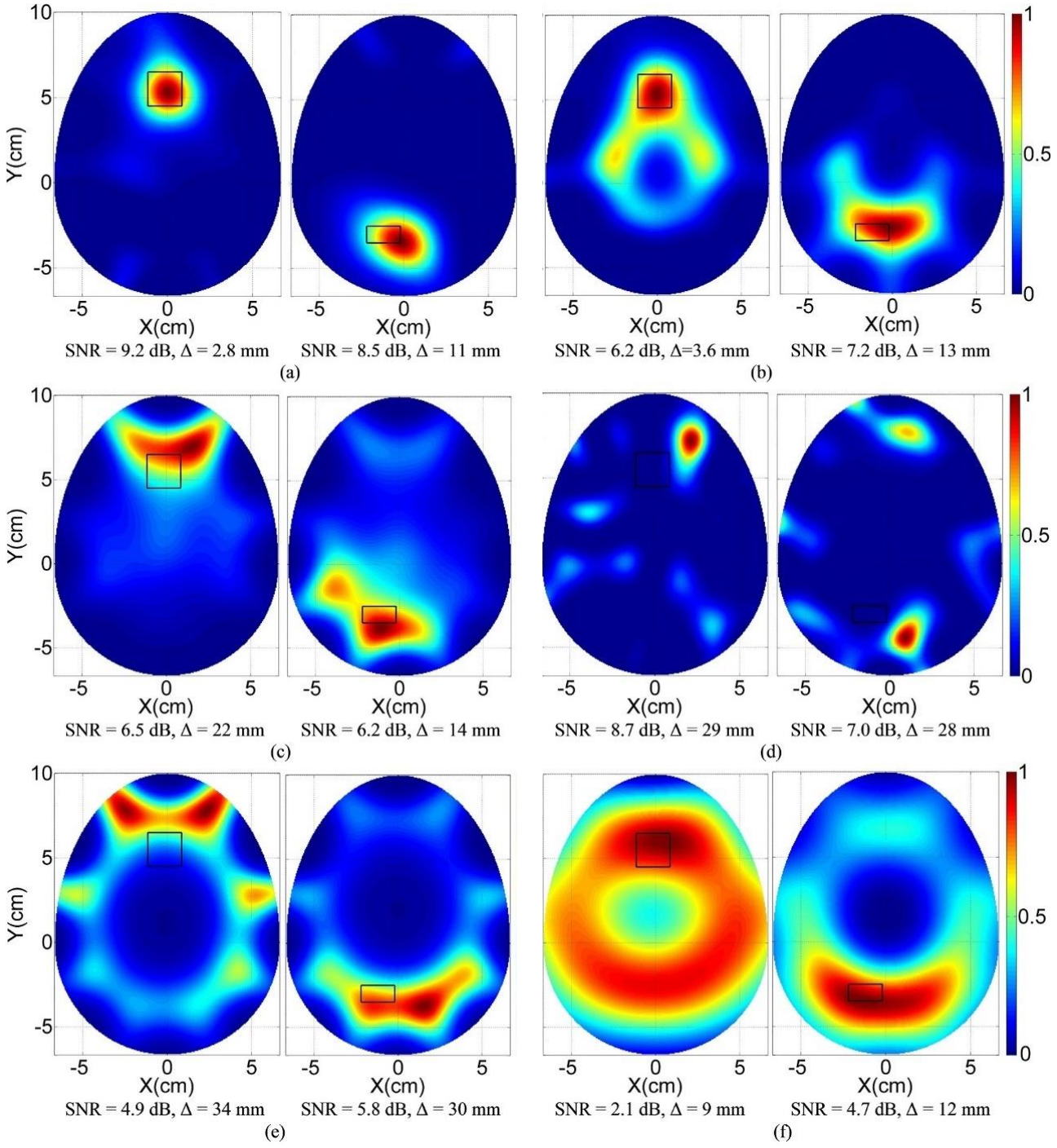

Fig. 4.5. Experimental results using (a) the proposed hybrid method, (b) average subtraction, (c) differential approach-A, (d) differential approach-B, (e) spatial filtering, and (f) entropy-based filtering. Black rectangles show the exact location of the target. Left side images are for 2 × 2 × 2 cm3 bleeding in the head phantom and right side images are for 2 × 1 × 1 cm3. Black squares show the exact location of the bleeding.

4.7 Summary

A hybrid method to remove the clutter effects in microwave medical imaging has been presented. Due to the complex structure of the human body, time and frequency overlapping between target response and clutters causes false positive or negative detection when using traditional clutter removal techniques. The proposed hybrid method mitigates the effect of the clutter in all frequencies by applying the average subtraction in every frequency step and then using a modified entropy-based filter to remove the strong reflections from the skin, skull, fat and muscle layers. It has been shown that some deficiencies of the adopted methods in the time domain, such as time overlapping, can be alleviated when they are modified for use in the frequency domain. The performance of the proposed method has been tested on realistic head phantom. The presented results indicate superiority of the proposed hybrid method in removing the clutter and ghost targets therefore producing accurate images in microwave head imaging.

5 Improved Radar-Based Microwave Medical Imaging Using Extended Virtual Antenna Array

As it is shown in Chapter 3, the accuracy of microwave imaging is highly dependent on the number of antennas used for data acquisition. The number of antennas is usually determined based on the antenna size, available space for antennas, and acceptable hardware complexity (switching and processing) to use as many antennas as practically possible. For example, authors in [73], use 40 antennas distributed on five elliptical rings of eight antennas for breast imaging. In [38], the system uses up to 200 antenna positions for a 3D monostatic breast imaging system. In some other systems, 32 and 16 antennas are utilised for multistatic breast imaging, respectively [9]-[12]. However, the information available in microwave imaging is essentially limited and cannot be increased by just increasing the number of antennas. Hence, for a given accuracy, increasing the number of antennas beyond a specific value does not convey independent information [75], [76]. Moreover, the limited number of antennas in a multistatic array, which is determined by the feasible space between the antennas, mutual coupling, and hardware complexity, does not allow the designer to make the best use of multistatic techniques.

To overcome these shortcomings with the aim to improve the accuracy and quality of reconstructed images, the concept of virtual antenna array to increase the effective number of antenna elements is proposed and explained in this chapter. In addition, the information correlation coefficient (*ICC*)

[74] is proposed to find the maximum and minimum number of antennas required for the proposed virtual array concept to work. The presented method is tested via simulations and experiments using the aforementioned multistatic-radar-based head imaging system.

5.1 Virtual Array Concept

The virtual antenna concept is well known in direction finding techniques that are used in communication and navigation systems [77]-[80]. Through-the-wall and MIMO imaging systems [81], [82] also use virtual phased array and switched-antenna-array techniques in planar and linear bistatic configurations to enable using fewer antennas. The virtual antenna array can increase the degree of freedom of a multistatic array by creating a larger array using only a small number of real antennas. To that end, the data transformation (mapping) from a real antenna array onto the virtual array was performed by using different algorithms, such as MUSIC and spatial smoothing [79], [83]-[85]. A virtual pseudo-monostatic subarray architecture was also proposed in [86] for planar radar imaging.

In this work, a spatial statistical technique based on the Kriging method [87] is derived and utilised to build a virtual antenna array with larger number of antennas than the real array. Efficacy and accuracy of the Kriging method in estimating electromagnetic fields is demonstrated in [88]-[94]. While other interpolators, such as Lagrangian polynomials and least-square methods, have been successfully used in different applications [95], Kriging method considers the spatial structure of the variables, which is essential in physical applications. In addition, this method provides information about the local behaviour of variables making it an ideal candidate to predict electromagnetic wave behaviour in small domains. Unlike the previous virtual array techniques such as MUSIC-like methods, the proposed method can perfectly handle correlated (or highly correlated) signals, which usually arise in biomedical applications due to multipath propagation. In addition, unlike the spatial smoothing technique, which is only applicable in bistatic linear uniformly spaced arrays, the Kriging-based method can be applied on different array configurations.

For the efficient use of the statistical interpolator, a model for the correlation function of the electric fields is derived. The designed statistical model provides the local spatial structure of the microwave signals at different locations around the imaged domain. Due to the statistical nature of this model, more information can be extracted from the data. The estimated values using this model are inferred at the desired locations. The virtual array's outputs are then processed using the frequency-based imaging algorithm to get improved image quality and detection accuracy.

5.1.1 Statistical Model

Fig. 1 shows the scenario of wave propagation between two antennas in a multistatic head imaging system. The foundation of the model is the estimation of the wave propagation behaviour in the imaged domain. By applying the derived model, the signals at any location around the imaged domain can be predicted to configure the desired virtual array.

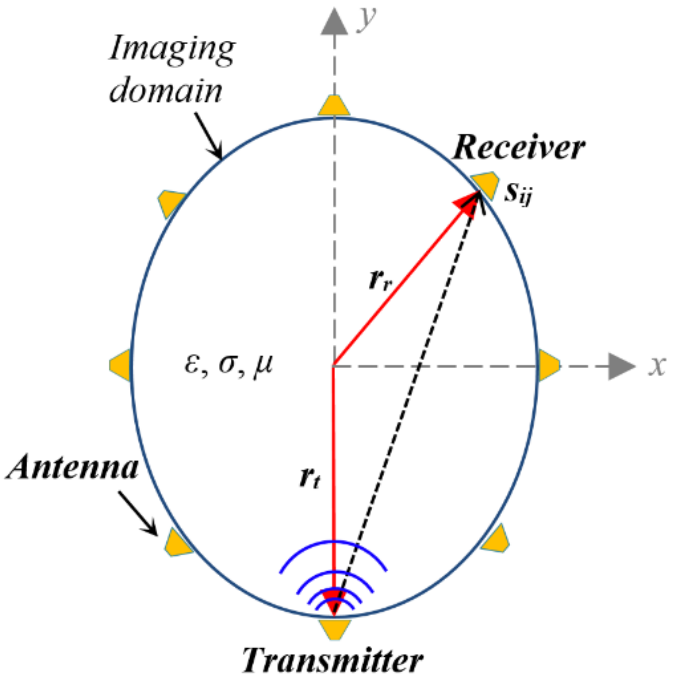

Fig. 5.1. Wave propagation in a round-shaped microwave imaging system.

Consider a wideband multistatic antenna array consisting of N_a elements that enclose the head. Each antenna works as both a transmitter and receiver of N_f frequency samples. Assuming the system a black-box with received signals $s = \{s_{11}, s_{12}, s_{13}, \ldots, s_{NaNa}\}$ as system responses, and transmitter and receiver locations ($\vec{r_t}$ and $\vec{r_r}$, respectively) as system variables, the relationship between responses and variables of the system is required. Generally, the structure of that relationship is unknown. Therefore, a suitable approximation to the true relationship should be considered. The most common form is low-order polynomials (first or second-order) which can be used for a wide variety of real physical applications [94], [95]:

$$s(\vec{r_t}, \vec{r_r}) = w_0 + \sum_{i=t,r} w_i \vec{r_i} + \sum_{i=t,r} \sum_{j=t,r} w_{ij} \vec{r_i} \vec{r_j} + e \tag{5.1}$$

where w_i are unknown parameters to be solved, $\vec{r_t}$ and $\vec{r_r}$ are the inputs (transmitter and receiver locations) and e is the error function. In matrix notations, (5.1) can be written as

$$S = Rw + e \tag{5.2}$$

where S is an $N_a^2 \times 1$ vector of received signals from the multistatic array of N_a antennas, $R = [r(\boldsymbol{r}_1), r(\boldsymbol{r}_2), ..., r(\boldsymbol{r}_{N_a^2})]^T$ is a known $N_a^2 \times 7$ location's quadratic function matrix with $r(\boldsymbol{r}_i) = [1, \overrightarrow{r_{t_i}}, \overrightarrow{r_{r_i}}, \overrightarrow{r_{t_i}}^2, \overrightarrow{r_{t_i}}\overrightarrow{r_{r_i}}, \overrightarrow{r_{r_i}}\overrightarrow{r_{t_i}}, \overrightarrow{r_{r_i}}^2]^2$, w is a 7×1 vector of regression coefficients, and e is $N_a^2 \times 1$ error vector. The vector of coefficients estimator $\hat{w}$ can be determined subject to the minimisation of the total sum of squares (*TSS*) of the error, e

$$TSS = \sum_{i=1}^{N_a^2} e_i = (S - Rw)^T (S - Rw) \tag{5.3}$$

Based on the Kriging method [87], the best linear unbiased estimation of w is

$$\hat{w} = (R^T C^{-1} R)^{-1} R^T C^{-1} S \tag{5.4}$$

where $C = [c_{ij}]$ is $N_a^2 \times N_a^2$ correlation matrix with

$$c_{ij} = \rho(\boldsymbol{r}_i, \boldsymbol{r}_j), \quad i, j = 1, ..., N_a^2 \tag{5.5}$$

ρ is the correlation function to be found, and $\boldsymbol{r}_i = \{\overrightarrow{r_t}, \overrightarrow{r_r}\}_i$ indicates ith set of transmitter-receiver locations. The estimated value for an arbitrary set of transmitter-receiver location r_v is then calculated by

$$\hat{S}(\boldsymbol{r}_v) = r(\boldsymbol{r}_v)\hat{w} + c(\boldsymbol{r}_v)^T C^{-1}(S - R\hat{w}) \tag{5.6}$$

where $c(\boldsymbol{r}_v) = [C(\boldsymbol{r}_v, \boldsymbol{r}_1), C(\boldsymbol{r}_v, \boldsymbol{r}_2), ..., C(\boldsymbol{r}_v, \boldsymbol{r}_{Na^2})]^T$.

5.1.2 Correlation Function Design

Since the proposed technique exploits the spatial correlation of data to build interpolations, the choice of the correlation function highly affects the quality of the estimation. Different correlation functions, such as exponential [88]-[90], linear [91], and Gaussian [92]-[93] functions, were proposed by researchers for different applications, such as designing electromagnetic and communication systems, microwave devices, and remote sensing. However, there is no particular correlation function designed for microwave imaging systems. The current models, such as the standard time-harmonic signal model used in back-projection and matched filter approaches [96]-[97], are mainly developed for monostatic linear or planar arrays. In this work, a specific correlation

function is derived for the intended multistatic virtual array from the propagation characteristics of electromagnetic waves.

The spatial correlation function between two complex electric fields $\vec{E}$ at $\vec{r_i}$ and $\vec{r_j}$ is defined by [94]

$$\rho(\vec{r_i},\vec{r_j}) = \frac{\langle \vec{E}(\vec{r_i}).\vec{E}^*(\vec{r_j})\rangle}{\langle |\vec{E}|^2\rangle} \tag{5.7}$$

where * denotes complex conjugate, $\langle\ \rangle$ is the ensemble average over all realisations of $\vec{E}$, and $\langle |\vec{E}|^2\rangle = E_0^2$ is the electric field mean power.

To find the spatial correlation function between two electric fields at two different locations, the relation between the electric field and distance is needed. According to the working frequency and size of the biomedical imaged domain, that domain is located within the near- to far-field with respect to the utilised electromagnetic wave source. In addition, the transient waves and strong reflections are removed in the pre-processing stage of the imaging algorithm, explained later in Section III. Therefore, the transmitted waves can be estimated for simplicity and reasonable accuracy by far-field equations. To that end, the angular spectrum of the electric field, which is a composition of different propagating plane waves $\vec{f}$ with zero average value is utilised and can be written in its spatial dependences format as

$$\vec{E}(\vec{r_i}) = \int_{\emptyset} \vec{f}(\emptyset) e^{-i\vec{k}\vec{r}} d\emptyset \tag{5.8}$$

In (5.8) the integral operation is operated over all angles ϕ around the receiving point, while $\vec{r} = \vec{r_i} - \vec{r_r}$ is the distance between transmitter and receiver, and $\vec{k}$ is the complex wavenumber. In this case, the angular spectrum $\vec{f}$ is a random function whose statistical characteristics have to be determined. So, by applying (5.8) in (5.7), we get

$$\rho(\vec{r_i},\vec{r_j}) = \frac{1}{E_0^2}\int_{\emptyset_j}\int_{\emptyset_i}\langle \vec{f}(\overrightarrow{\emptyset_i}).\vec{f}^*(\overrightarrow{\emptyset_j})\rangle e^{-i(\vec{k_i}\vec{r_i}-\vec{k_j}\vec{r_j})} d\emptyset_i d\emptyset_j \tag{5.9}$$

Since the real and imaginary part of the plane wave spectrum are uncorrelated [83], then

$$\left\langle f_{real}(\phi_i)\cdot f^*_{imag}(\phi_j)\right\rangle = 0 \tag{5.10}$$

and

$$\left\langle f_{real}(\phi_i)\cdot f^{*}_{real}(\phi_j)\right\rangle = \left\langle f_{imag}(\phi_i)\cdot f^{*}_{imag}(\phi_j)\right\rangle = \frac{E_0^2}{8\pi^2} \tag{5.11}$$

Thus, the correlation function between two electromagnetic waves is

$$\rho(\vec{r_i},\vec{r_j}) = \frac{1}{4\pi^2}\int_{\emptyset_j}\int_{\emptyset_i} e^{-i\vec{k}|\vec{r_i}-\vec{r_j}|}d\emptyset_i d\emptyset_j = e^{-i\vec{k}|\vec{r_i}-\vec{r_j}|} \tag{5.12}$$

After applying (5.12) in (5.4), the regression coefficient *w* is estimated and then the received signals in the virtual array at any arbitrary configuration can be predicted using (5.6) to set up the required virtual array. The output of the virtual array is the scattering parameter, S_{ij}. Therefore, the imaging method is still in the frequency domain.

Once the virtual array is designed, the imaging algorithm can be used to process the signals at the virtual array to construct the final image.

The key feature of the proposed method is that the employed statistical method can model black-box systems without a priori knowledge about the system's interior. The only required information is the locations of the antennas. By providing the detailed structure of the system (permittivity values at different locations of the heterogeneous head model), the obtained model can perfectly estimate the responses in other locations. However, since it is assumed in this work that the internal structure of the head is unknown, the equivalent homogeneous model is utilised. The equivalent homogeneous model may deliver an estimation error, but this error is significantly reduced by using the average complex permittivity of the head in the correlation function. The results from imaging the head model in Chapter 3 with different values of average permittivity show that 10% variation in the average permittivity does not effectively change the resultant image accuracy and quality. Therefore, using an estimated average permittivity with up to 10% error from the real value is acceptable to still get accurate imaging.

The proposed procedure differs considerably from the back-projection technique, which uses cross-correlation function (convolution) between transmitter and receivers in the time domain to improve the cross-range resolution. In the proposed method, the correlation between any two pairs of transmitter-receiver is used as part of the statistical method to model and predict the signals' behaviour if another antenna is added to the array. By this way, more information is extracted from the data to improve the image quality and accuracy of detection. In addition, unlike the back-projection approach, the location of the reference antennas does not need to be located away from the imaging domain.

5.2 Model Validation

The proposed method is verified using the recorded data from the simulations environment described in Section 3, with different array sizes and then is validated through the experiments on the realistic human head phantom.

5.2.1 Simulations

Using the presented method, the recorded data in the eight-element array (Fig. 3.5 (b)) are utilised to build a twelve-element virtual array uniformly distributed around the head. For this purpose, the frequency-domain received signals by the eight-element array and their corresponding locations are used to find the proper regression coefficients and build the statistical models for each frequency step. Then, the locations of the antennas in the twelve-element array are applied as inputs to the model to generate the required S-parameters.

The obtained S-parameters of the virtual twelve-element and those from the real 12-element array at the exact locations of the virtual elements are illustrated in Fig. 5.2. To enable appraising the quality of the estimation, the estimation errors of different scattering parameters are also illustrated in Fig. 5.3. As it is clear from Fig. 5.3, the proposed model can accurately estimate the S-parameters of a twelve-antenna array from an eight-element array for short and long distances and at different frequencies, though with a slight error compared to the real values. This error is more obvious in S_{61}, S_{71} and S_{18} where the distance between the antenna elements is greater than, for example, the case of S_{21}. The slight error in the estimation of S_{21} comes mainly from the mutual coupling between the neighbouring antennas in the dense array, a factor that is not considered in the calculations.

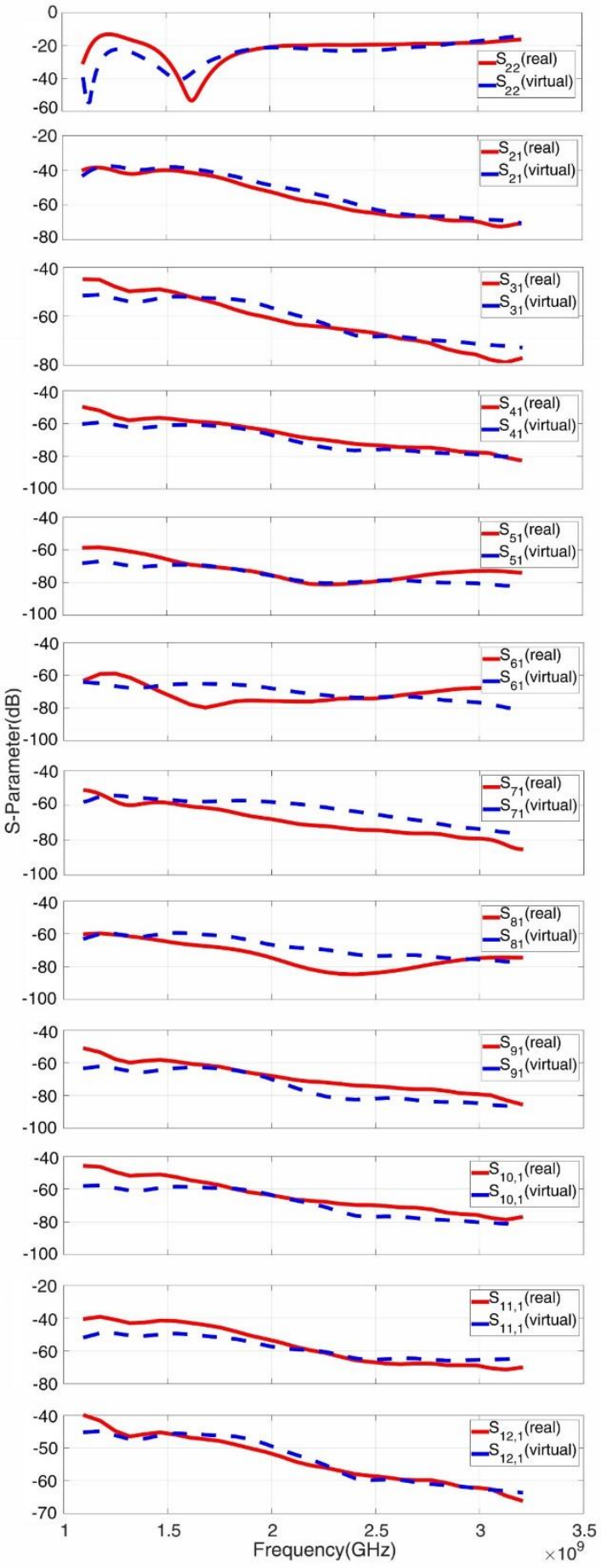

Fig. 5.2 . S-Parameters of real and virtual 12-antenna arrays.

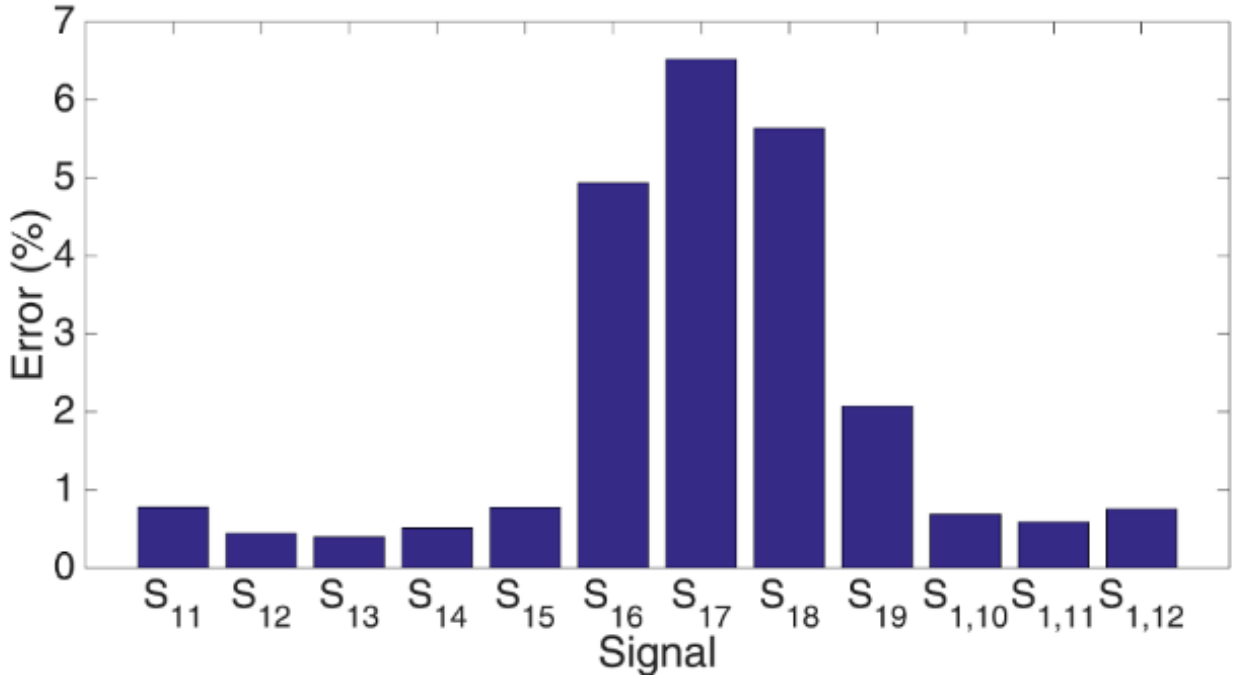

Fig. 5.3. Estimation error for the extended 12-antenna array from 8-element array.

To investigate the efficacy of the designed virtual array and in order to inspect the effect of the produced error on the final image, the proposed frequency-based multistatic microwave imaging algorithm in Section 3 is utilised to process the data and create an image. To that end, the obtained signals from the virtual and real arrays with twelve elements are processed by the imaging algorithm. The signals from the eight real elements are used to generate signals at the locations of the extended virtual elements. Those generated signals are then used for imaging. The resultant images of two unhealthy cases with shallow and deep targets along with the healthy scenario for the 8-element real and its extended 12, 16 and 32 virtual elements are depicted in Fig. 5.4. Locations of the real elements are depicted in Fig. 5.4 (a) with black solid quadrilaterals around the image of the shallow target. The extended virtual elements are positioned uniformly around the head as indicated by the dashed quadrilaterals in Fig. 5.4 (b)-(d). The produced images in Fig. 5.4 are normalised to the maximum intensity of unhealthy scenarios and the exact location of bleeding is indicated by a square.

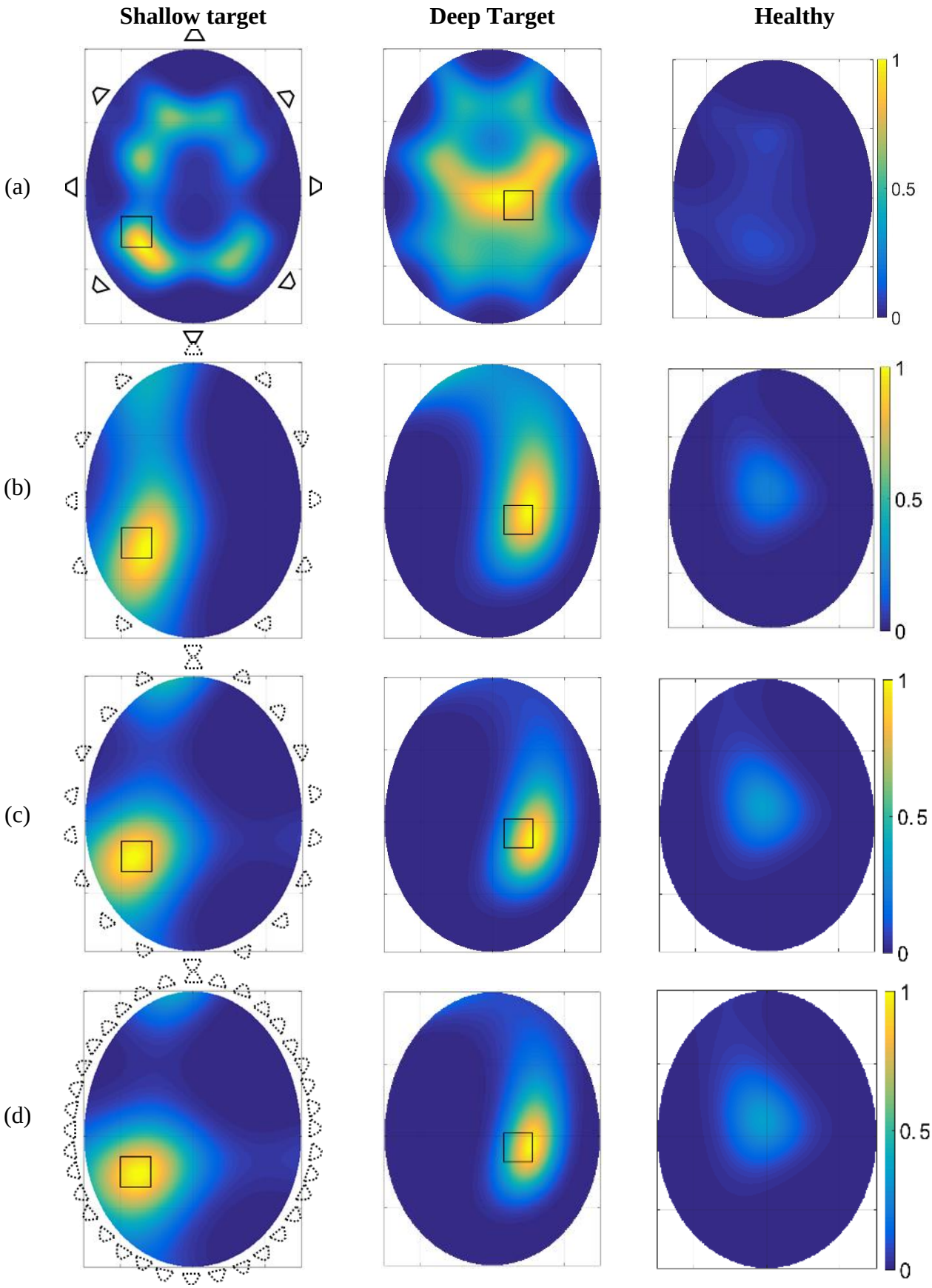

Fig. 5.4. Reconstructed images for shallow target, deep target and healthy scenarios using frequency-based imaging method with (a) real 8-element array, and virtual (b) 12, (c) 16, and (d) 32 elements. Black squares show the exact location of bleeding.

A visual comparison between Fig. 5.4 (a) and (b)-(d) shows that the proposed method effectively improves the image quality and accuracy of the target detection and localisation by mitigating the ghost targets produced by the real 8-element array. It can also be realised from Fig. 5.4 (b)-(d) that increasing the number of virtual antennas using data from the same number of real elements can effectively reduce the estimation error and thus enhance the image quality and accuracy in target localisation. However, there is a limit on the possible improvement. For example, there is no significant improvement in the image quality when increasing the number of virtual elements from 16 to 32. In other words, one of the main findings in our extensive simulations is that using twice the number of real antennas can give the best possible improvement to sufficiently enable the detection of the target with minimum computational efforts. Testing the proposed method in torso imaging system with 12 imaging antennas also shows that using 24 (twice the number of real antennas) can provide the best possible improvement.

To investigate the possibility of differentiating between healthy and unhealthy cases using the proposed method, the variation in the image intensity of those cases (Fig. 5.4) are calculated and plotted in Fig. 5.5. As realised, the image intensity in all of the investigated unhealthy cases is well above the maximum image intensity from the healthy cases; hence, it is fairly reasonable to propose that the unhealthy cases can be detected. Nevertheless, a threshold similar to Fig. 5.5 needs to be established in future tests on human subjects.

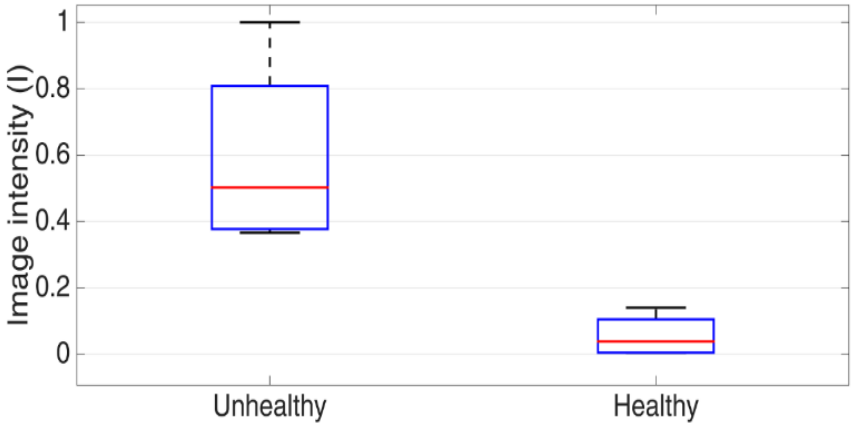

Fig. 5.5. Image intensity variation range for unhealthy and healthy cases.

The reconstructed image with 12-element real array and 12-element virtual array generated from data of the 8-element array are depicted in Fig. 5.6. It can be seen that the virtual antenna array can successfully produce images that are almost similar to the images of a real array of the same number of elements, though with a slight shift in the position of the target. This shift is due to the produced error in the estimation process of the signals at the virtual elements, which can be reduced by increasing the number of virtual antennas as proven with the aforementioned 8-element array case.

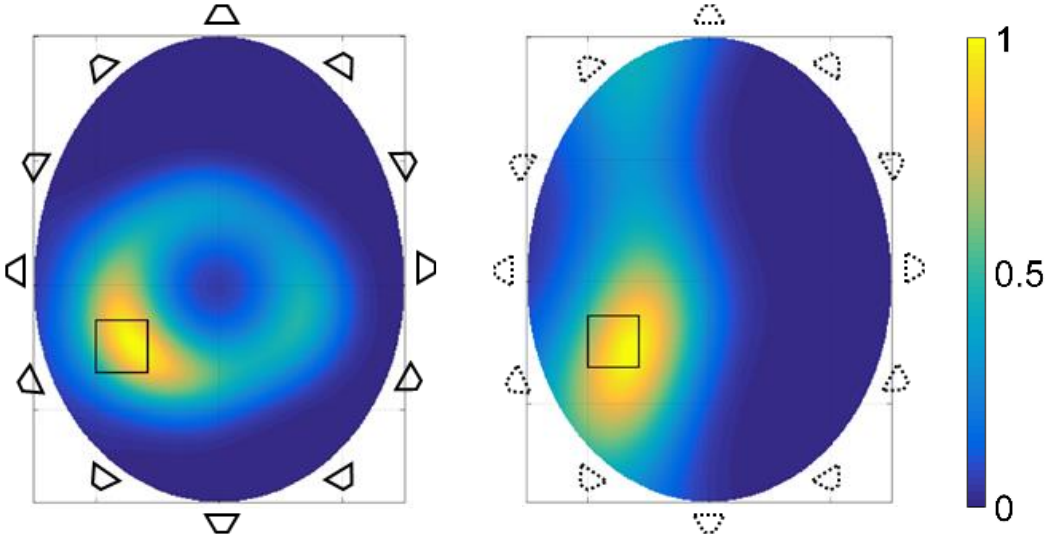

(a) (b)

Fig. 5.6. Reconstructed images using (a) real 12-element array and (b) virtual 12-element array using data from a real 8-element array.

To investigate the quality and accuracy of the reconstructed images, the signal-to-noise ratio (*SNR*) and the detection error (Δ) are used as metrics to quantify the obtained images. Knowing the assumed bleed size and location, the metrics are calculated for the reconstructed images in Fig. 5.4 and Fig. 5.6, and listed in Table 5.1. The higher value of *SNR* and lower value of Δ for the images generated by the virtual array configuration, compared to the values for the real eight-element array, demonstrate that the proposed method provides higher quality images with more accurate detection than the real eight-element array. Those values are very close to the calculated values for the real 12-element array, which proves that the proposed technique can successfully estimate signals in other locations. Interestingly, applying 16- or 32-element virtual array provides more accurate images than the real 12-element array (Fig. 5.4 (b)).

Table 5.1 . Image quality of the simulated results

Array Configuration	SNR (dB)	Δ (mm)	Figure
Real 8-element	2.6	9.8	Fig. 5.4 (a)
Real 12-element	5.5	5.7	Fig. 5.6 (a)
Virtual 12-element	5.2	6.6	Fig. 5.4 (b)/ Fig. 5.6 (b)
Virtual 16-element	5.6	2.9	Fig. 5.4 (c)
Virtual 32-element	5.7	2.7	Fig. 5.4 (d)

In order to investigate the ability of the proposed method when smaller number of real antenna elements are used, images with six and four-element arrays and their virtual extensions to 8, 12, 16 and 32 elements are constructed and depicted in Fig. 5.7 and Fig. 5.8, respectively. It can be seen from Fig. 5.7 (a) and Fig. 5.8 (a) that the obtained data from the six and four-element arrays are not enough to enable the detection of the target. Applying the virtual array concept on the data from four and six elements improves the image quality (Fig. 5.7 (b)-(c) and Fig. 5.8 (b)-(c)). However, due to the lack of enough information when using such a small number of antennas, the extended virtual array cannot localise the target in its actual position even when generating data via a dense 16-element virtual array.

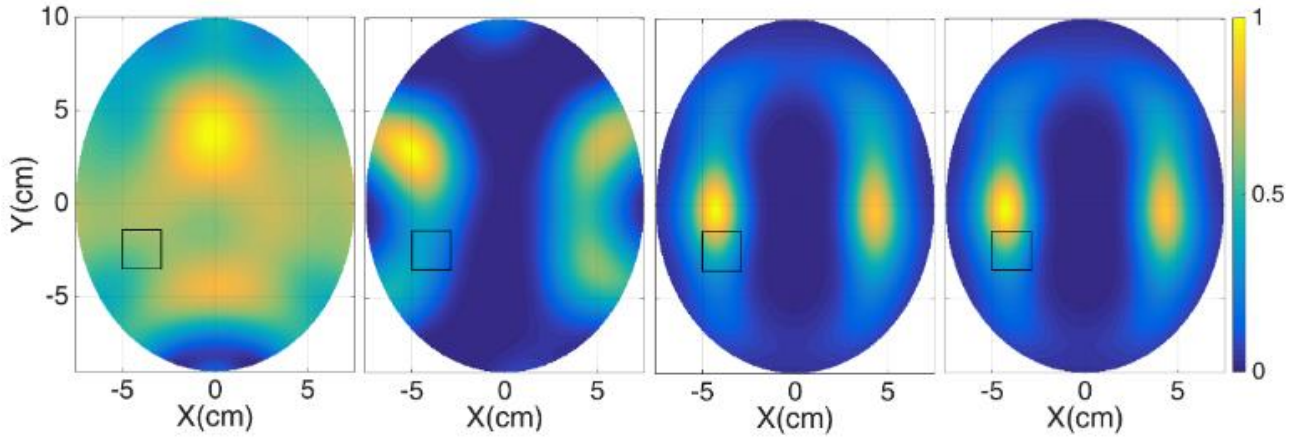

(a) (b) (c) (d)

Fig. 5.7. Reconstructed images from (a) real six-element array with virtual (b) 8, (c) 12, and (d) 16-element arrays.

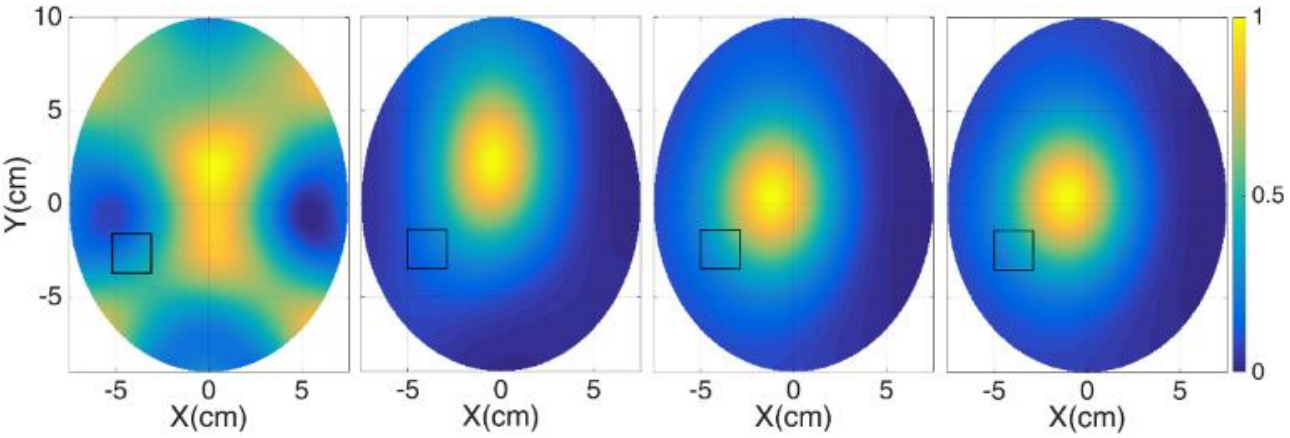

(a) (b) (c) (d)

Fig. 5.8. Reconstructed images from (a) real four-element array with virtual (b) 8, (c) 12, and (d) 16-element arrays.

From the previous results, it is clear that the virtual array concept does not work well when the data comes from a very small number of real antennas. Therefore, the logical question here is on the minimum number of real antennas required for the proposed virtual array concept to work. To that end, the information correlation coefficient (*ICC*) [98], which is widely used in information theory to quantify the amount of information similarity between two set of data, is utilised. The *ICC* of every two neighbouring antennas in an array is calculated using

$$ICC(S_i, S_{i+1}) = \frac{\left|\sum_{k=1}^{N_f} \left\langle S_i . S_{i+1}^{*} \right\rangle\right|}{\sqrt{\sum_{k=1}^{N_f} \left\langle |S_i|^2 \right\rangle \left\langle |S_{i+1}|^2 \right\rangle}}, \quad S_{N_a+1} = S_1 \tag{5.13}$$

where $S_i = \{s_{i,1}, s_{i,2}, \ldots, s_{i,Na}\}$ is the set of received signals at ith receiver from all the other antennas. $ICC = 1$ means that the two neighbouring antennas receive exactly the same signals. *ICC* approaches zero when the signals received at two neighbouring antennas have no information in common. Connecting those two limits to the proposed techniques, high values of *ICC* means there is no benefit from extending the real array using the virtual concept as the real array is dense enough to recover the whole data about the imaged domain. On the other hand, $ICC = 0$ means critical information is lost such as when using a very small number of antennas, and thus the virtual concept will not be able to recover that data. There is a range between those two extremes where the virtual concept is effective. To find that range for the problem under investigation, the minimum and maximum values of *ICC* for different real arrays are calculated and listed in Table II. Based on the generated images and *ICC* values in Table 5.2, it is possible to suggest that an *ICC* within the range 0.2 to 0.5 is a reasonable range for the virtual concept to be effective for the subjects within the size of the head model.

Table 5.2 . Mutual information between neighbouring antenna elements

Number of antennas	Min (*ICC*)	Max (*ICC*)
4	0.014	0.081
6	0.045	0.125
8	0.226	0.278
12	0.232	0.345
16	0.273	0.468

The minimum and maximum number of antennas for the head imaging calculated by the degrees of freedom (DOF) theory [75]-[76] confirms the proposed values. According to DOF, the imaging domain's perimeter should be sampled at a minimum rate equal to one-half of the wavelength in air to be able to detect the target:

$$\Delta\phi \leq \lambda_{\min}/(2a) \tag{5.14}$$

In this case, the number of DOF of the head imaging system and thus the maximum number of antennas required to collect the available information at the highest frequency and provide the best result is 16 as confirmed in Fig. 5.4. This is the reason why only marginal improvements are observed when using the 32 antennas virtual array (Fig. 5.4 (d)). However, the target in this problem can be roughly enclosed in a square sub-domain centered on the origin of side 10 cm (radius of the imaging domain), corresponding to a minimum number of DOF of 8. Therefore, at least 8 antennas are required for the proposed virtual array concept to work (Fig. 5.4 (a)), whereas four and six antennas (Fig. 5.7 and Fig. 5.8) are not sufficient to build a virtual array capable to successfully image the target.

5.2.2 Experiments

To validate the proposed method, it is applied to the experimental data collected from the integrated microwave head imaging system as explained in Section 3. By using the recorded data from the real eight-element array, a 16-element (twice the number of the real antennas) virtual array with eight elements in halfway between any two real elements is generated. Then, the imaging algorithm is applied to those virtual data to reconstruct the final image. The final images for real eight-element array and 16-element virtual array along with their calculated metrics are depicted in Fig. 12. According to the obtained images, the proposed method can effectively improve the detection accuracy and image quality by localising the target in its exact location and mitigating the ghost targets. A comparison between the metrics indicate that the resultant images from the proposed virtual array deliver higher values of *SNR* and lower values of Δ for both of the investigated experimental scenarios. These metrics confirm the efficacy of the proposed method in improving detection accuracy and image quality in the investigated multistatic microwave head imaging.

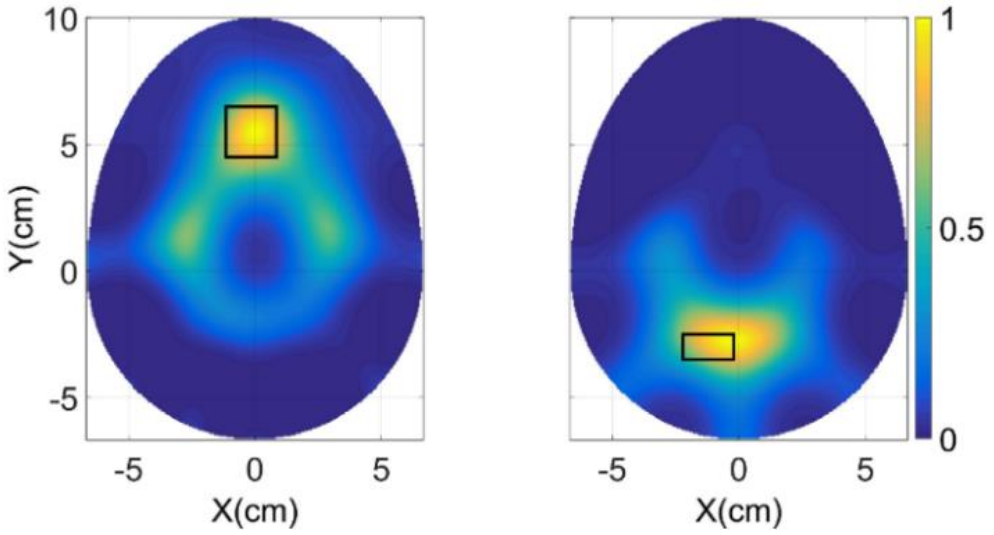

SNR = 6.2 dB, Δ=3.6 mm SNR = 7.2 dB, Δ = 13 mm

(a)

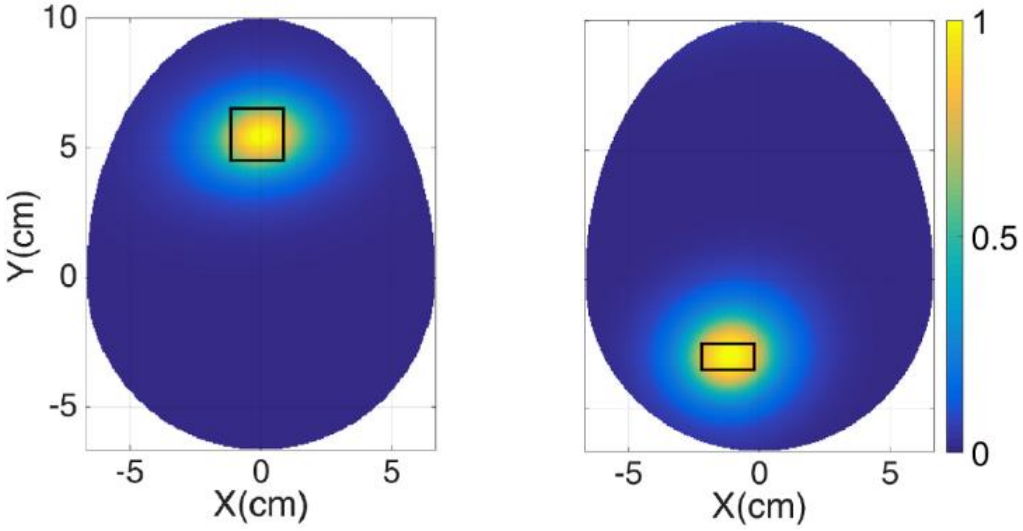

SNR = 6.8 dB, Δ = 1.5 mm SNR = 7.7 dB, Δ = 2 mm

(b)

Fig. 5.9. Reconstructed images from experimental data, using (a) real eight-element array, and (b) virtual 16-element array. Left images are related to the 2 × 2 × 2 cm3 and right images are related to the 2 × 1 × 1 cm3 bleeding target. Black rectangles show exact location of target.

5.3 Comparison

To compare the proposed method with existing correlation-based methods, the multistatic back-projection technique [96]-[97] is used to process the same simulated datasets. The back-projection technique uses cross-correlation function (convolution) between transmitter and receivers in the time domain to improve the cross-range resolution. Fig. 5.10 shows the obtained images using the aforementioned methods to process the simulated data. It is obvious from Fig. 5.10 (b) that the back-projection method cannot clearly detect the target in both of the scenarios. This method

produces false targets due to small distances between the transmitters and receivers. In comparison, the proposed method can accurately detect the target in the same simulated environment for shallow and deep targets (Fig. 5.10 (a)). The images' metrics for the back-projection method are calculated and compared with the proposed method counterparts as shown in Table III. The larger value of *SNR* and smaller value of localisation error Δ for the proposed method than the values in the back-projection method demonstrate superiority of the proposed method.

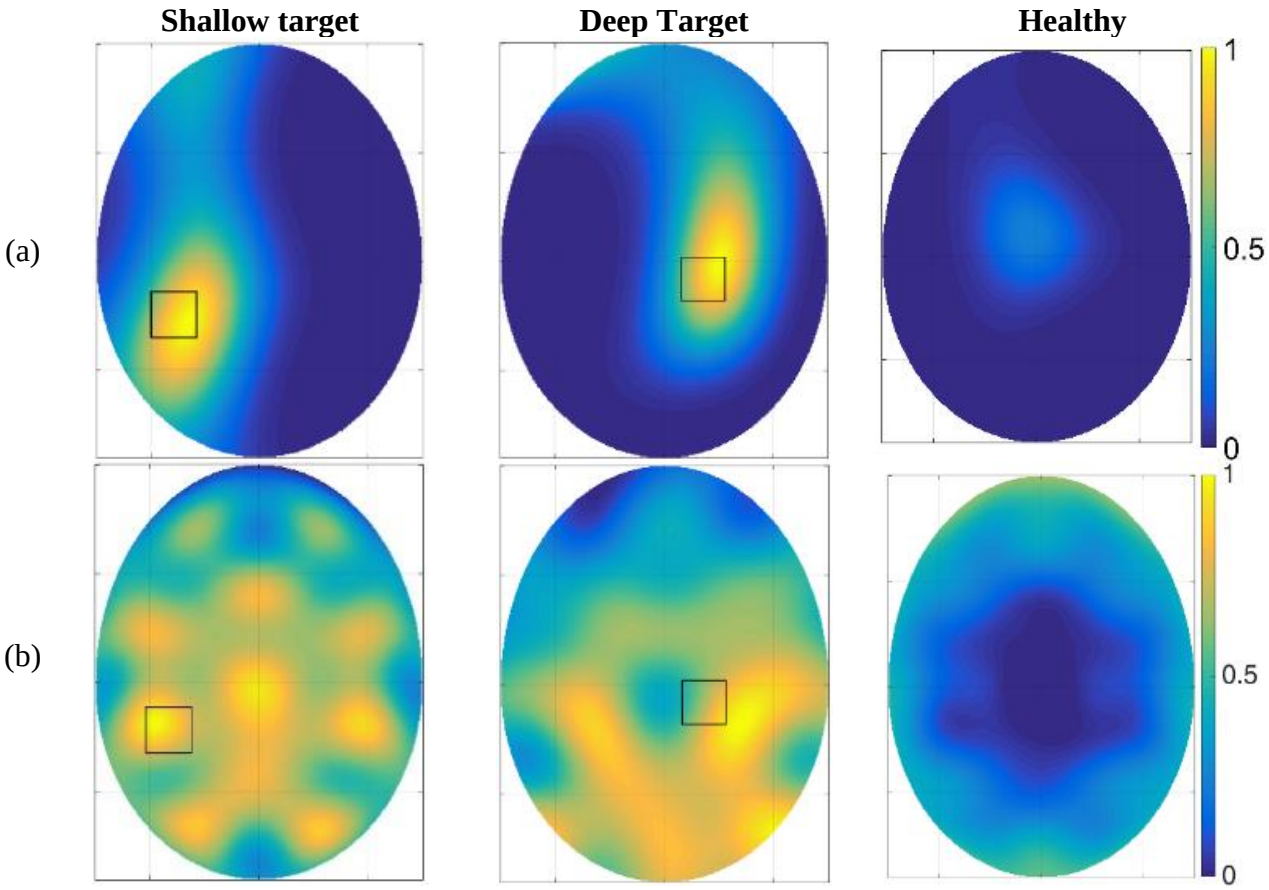

Fig. 5.10. Reconstructed images for shallow target, deep target and healthy scenarios using (a) frequency-based imaging method with virtual 12-element array extracting from 8 real antenna array and (b) multistatic back-projection technique with real 8-element array.

Table 5.3 . Comparison of image quality

Array Configuration	*SNR* (dB)	Δ (mm)	Figure
Proposed virtual 12-element	5.2	6.6	Fig. 5.10 (a)
Back-projection	2.7	10.4	Fig. 5.10 (b)

5.4 Summary

A virtual array concept for microwave biomedical imaging has been introduced. It utilizes a spatial correlation function to virtually increase the number of antennas and consequently the number of available signals for processing and image formation. While increasing the number of antennas improves image quality, multistatic biomedical imaging allows the use of only limited number of real antenna elements due to the available space, antenna size, mutual coupling and system complexity. The developed technique is effective when the number of real antenna elements is neither too small nor too large. To scientifically define those two limits, the information correlation coefficient, which measures the similarity in the signals received by any two neighbouring antennas, is introduced. It is shown that the virtual array technique is efficient when the values of that coefficient are within the range 0.2 to 0.5. With this range, a virtual array that has twice the real antenna elements, which meet the minimum limit of degree of freedom of the problem, is needed to generate the best possible image without significantly increasing the computational resources required. The proposed method has been successfully verified via simulations and experiments in a head imaging system. It has also been shown that the proposed virtual method is more accurate with better clutter rejection capability than existing back-projection methods.

6 Permittivity Estimation as a Priori for Microwave Medical Imaging

As mentioned before, all of the microwave imaging techniques, such as delay-and-sum [35], space-time beamforming [40], adaptive beamforming [43], and the proposed frequency domain algorithms need a priori information on the wave's propagation speed in the imaging domain. Thus, the effective dielectric constant of the domain is typically assumed in the homogeneous propagation models employed by those algorithms. However, due to the multiple reflection and refraction of the electromagnetic wave in a dispersive and heterogeneous environment such as the human body, the wave passes through different tissues and follows different paths depending on the transmitter-receiver location with respect to the imaged object. Therefore, each transmitting-receiving antenna pair "sees" different effective permittivity, which is the average permittivity of tissues and space through which the electromagnetic wave propagates for a specific transmitter-receiver scenario. That effective permittivity thus depends on the location of the antennas with respect to the imaging domain, in addition to properties of the imaged object and its location with respect to those antennas. Therefore, a method to accurately predict the location-specific dielectric properties of the imaged domain is required for successful radar-based imaging algorithms. In this chapter, a technique to determine the effective complex permittivity seen by each imaging antenna across the used frequency band of a multistatic imaging domain is presented.

6.1 Permittivity Estimation Techniques: Literature Review

Different methods to estimate the permittivity of the imaging domain were proposed [99]-[101]. In those methods, the time delay between two sets of measurements (with and without the imaging subject or with its metallic equivalent) are compared to determine the average permittivity of the subject. In [102], Multiple Signal Classification (MUSIC) technique was used to calculate the Time-of-Flight (ToF) of the signals through the imaged domain to estimate the average dielectric permittivity of the imaged object. Those techniques gave promising results for low-loss, frequency-independent and homogeneous objects. However, the heterogeneous objects with frequency dispersive properties like human tissues, can lead to inaccurate ToF estimation, which subsequently result in inaccurate images. With the heterogeneous structure of human organs, which creates multiple signal paths and possible surface waves, the exact value and meaning of ToF are quite ambiguous.

In [103], the dielectric constant of the imaged subject is modelled as a function of antenna's position and imaged location within the imaging domain of a monostatic imaging system. The used dielectric model is specific to the imaged object and is thus highly sensitive to variations in the size and shape of that object. In addition, the location of the imaged object with respect to the antennas should be known and agreed with a pre-defined value for an accurate estimation. In another approach, the most likely effective permittivity of the imaging domain is estimated by optimising the image quality [25], [104]. Those works showed interesting results for monostatic head and breast imaging; however, they are time consuming if used in multistatic configurations with large imaging domains. In addition, they may converge on local maxima (ghost targets) in highly heterogeneous environments, causing inaccurate detection as they rely on finding one effective permittivity for the whole domain. In [105]-[106], the relative permittivity of biological tissues is expressed as a weighted sum of scattering parameters to determine the electrical properties of deep internal organs for monitoring purposes. However, that method needs the average permittivity and imaged object borders as a priori information to reduce the training matrix size. In addition, the measurements are performed in a low frequency step for a two-layer structure, which is not applicable for ultra-wideband imaging techniques that deal with heterogeneous frequency dispersive tissues.

A method to estimate the complex permittivity of the imaging domain using a statistical modelling technique is presented in the following sections. It has the capability to accurately predict the effective complex permittivity seen by any imaging antennas across the whole used band. The proposed method does not require any predefined distance between the antennas and the imaged

object, nor does it need the imaged object to be cantered within the imaging domain. In addition, the method does not need to know boundaries of the imaged object. Those three parameters are quite important in medical applications, where the distance between the antennas and the imaged object, which may have any shape or size, cannot be fully controlled or known. The performance of the proposed method is successfully verified by realistic simulations and validated by experiments on the human torso phantom with the aim to detect early lung cancer.

6.2 Permittivity Estimation from the View Point of Each Antenna

Assume that an imaging domain is surrounded by N_a antennas operating in multistatic mode as shown in Fig. 6.1. The effective permittivity of the imaging domain seen by any antenna depends on properties, size, and shape of the imaged object located in the domain. For a heterogeneous object with frequency dispersive properties, the effective permittivity seen by an antenna depends also on the location of that antenna with respect to the object and the used frequency. Thus, the assumption of one effective permittivity, or even the prediction of one effective value when using radar beamforming processing techniques does not really enable accurate imaging. Hence, a method that can predict the effective permittivity seen by any antenna is necessary for accurate imaging.

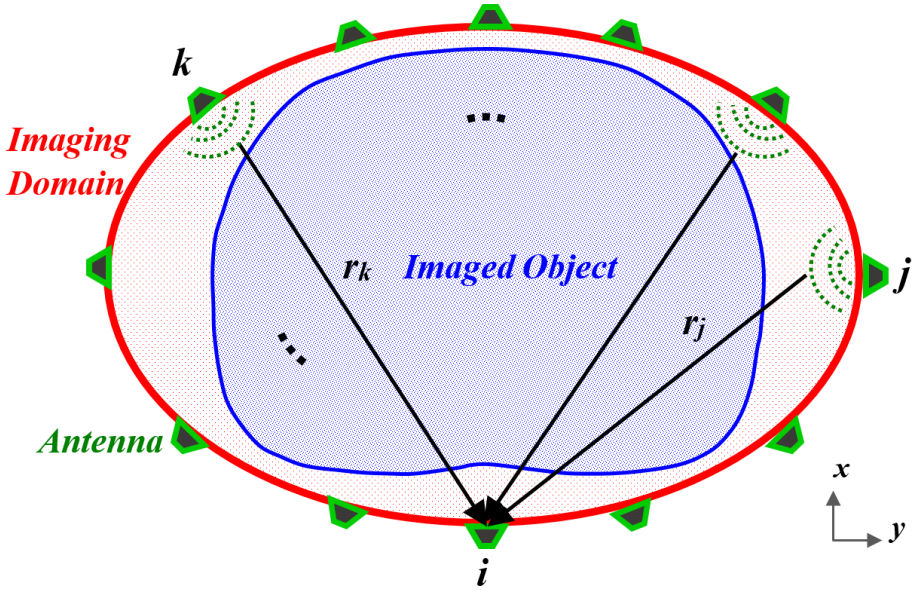

Fig. 6.1. The used imaging domain.

The effective permittivity can be expressed as a function of the scattering parameters. So, if a set of S-parameters are calculated for a specific imaging domain (i.e. specific antennas and array structure) with known properties, these parameters can be used to train the system to predict the effective complex permittivity when imaging an unknown object. In the work [105], such a function was solved using the ordinary least squares linear regression methods in a bistatic configuration. However, due to the large number of variables (S-parameters) in the adopted multistatic

configuration, such a function leads to ill-posed problems, where more than one weighting factor satisfy the linear equation, leading to over or underdetermined equations.

To address this issue, additional information must be introduced to the ill-posed problem to prevent over- or under-fitting. To that end, the problem is regularised by the spatial regionalisation of the scattering parameters; thus, the variogram [107], which describes the degree of spatial dependence of signals, is calculated for each receiver *i*:

$$\gamma_i(h) = \frac{1}{2|N(h)|}\sum_{(j,k)\in N(h)}\left|S_{ij} - S_{ik}\right|^2 \tag{6.1}$$

where h is the distance between the jth and kth transmitting antenna locations, S_{ij} is the received signal at ith antenna transmitted from jth antenna using N_f frequency samples, and $N(h)$ denotes the set of pairs of observations ij and ik such that $|r_{ij} - r_{ik}| = h$ and $|N(h)|$ is the number of pairs in the set. Low values of h represent neighbouring antennas, which receive highly correlated signals and thus their corresponding γ is low, whereas antennas that are distant from each other (high values of h) deliver high values of γ. From the physical point of view, electromagnetic waves that pass through similar tissues with similar permittivity values deliver lower variogram values (higher correlation), while the waves that pass through different tissues than other transmitting waves deliver higher variogram values (lower correlation). By using (6.1), each receiver in the multistatic configuration is presented by a function $\gamma(h)$. Therefore, $0.5\times N_a\times(N_a+1)$ independent variables/signals are reduced to N_a regularised functions that incorporate the spatial features of relevant signals.

To link $\gamma(h)$ with the dielectric properties of the imaging domain, the effective permittivity from the view point of ith receiver ε_i is modelled as

$$\varepsilon_i = \mathbf{f}(s)\mathbf{w} + z(s) \tag{6.2}$$

where $s=\{\gamma, h\}$ is the function's input in which γ is calculated using (6.1), $\mathbf{f}(s) = [1, \gamma, h, \gamma^2, \gamma h, h\gamma, h^2]$ is a vector of quadratic regression function, and $\mathbf{w}$ is the 7×1 vector of regression coefficients to be calculated for a minimised error $z(s)$. There are N_h functions of ε_i for h values extending from 0 to the length of the maximum axis of the elliptical antenna array. Those quadratic functions relate discrete values of γ to h and to ε. To obtain the best-unbiased estimation of $\mathbf{w}$, it is necessary to train the model using training samples, which are generated using the calculated S-parameters of the imaging domain when filled with uniform media that have certain assumed permittivity values (sample mediums). In that regard, the imaging domain (such as the ellipse in Fig. 6.1) is assumed

to have N_ε different permittivity values $\varepsilon_{n\,(n=1\text{ to }N_\varepsilon)}$ and the corresponding multistatic S-parameters are calculated at each assumption. The calculated S-parameters are then used in (6.1) to obtain $\gamma(h)$ and thus the corresponding training functions $s_n=\{\gamma_n, h_n\}_{(n=1\text{ to }N\varepsilon)}$ and $\mathbf{f}(s_n)$. Assuming N_ε different training samples with assumed permittivity values $\varepsilon_{n\,(n=1\text{ to }N\varepsilon)}$, (6.2) can be written in a matrix form as

$$\boldsymbol{\varepsilon}_i = \mathbf{F}\mathbf{w} + \mathbf{z} \tag{6.3}$$

where $\boldsymbol{\varepsilon}_i = [\varepsilon_1,\ldots,\varepsilon_M]^T$ is the vector of permittivity with the dimension of M $(=N_\varepsilon \times N_h) \times 1$, $\mathbf{F} = [\mathbf{f}(s_1),\ldots,\mathbf{f}(s_M)]^T$ is the $M \times 7$ regression function matrix and $\mathbf{z} = [z(s_1),\ldots,z(s_M)]^T$ is the $M \times 1$ error vector. The matrix of coefficients estimator $\hat{\mathbf{w}}$ (the notation $\hat{}$ represents the estimated coefficient) can be determined subject to the minimisation of the total sum of squares (TSS) of the error, $\mathbf{z}$

$$TSS = \sum_{n=1}^{M} |z(s_n)|^2 = (\boldsymbol{\varepsilon} - \mathbf{F}\mathbf{w})^{\boldsymbol{T}}(\boldsymbol{\varepsilon} - \mathbf{F}\mathbf{w}) \tag{6.4}$$

The generalised least squares solution of $\mathbf{w}$ is then [108]

$$\hat{\mathbf{w}} = (\mathbf{F}^T\mathbf{C}^{-1}\mathbf{F})^{-1}\mathbf{F}^T\mathbf{C}^{-1}\boldsymbol{\varepsilon} \tag{6.5}$$

In this equation, $\mathbf{C} = [c_{ij}]$ is an $M \times M$ stochastic-process correlation matrix with $c_{ij} = \rho(s_i, s_j)$, $i,j=1,...,M$, where ρ is the correlation function between the permittivity values at samples $s_i=\{\gamma_i, h_i\}$, $s_j=\{\gamma_j, h_j\}$. After testing different correlation functions such as linear [91], Gaussian [92] and exponential functions [109], the latter is selected as it gives the best fit to the data.

After finding $\hat{\mathbf{w}}$ for the designed imaging domain (antenna array and its structure), the training step finishes, and the system is ready to be used to image an unknown object of any shape and size as long as it fits within that domain. In this case the permittivity value $\hat{\varepsilon}_i$ for the measured S-parameters in the presence of an unknown imaged object with $s=\{\gamma, h\}$ is approximated by [87]

$$\hat{\varepsilon}_i(s) = \mathbf{f}(s)\hat{\mathbf{w}} + \mathbf{c}(s)^T\mathbf{C}^{-1}(\boldsymbol{\varepsilon} - \mathbf{F}\hat{\mathbf{w}}) \tag{6.6}$$

where $\mathbf{c}(s)$ is the correlation matrix between the input s from the unknown object and the training samples. Finally, the observed effective permittivity by the ith antenna is calculated by averaging the permittivity values over all values of h:

$$\hat{\varepsilon}_i^{\,effective} = \frac{1}{|N_h|}\sum_{j=1}^{N_h} \hat{\varepsilon}_i(s_j) \tag{6.7}$$

In summary, the proposed method can be represented by the flowchart shown in Fig. 6.2 and explained by the following steps:

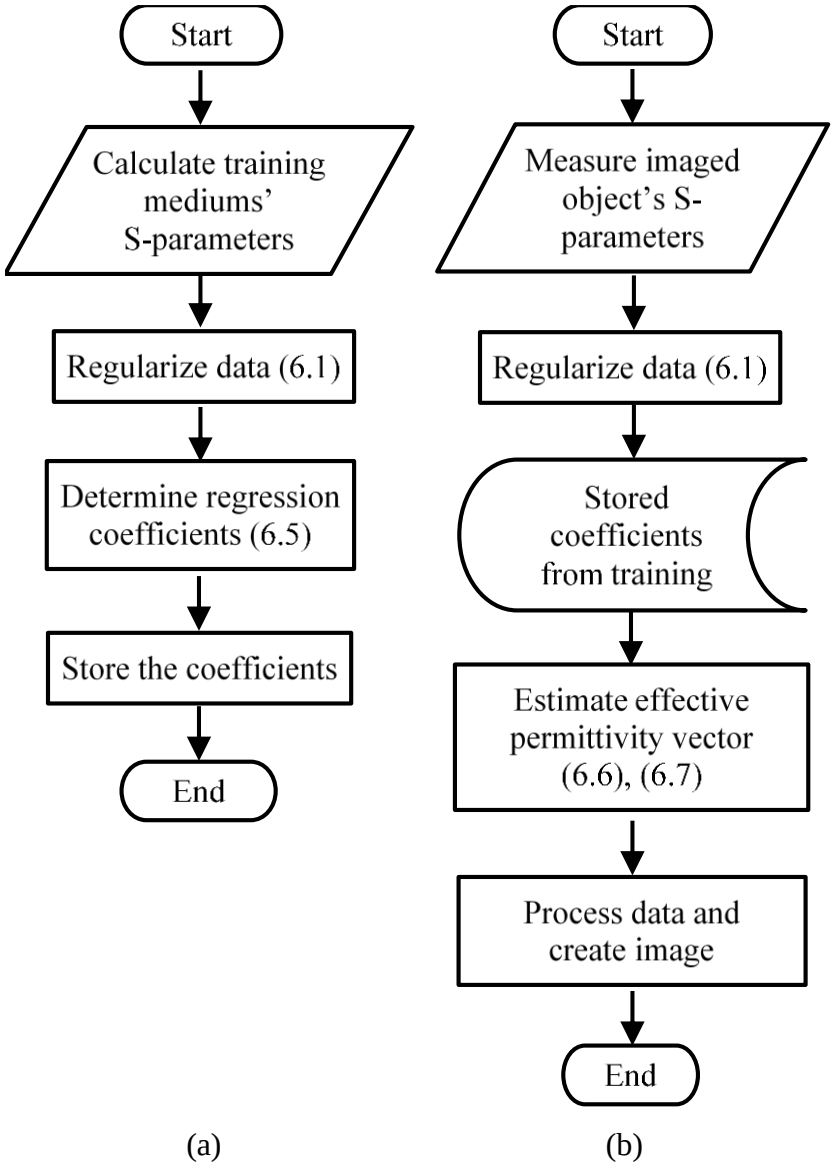

Fig. 6.2. Flowchart of the proposed method, (a) training and (b) imaging.

a) Training;

1. Calculate the multistatic frequency domain S-parameters for certain range of training mediums,

2. Regularise the S-parameters using (6.1),

3. Determine the vector of the coefficients estimator $\hat{\mathbf{w}}$, using (6.5).

b) Imaging;

1. Insert the object to be imaged in the imaging domain and collect the multistatic frequency domain S-parameters with the existence of the unknown imaged object,

2. Regularise the measured S-parameters using (6.1),

3. Estimate the effective complex permittivity vector using (6.6) and (6.7),

4. Construct an image using the estimated permittivity values and proper imaging algorithm.

6.3 Verification

To verify the proposed method in medical applications, a realistic simulation environment for human torso imaging is established in ANSYS HFSS. An elliptical shaped antenna array is utilised to simulate a realistic scenario in which the distance between the antennas and the imaged object, such as the human torso, is not uniform (Fig. 6.3). The used antenna array consists of compact unidirectional ultra-wideband antennas [110]. A photo of the used antenna and its performance are depicted in Fig. 6.4. The utilised antenna has the dimensions of 100 × 120 × 0.8 mm^3 and operates across the band 0.65-1.75 GHz with more than 10 dB return loss in free space and more than 20 dB mutual coupling between any two neighbouring antennas of the array. In the training and imaging steps, a signal covering the frequency band 0.65-1.75 GHz at 10 MHz intervals is sequentially transmitted by one antenna while all of the antennas receive the scattered signals, which are then recorded for further processing.

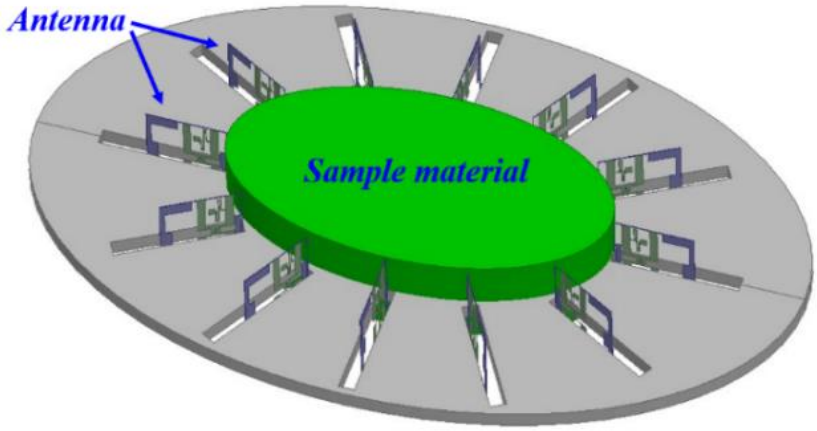

Fig. 6.3. Training setup.

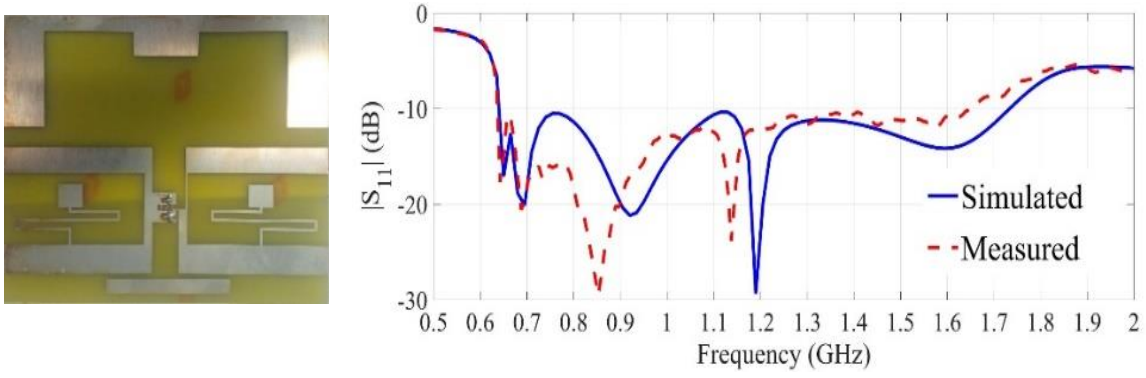

(a) (b)

Fig. 6.4. (a) The utilised antenna [25], and (b) its reflection coefficient.

To investigate the effect of the number of antennas on the estimation accuracy, the estimation error for different number of antennas is calculated and plotted in Fig. 6.5. The estimation error is the percentage of difference between the actual and estimated dielectric properties of a known test material that has different dielectric properties than the sample materials. It can be seen from Fig. 6.5 that the estimation error decreases with the increase in the number of imaging antennas. However, there is no significant improvement in the estimation error when increasing the number of antennas to more than 12. This issue can be explained by the fact that increasing the number of antennas significantly means that neighbouring antennas get closer to each other and they start to "see" the same effective permittivity from the imaged domain. Assuming 5% as an acceptable estimation error for the permittivity and conductivity [101], [105], at least 12 antennas are required to estimate those values in the considered torso imaging domain.

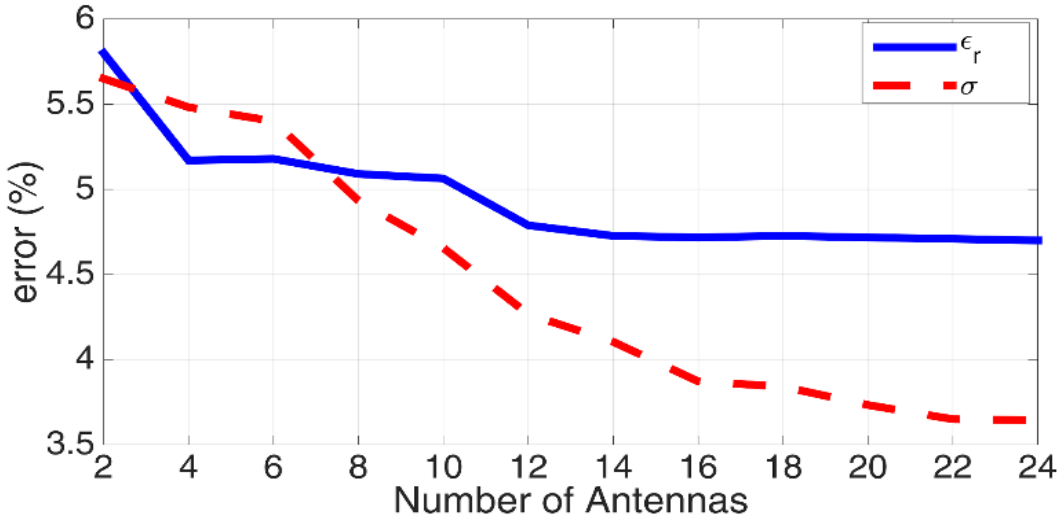

Fig. 6.5. Estimation error with number of antennas.

In the training step, no object is inserted in the imaging domain. Instead, a uniform training medium with the height equal or more than the height of the antennas fills the whole imaging domain, while the dielectric properties of air is chosen for the medium around and behind the antennas. The number of training media or samples (M) needed to train the method affects the estimation accuracy. Essentially, larger number of training samples means more accurate estimation of the permittivity, but at the expense of longer time for data gathering and model training. To determine a suitable number of samples, a design space including all possible combinations of permittivity and conductivity values is considered. Since the aim of this work is torso imaging, the design space is sampled using the ranges of ε_r = [1, 63] and σ = [0, 1.9] to cover all the permittivity values of human torso tissues. The time needed for recording the required data in simulations and training using three different permittivity and conductivity sampling intervals ($\Delta\varepsilon_r$, $\Delta\sigma$) is provided in Table 6.1. The computations are performed by a 3.4 GHz and 16 GB RAM personal computer. The time

for data gathering is calculated by multiplying the number of simulations (M) in the required time for one simulation run (≈ 4 hours). It is clear from Table 6.1 that 5040 hours (7 months) is needed to achieve a perfectly accurate model. It is also clear that the required time to train the model dramatically increases with the increase in the number of samples.

Table 6.1. Computation time for different number of samples

$[\Delta\varepsilon_r , \Delta\sigma]$	**[5 , 0.5]**	**[2 , 0.2]**	**[1 , 0.1]**
Number of samples (M)	65	315	1260
Time for gathering data (h)	260	1260	5040
Time for training (s)	164	3116	263520

To find a suitable compromise between the high gathering and training time needed with large number of samples and estimation accuracy, the estimation errors for different sampling intervals are calculated based on Monte Carlo sensitivity analysis [111]. In that regard, one fixed value for each parameter (e.g. conductivity) is randomly selected within its range, while the other parameter (e.g. permittivity) is sampled at different intervals. The relevant S-parameters are then calculated when the imaging domain is filled with the sampled permittivity values. The obtained S-parameters are used in (6.1) to regularise the data, and the estimation error $z(s)$ is calculated using (6.4), where $\mathbf{w}$ is replaced by $\widehat{\mathbf{w}}$. The estimation errors for different sampling intervals are plotted in Fig. 6.6 (a) and (b), respectively. It is clear from Fig. 6.6 that the error between the estimated and actual values of permittivity and conductivity increases by increasing the sampling intervals. According to Fig. 6.6, the maximum sampling intervals for the permittivity and conductivity are $\Delta\varepsilon_r = 2$ and $\Delta\sigma = 0.2$, respectively, to achieve less than 5% estimation error. Therefore, 315 training samples are required to fill the design space with $\Delta\varepsilon_r = 2$ and $\Delta\sigma = 0.2$ sampling intervals. Fig. 6.7 (a) shows distribution of the complex permittivity values of the selected samples (blue dots) along with the range of values for the dielectric parameters of different human torso tissues (coloured boxes). Variations of those parameters for some of the torso tissues with frequency are also shown in Fig. 6.7 (b).

The calculated S-parameters for all of the training media are used to model the dielectric properties of the imaging domain using (6.1) – (6.5). Once the model is created, it can be used to estimate the dielectric properties of any imaged object using (6.7). While this model is exclusive to the trained imaging domain i.e. the antenna array and size of the imaging domain, it is valid for imaging any object located within that domain.

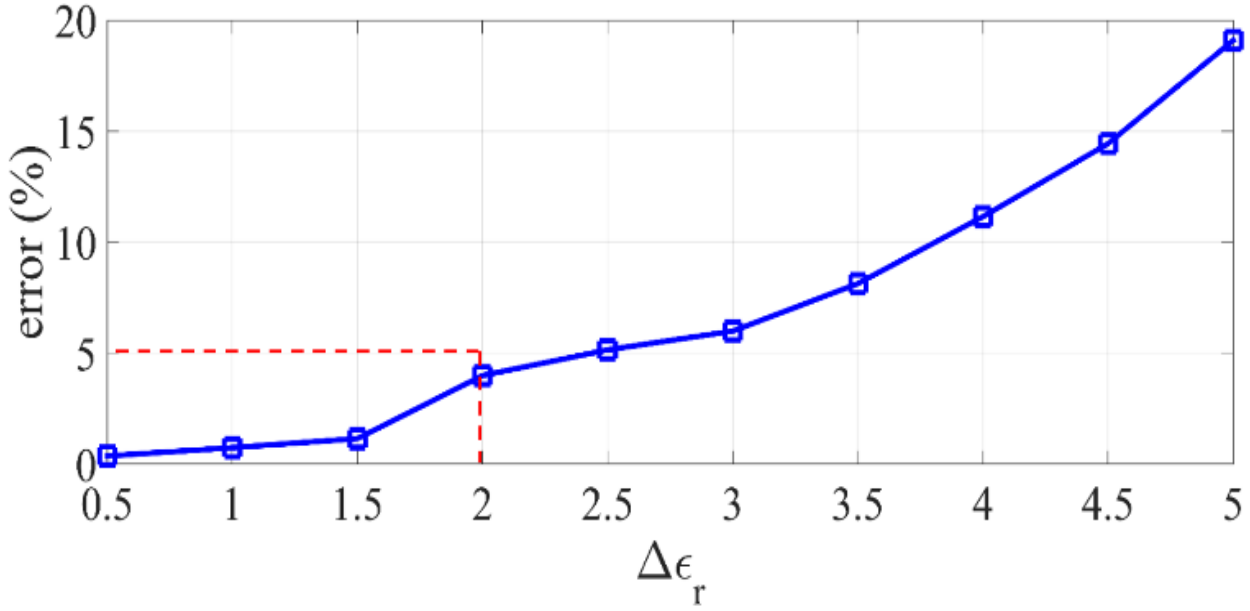

(a)

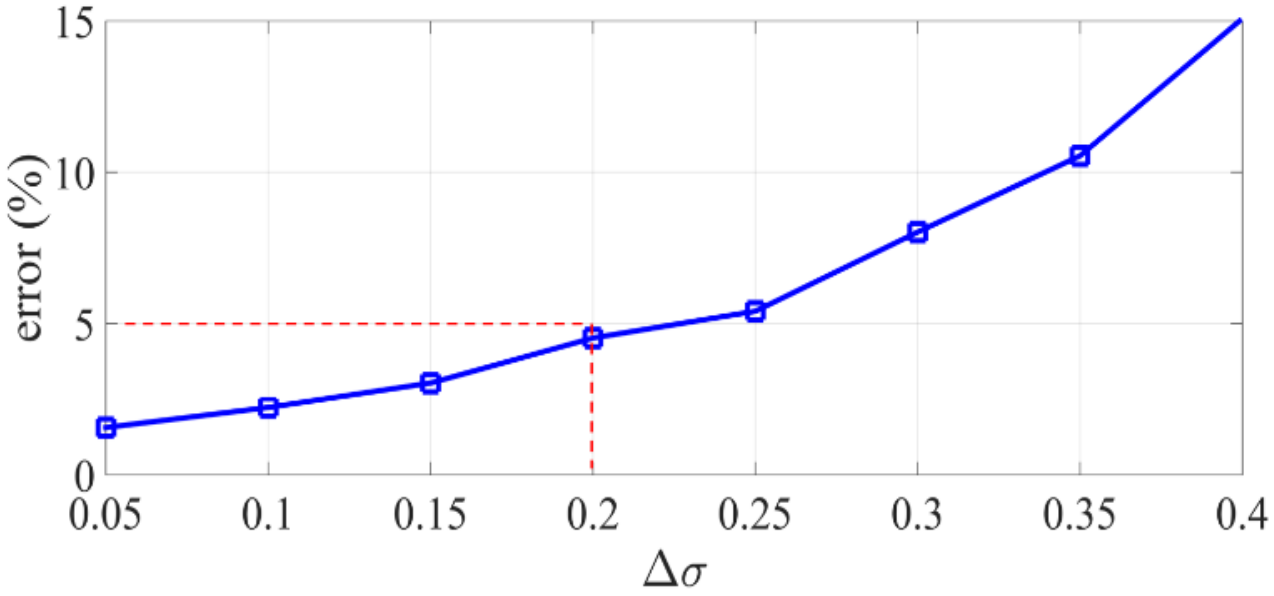

(b)

Fig. 6.6. Estimation error against sampling size, for (a) relative permittivity and (b) conductivity.

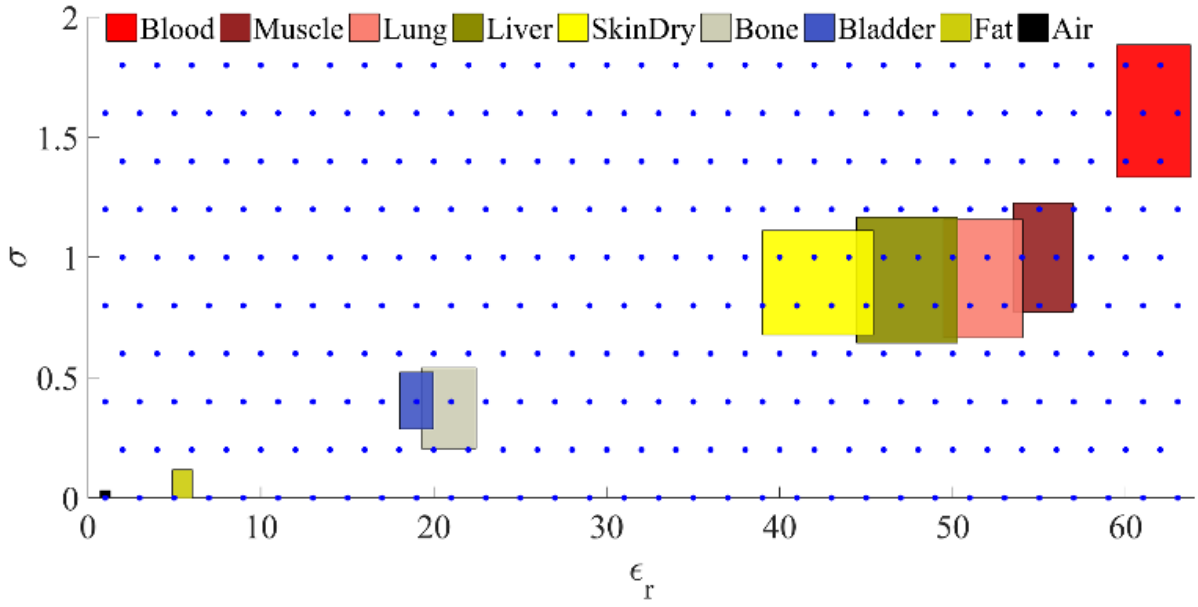

(a)

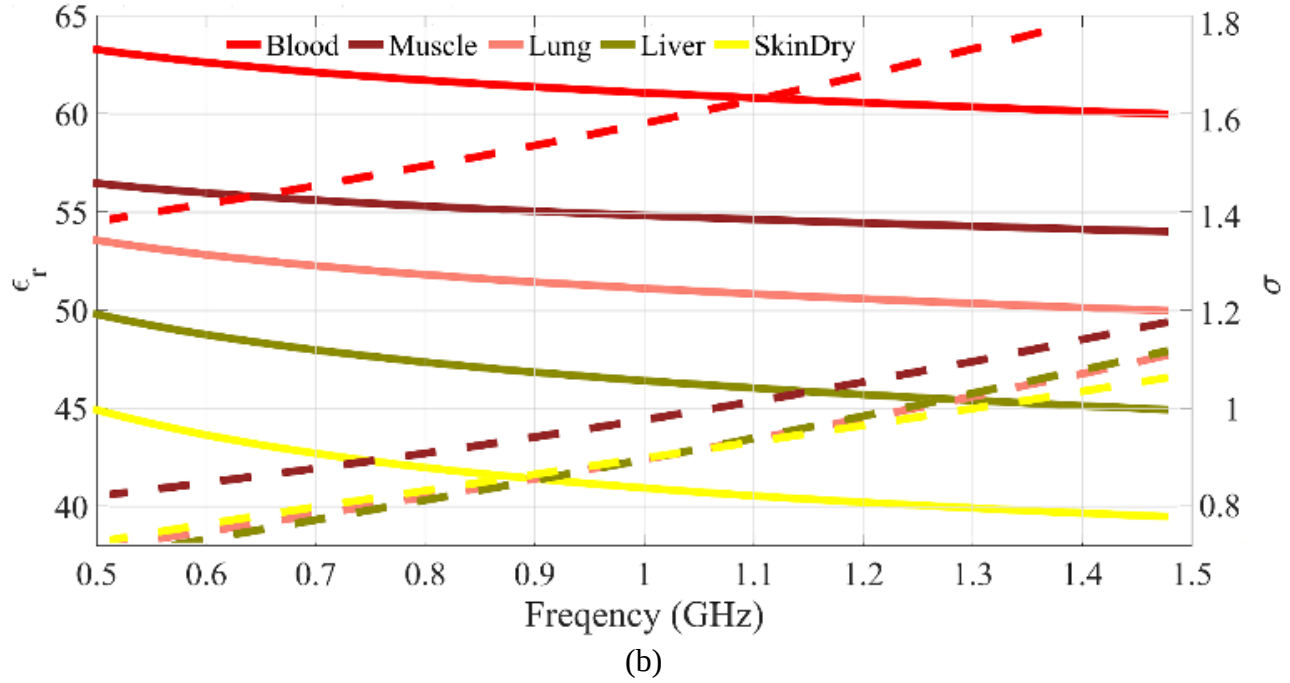

(b)

Fig. 6.7. (a) Dielectric properties of the training samples along with the ranges of variations for dielectric parameters of human torso tissues (coloured boxes), and (b) variation of relative permittivity (solid lines) and conductivity (dash lines) with frequency.

6.3.1 Simulations

The system is used to image a three-dimensional human torso model (EMAG model) including all of the torso tissues with their realistic dispersive properties (Fig. 6.7). The torso model and a multistatic antenna array are integrated with a multistatic frequency-based radar imaging algorithm to form a microwave torso imaging system (Fig. 6.8). To emulate the scenario of lung cancer patient, a 1 cm radius sphere of tissue with tumour properties is inserted inside one of the lungs.

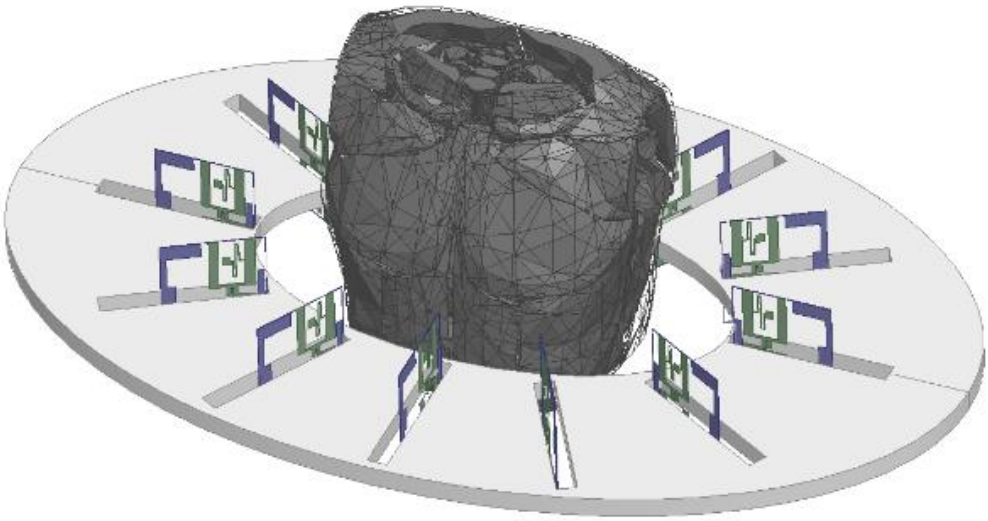

(a)

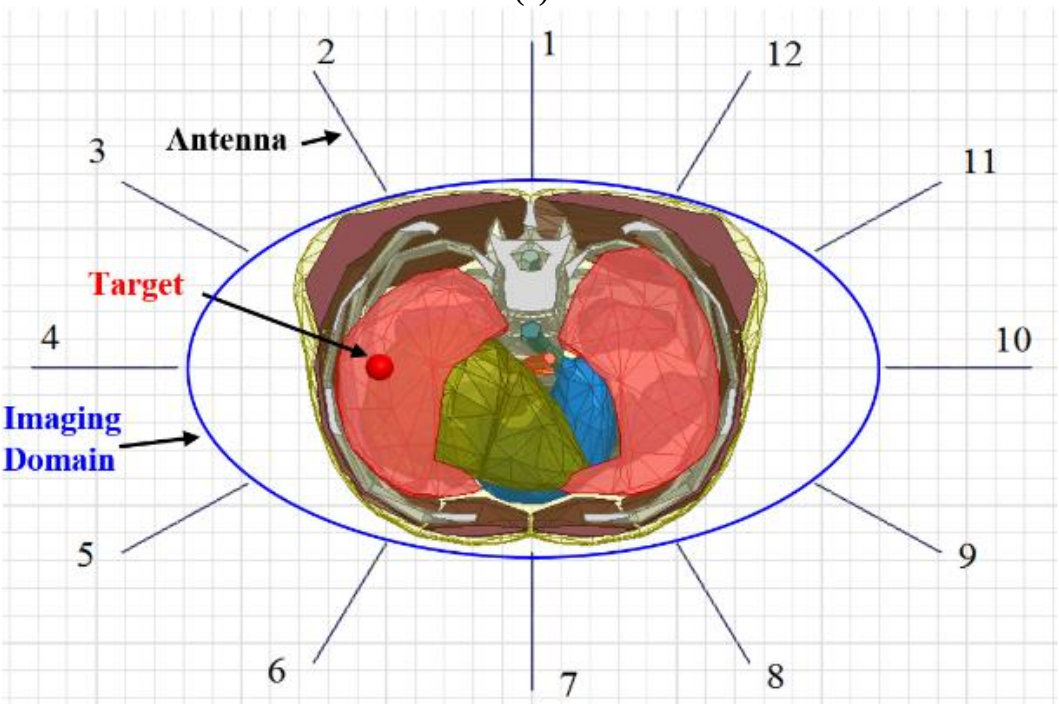

(b)

Fig. 6.8. Simulation setup to image an object (human torso), (a) side view and (b) cross-section up view.

The simulation is conducted in CST and the recorded S-parameters are regularised by (6.1). The regularised signals are then used for estimating the effective permittivity of the imaging domain by the obtained model in training using (6.6) and (6.7). The simulations are conducted for healthy (without tumour) and unhealthy (with tumour) cases to show effect of the change in the dielectric properties of the tissues in the estimation of the effective permittivity. The estimated relative permittivity and conductivity of the imaging domain at the centre frequency (1 GHz) from each antenna perspective are depicted in Fig. 6.9 for both healthy and unhealthy cases. Their values for antennas 1 and 4 over the used frequency band are also shown in Fig. 6.10.

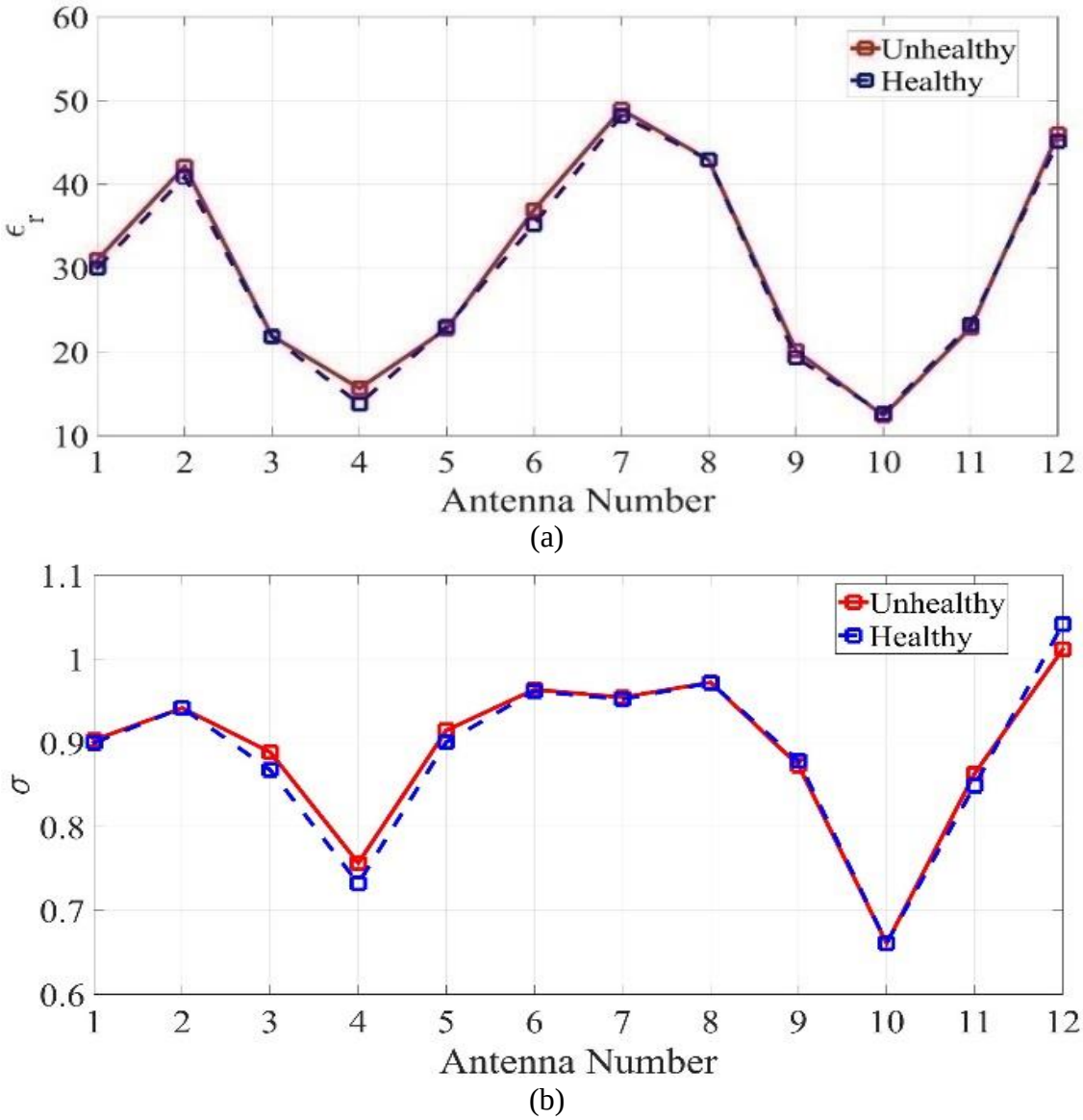

Fig. 6.9. Estimated dielectric properties at 1 GHz for each antenna. (a) Relative permittivity, and (b) conductivity.

As clearly shown in Fig. 6.9, the estimated permittivity and conductivity values of the unhealthy case are slightly larger than the values of the healthy one due to the presence of a small tumour with high dielectric constant in the unhealthy case. Of course, the slight difference in those values between healthy and unhealthy cases cannot be interpreted directly from Fig. 6.9 and Fig. 6.10 to determine whether a case is healthy or not. An efficient processing algorithm is still needed to create a clear image that enables accurate diagnosis. The aim of those figures is to demonstrate that the proposed method is quite sensitive even to a very small variation in the effective permittivity caused by a small abnormality, which may consequently aid better diagnosis in combination with proper processing techniques. That difference is more evident in the antennas that are close to the tumour location, especially antenna 4. Most importantly, the dielectric properties from the view-point of those antennas are lower than the observed values from the other antennas' perspective due

to the larger air gap between antennas 4 and 10, and the torso. On the other hand, the antennas that are close to the torso such as antennas 1, 2, 12, 6, 7 and 8, see the highest effective permittivity and conductivity. By using antenna-specific permittivity values in a radar-based imaging algorithm, the imaging results are expected to be more accurate and there is no need to adjust the distance between the antennas and the imaged object to be uniform.

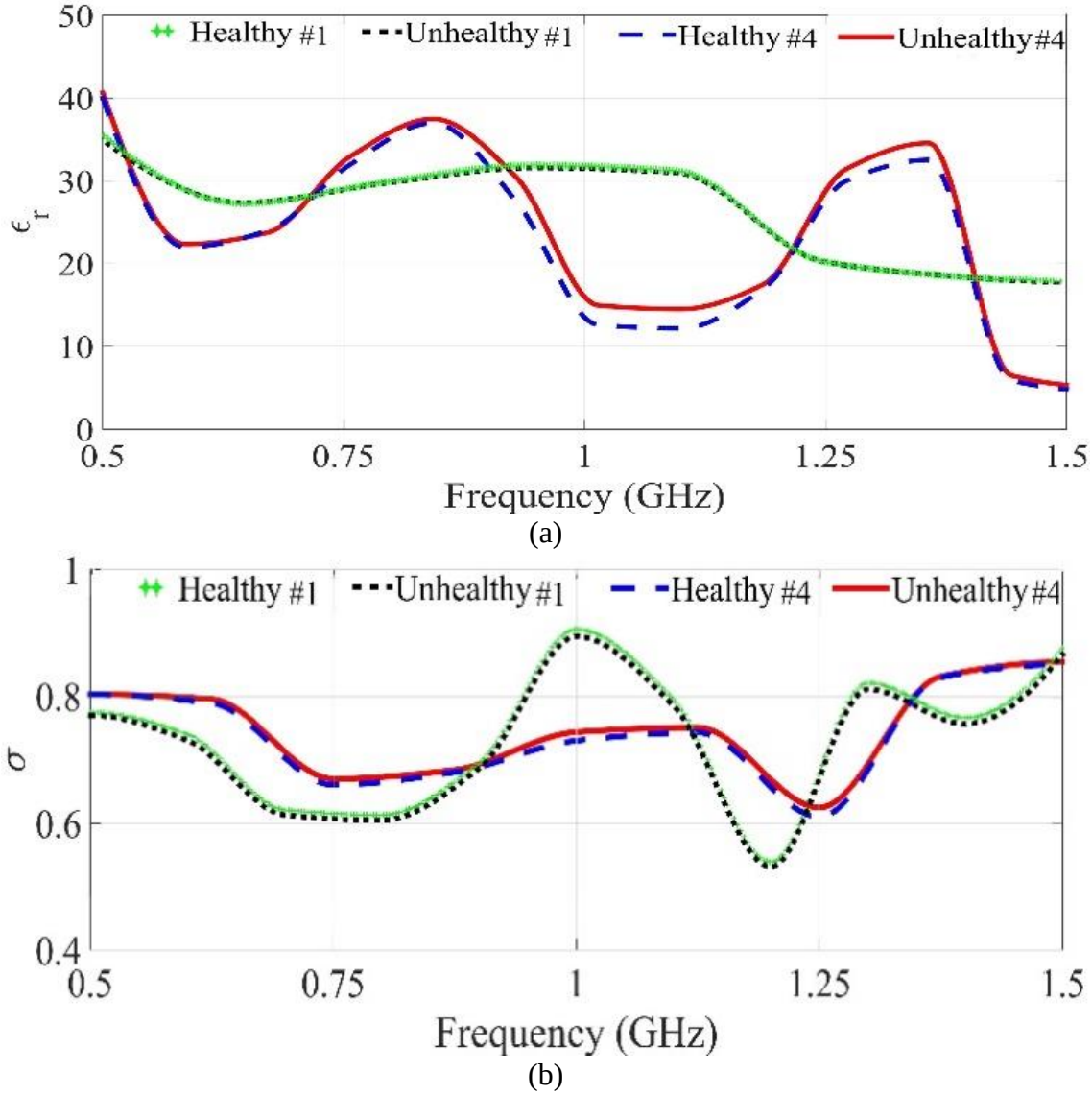

Fig. 6.10. Estimated dielectric properties for antenna 1 and 4 over the used frequency band. (a) Relative permittivity, and (b) conductivity.

Fig. 6.10 demonstrates that the proposed method can estimate the complex permittivity of the dispersive imaging domain. Since the torso includes many types of tissues with frequency dispersive properties, the estimated permittivity fluctuates over the investigated frequency band. The overall trend of the estimated relative permittivity of the torso indicates a decrease in value with frequency. This trend of variation follows the average trend of variation for the permittivity and conductivity of individual tissues as shown in Fig. 6.7 (b). The average values of the estimated

relative permittivity and conductivity over all of the antennas and frequencies are [ε_r, σ] = [29.78, 0.90] and [30.96, 0.91], respectively. It is worth noting that these values are the estimated permittivity of the whole imaging area, including the effect of the air gap between the antennas and the torso.

To investigate the efficacy of the proposed method in the image reconstruction procedure, the proposed frequency-based multistatic microwave imaging algorithm in Section 3 is modified and utilised to process the recorded data and create two-dimensional images. In the pre-processing step of the algorithm, the probability of the calibrated signals (4.22) are adjusted according to the corresponding wavenumber of receivers k_i:

$$P\left(rx_i, tx_j, f_k\right) = \frac{\beta(rx_i,tx_j,f_k)[S_{meas}\left(rx_i,tx_j,f_k\right)-S_{avg}(f_k)]^2}{\sum_{m=1}^{Na}\sum_{n=1}^{Na} w(n,m;f)[S_{meas}(n,m;f)e^{ik_i r}-S_{avg}(f)]^2} \ , \tag{6.8}$$

where,

$$\beta(i,j;f) = e^{-ik_i/|r_i-r_j|} \tag{6.9}$$

The adjusted probability functions are then used by (6.10) and (6.11) to remove the strong reflections from the outer layers (skin and muscle) based on the estimated wavenumbers from each antenna location.

$$H_3(f_k) = -\frac{1}{2}\log(\sum_{j=1}^{Na}\sum_{i=1}^{Na}\left[P\left(R_i,T_j;f_k\right)\right]^3) \tag{6.10}$$

$$S\left(R_i,T_j;f_k\right) = \begin{cases} S_{avg}^*(f_k) & e^{H(f_k)} \geq N_0 \\ S_{meas}\left(R_i,T_j;f_k\right) & otherwise \end{cases} , \tag{6.11}$$

After removing the strong reflections, the estimated permittivity values and the recorded signals are used by the imaging algorithm to show the distribution of power intensity inside the imaged region.

$$I(x,y) = \frac{1}{{N_a}^2}\left\|\sum_{k=1}^{Nf}\sum_{j=1}^{Na}\sum_{i=1}^{Na} S\left(rx_i,tx_j,f_k\right) J_1^2(k_i r)e^{-i2(k_i \boldsymbol{r}+\varphi)}\right\| \tag{6.12}$$

In the previous equation (3.18), a pre-known average permittivity value was used to calculate the wavenumber. While, in this equation, the estimated permittivity values from (6.7) which are specific to each antenna and each frequency step are used to calculate the wavenumber. The

reconstructed image can illustrate the location of tumour, which has higher dielectric properties than the healthy tissues of the torso.

Fig. 6.11 shows the reconstructed images using the traditional (one average value) and proposed antenna-specific permittivity estimation methods for two different locations. The considered average permittivity values in the traditional method (Fig. 6.11 (a) and (b)) are selected based on the best image quality technique. In this approach, the imaging domain is assumed to have different average dielectric constant values. The signal-to-noise ratio (*SNR*) metric of the obtained images from different assumed dielectric properties are then calculated by (4.25). *SNR* reflects the contrast between the target and background. Higher value of *SNR* means higher image quality. Therefore, relevant dielectric properties of the image with the maximum *SNR* value are selected as the dielectric properties of the imaging domain. The obtained average permittivity values from the traditional method are $[\varepsilon_r, \sigma] = [23, 0.8]$.

According to Fig. 6.11, the proposed method can successfully improve the image quality and detection accuracy. It is clear from Fig. 6.11 (a) and (b) that even using one overall average permittivity value can cause wrong detections by producing false and ghost targets; this happens due to the multipath phenomena occurring in the inhomogeneous torso. On the other hand, Fig. 6.11 (c) and (d) illustrate that applying the estimated permittivity values to the imaging algorithm provides more accurate detections than the conventional method (Fig. 6.11 (a) and (b)). In addition, since the estimation of the permittivity is done from the antenna's point of view, the non-uniform distance between the antennas and the torso does not affect the detection accuracy. Moreover, the distribution of the lung tissues with high permittivity values are also roughly revealed in those images. This achievement can lead to more reliable diagnosis of lung cancer and/or other relevant diseases. Although the exact boundaries of lungs are not clearly displayed in the image, the image quality can be improved by increasing the number of training samples, however at the expense of computational time and memory. It should be noted that strong reflections of the outer layers, including the skin and muscle tissues, are mitigated in the first step of the imaging algorithm (6.11). Hence, those tissues are not shown in the reconstructed images.

To investigate the quality and accuracy of the obtained images, *SNR* and the detection error (Δ) metrics are calculated to quantify the images. Knowing the assumed target size and locations, the metrics are calculated for the reconstructed images in Fig. 6.11, and listed in Table 6.2. The higher value of *SNR* and lower value of Δ for the images generated using the proposed method compared to the average permittivity method demonstrate superiority of the proposed method.

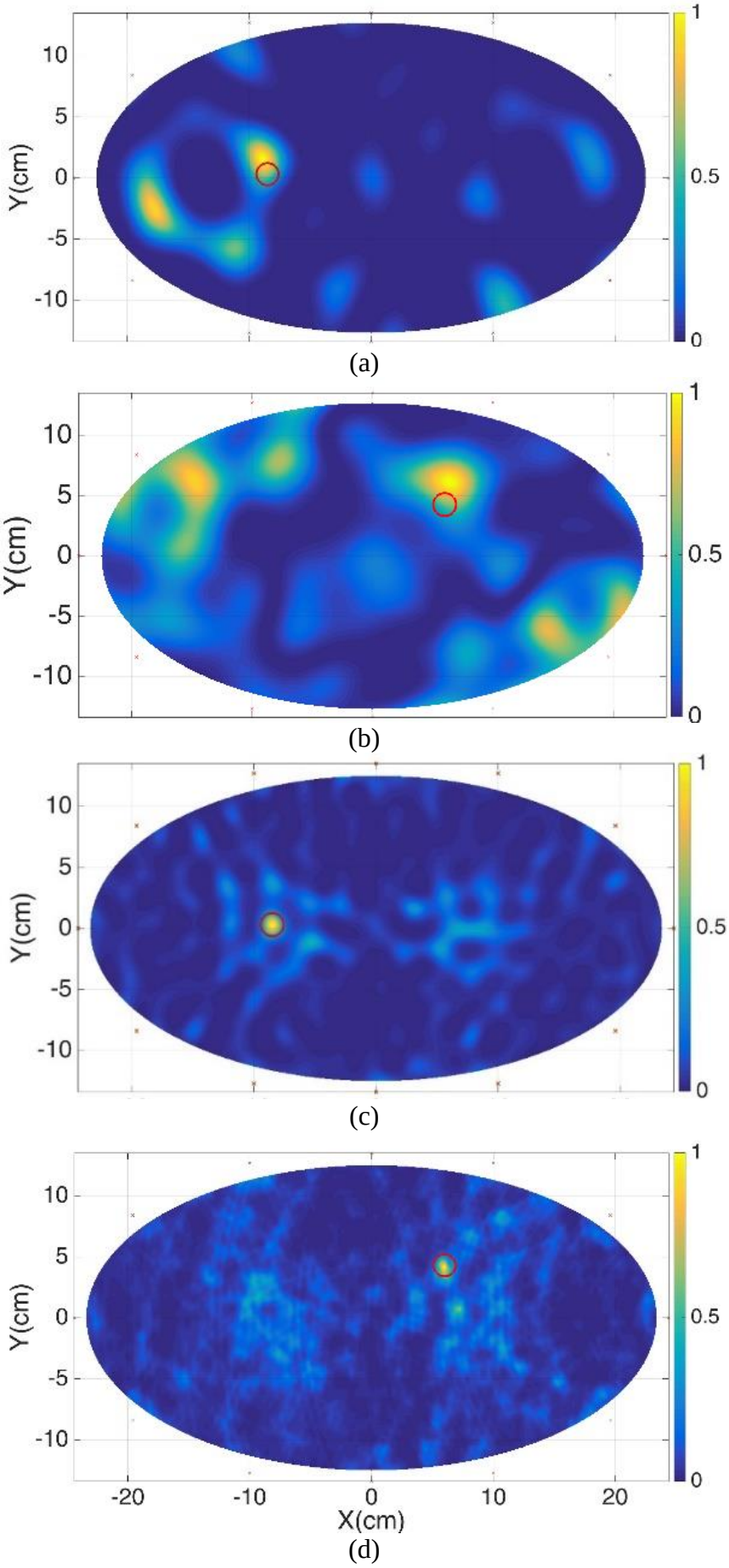

Fig. 6.11. Reconstructed images (a), (b) before, and (c), (d) after permittivity estimation.

Table 6.2. Image quality using conventional and proposed methods

Method	SNR (dB)	Δ (mm)	Figure
Average value	7.01	13.12	Fig. 6.11 (a)
Average value	3.34	19.90	Fig. 6.11 (b)
Proposed	12.08	0.00	Fig. 6.11 (c)
Proposed	11.50	1.12	Fig. 6.11 (d)

6.3.2 Experiments

In order to validate the performance of the proposed method in realistic environments, experiments were performed using an integrated microwave torso imaging system. Fig. 6.12 shows the configuration of the system. The data acquisition system contains a wall-mounted tube that encloses the subject under test. Twelve antennas are assembled inside the outer layer of the system to form a circular shape multistatic antenna array. The inner cavity is designed in an elliptical shape to form similar structure to that of the human torso. The outer layer of the system is built using expanded Polyvinyl chloride (PVC) with properties that are radio frequency (RF) transparent, and therefore, it does not affect the radiation performances of the antennas. The antennas are connected to a Keysight L4491A microwave switching system to scan the circumference of the torso. The switching network is connected to the ports of a Keysight N9923A FieldFox vector network analyser (VNA). The VNA generates the required microwave signal and measures the frequency response of the connected antenna between 0.65 and 1.75 GHz. The VNA and the switches are controlled by a laptop connected via Ethernet and USB connections. The explained torso phantom in Section 3, comprised of lungs, heart and abdomen block in addition to complete thorax ribs and muscle tissues (Fig. 3.15), is utilised. A 1 cm radius sphere built from materials that mimic the dielectric properties of tumour is inserted inside the phantom lung to imitate a lung cancer scenario.

To analyse the performance of the proposed method, the target is positioned inside the phantom's lung. The phantom is then scanned and collected data are used to estimate the permittivity of the imaging domain and construct an image of the phantom. Due to the complexity of the experiments and the huge number of required materials, the simulation-based training algorithm is used to estimate the permittivity values in experiments. To that end, the measured signals are calibrated by shifting the signal frequency and then multiplying them by the calibration factor a_c:

$$S_{cal}(f) = a_c S_{exp}(f - \Delta f) \tag{6.13}$$

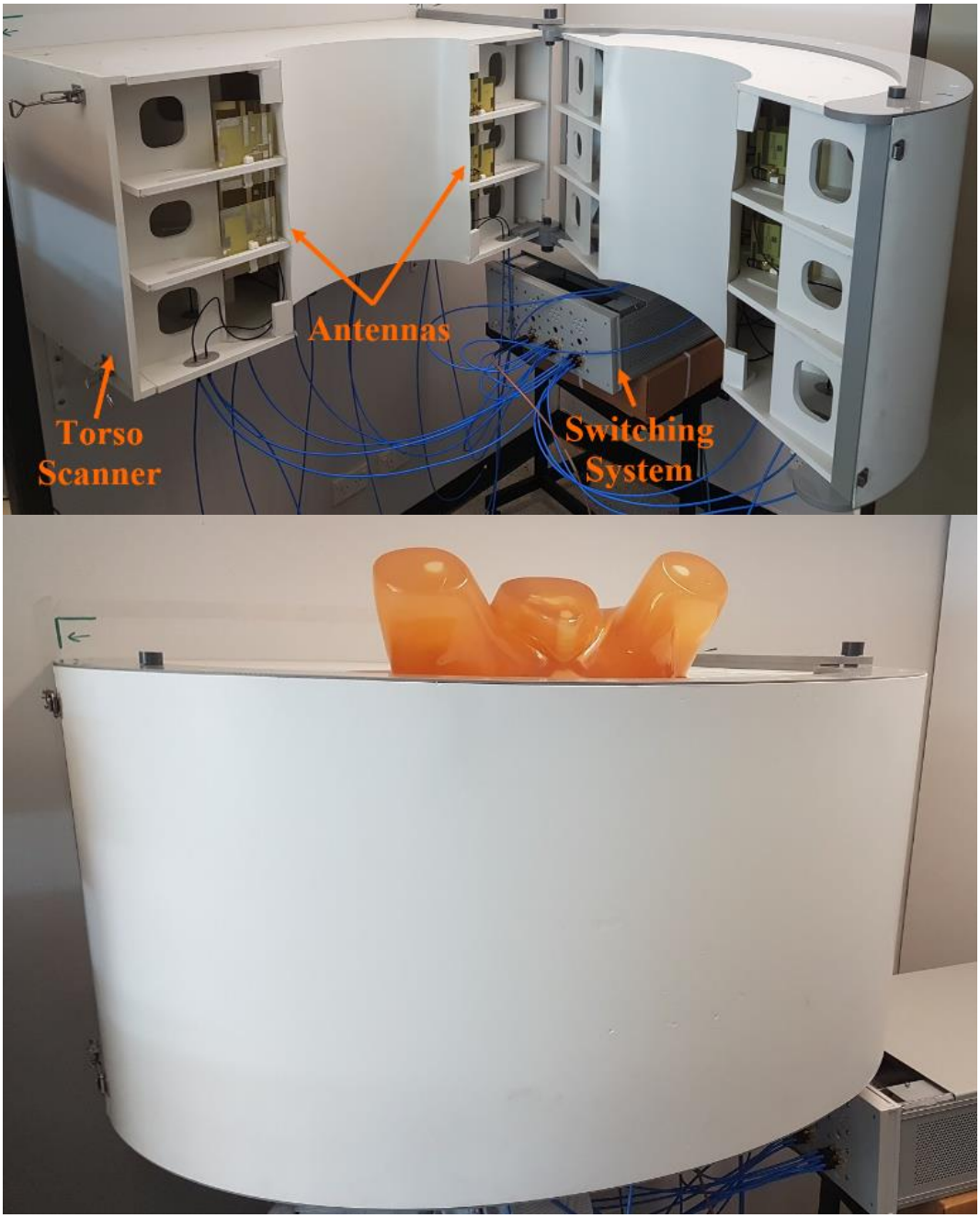

Fig. 6.12. Torso scanner opened to show its structure and then enclosing a torso phantom.

where, S_{cal} is the calibrated signal at frequency f, S_{exp} is the measured signal of experiment, and Δf is the frequency shift which is needed to calibrate the data against the variations in the resonant frequency of the simulated and measured S-parameters. The calibration factor a is calculated for a free space scenario, i.e. by dividing the shifted signals of measurement at free space (without phantom) $S_{exp}^{free}(f-\Delta f)$ by the simulation signals at free space $S_{sim}^{free}(f)$:

$$a = \frac{S_{exp}^{free}(f-\Delta f)}{S_{sim}^{free}(f)} \tag{6.14}$$

The calibrated signals are then used to estimate the dielectric permittivity values and create the final image.

The reconstructed image is shown in Fig. 6.13, where the small target is exactly detected in the imaging domain. The approximate distribution of the lungs tissues around the target can also be seen in this image.

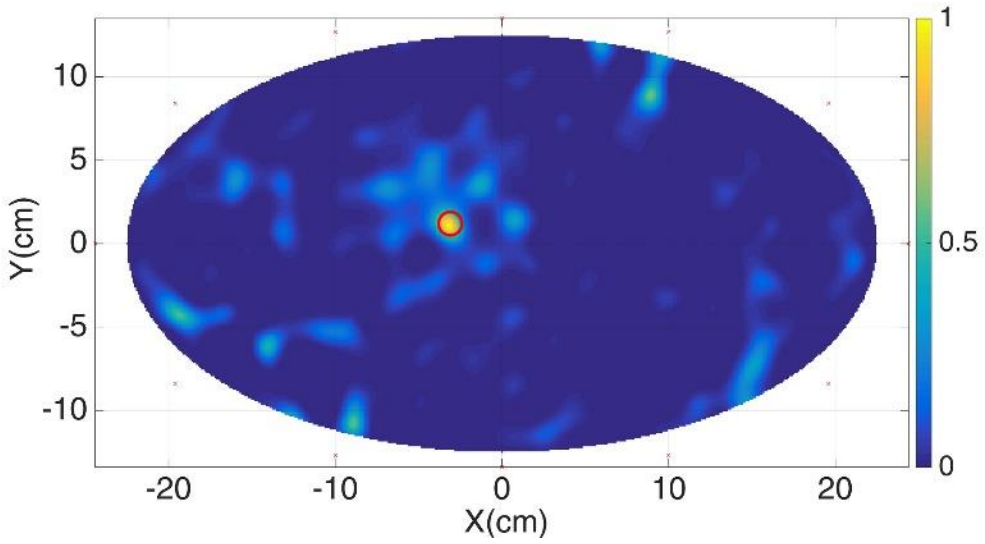

Fig. 6.13. Resultant image from experiment.

6.4 Summary

A technique for an accurate estimation of the frequency dispersive complex permittivity of an imaging domain has been presented in this chapter. The aim of the work is to improve the detection and imaging accuracy of multistatic microwave medical imaging systems. To that end, the complex permittivity from the viewpoint of each element is estimated to enhance the image quality. In the proposed technique, the recorded S-parameters are firstly spatially regionalized, and then a spatial statistical model of the dielectric permittivity is produced using a set of training media. The obtained model is used to estimate the frequency dispersive complex permittivity of the imaging domain from the viewpoint of each antenna. The estimated permittivity values are then used as a priori information in a multistatic frequency-based microwave imaging algorithm. The performance of the proposed method was tested using realistic-model simulations and experimentally verified in a torso imaging system where a lung tumour was successfully detected in a torso phantom. The comparison between the constructed images using the proposed and conventional methods shows superiority of the proposed method. In addition, by using the proposed method, there is no need to adjust the distance between the antennas and the imaged object to be uniform or even known as a priori information. This feature is quite important in clinical use of the imaging systems, where the imaged object can be located anywhere inside the imaging domain.

7 SURFACE ESTIMATION OF IMAGED OBJECT FOR IMPROVED MICROWAVE MEDICAL IMAGING

One of the main requirements for accurate imaging especially when not using a perfect coupling medium is the need to know the exact location of the imaged object within the imaging domain, i.e. the need for the exact distances between the imaging antennas and imaged object. The proposed method in the previous section tried to avoid detecting the location of the imaged object by imaging the whole imaging domain. Nevertheless, introducing the information about the boundaries of the imaged object into the imaging algorithms leads to an enhanced performance by reducing the reconstruction volume and hence computational time in tomography methods, and improving the accuracy of the propagation models used in radar-based imaging techniques. While it might be possible to manually measure that boundary in a controlled lab environment, this cannot be achieved in the clinical environment due to the impracticality of such a measurement in addition to the effect of the subject's natural movement.

In the literature, a variety of strategies were used to detect the imaged domain boundaries. For example, laser sensors were used in [112] to accurately detect the surface of the imaged object. However, laser scanning requires additional devices, which complicate the imaging system. Moreover, laser and microwave scans should be performed simultaneously to prevent false imaging due to patient movement/breathing during the scan. Other methods, including 2D and 3D matched-filter approaches [113]-[114], were developed based on the time delay in the wave propagation. However, the unpredicted delays due to the heterogeneous and multilayered structure of the human

body as explained in Chapter 4 and the presence of strong surface waves affect the accuracy of those methods.

In this chapter, a method for boundary identification at the same time of imaging and using the same data captured for imaging is presented. The method is based on the relation between the imaging antennas' resonant frequency and the location of the imaged object. The imaging antenna's resonant frequency shifts when that antenna faces an imaging object, which is effectively a lossy dielectric in biomedical application, and that shift depends on the distance between the antenna and the object. Since the number of imaging antennas is usually limited by the size of the antennas, level of acceptable mutual coupling and available apace, the virtual antenna array method, which is explained in Chapter 5, is also utilised to enhance the accuracy of the boundary estimation. The proposed technique is quite fast in scanning, computation and image creation as it does not need additional devices for the accurate boundary estimation. The method is tested via simulations and human trials using the torso imaging system.

7.1 Surface Estimation Using Antenna Resonant Frequency Shift

When an antenna faces an imaging object, its input impedance and thus radiation characteristics change significantly due to the loading effect of the object on the antenna. One of the outcome of that effect is a shift in the resonant frequency of the antenna compared to its free-space resonant frequency. That loading and thus the shift in the resonant frequency depend on the distance between the antenna and the object. This phenomenon is more obvious at higher frequencies, where the object becomes effectively much larger than the wavelength and thus high portion of the transmitted signal is reflected from the boundary of the imaged object. The relation between the antenna-imaged object distance and the resonant frequency shift can be utilised for the detection of the imaged object's boundaries.

The effect of the imaged object on the input impedance of the antenna is defined using the image theory [113] in the form of a mutual impedance. Assuming the skin (the outer boundary of the object) as a lossy ground plane located at the distance d from the antenna, a virtual antenna can be placed at the distance $2d$ from that antenna to account for reflections from the object. Based on the mutual coupling theory [115], it is possible to define the input impedance of the antenna Z_{in} as the combination of self-impedance Z_s and mutual impedance Z_m:

$$Z_{in} = Z_s + Z_m = (R_s + R_m) + j(X_s + X_m) \tag{7.1}$$

where R_s and R_m are self and mutual resistances, respectively, and Z_s and Z_m are self and mutual reactance, respectively. Using the induced EMF method [115], the self and mutual reactance values for an antenna operating at the dipole mode, like the antenna used in this work, can be roughly defined as:

$$R_s = \frac{\eta}{4\pi \sin^2\left(\frac{kl}{2}\right)}\left\{0.577 + \ln(u_0) - C_i(u_0) + \frac{1}{2}\sin(u_0)\left[S_i(2u_0) - S_i(u_0)\right] + \frac{1}{2}\cos(u_0)\left[0.577 + \ln\left(\frac{u_0}{2}\right) + C_i(2u_0) - 2C_i(u_0)\right]\right\}, \quad (7.2)$$

$$X_s = -120\frac{\left[\ln\left(\frac{l}{2a}\right)-1\right]}{\tan\left(\frac{kl}{2}\right)}, \quad (7.3)$$

$$R_m = \frac{\eta}{4\pi}\left[2C_i(u_0) - C_i(u_1) - C_i(u_1)\right], \quad (7.4)$$

$$X_m = \frac{\eta}{4\pi}\left[2S_i(u_0) - S_i(u_1) - S_i(u_2)\right], \quad (7.5)$$

where, η is the intrinsic impedance of the medium,

$$u_0 = 2dk \quad (7.6)$$

$$u_1 = k\left(\sqrt{4d^2 + l^2} + l\right) \quad (7.7)$$

$$u_2 = k\left(\sqrt{4d^2 + l^2} - l\right) \quad (7.8)$$

k is the wavenumber, and l and a are constants to be found depending on the exact structure of the antenna. For simple dipole antennas, the parameters l and a are the length and diameter of the dipole, respectively. C_i and S_i are the cosine and sine integrals, respectively:

$$C_i(u) = \int_{\infty}^{u} \frac{\cos(x)}{x}\,dx \quad (7.9)$$

$$S_i(u) = \int_{0}^{u} \frac{\sin(x)}{x}\,dx \quad (7.10)$$

Attaching the antenna to a signal generator with an impedance of Z_g = 50 Ω, the reflection coefficient S_{11} of the antenna is:

$$S_{11} = \frac{Z_{in}(f) - Z_g}{Z_{in}(f) + Z_g} \tag{7.11}$$

Hence, the resonant frequency of the antenna can be calculated as the frequency at which the reflection coefficient of the antenna is minimum:

$$f_r = \arg\min_f |S_{11}| \tag{7.12}$$

As an example, Fig. 7.1 (a) shows the calculated resonant frequency of a dipole antenna with $l = \lambda/2$, $a = 10^{-5}\lambda$ (λ is the wavelength), designed to have a free space resonant frequency of 1 GHz for different distances from a perfect ground plane as a reflector. It is clear that the resonant frequency of the dipole fluctuates with distance around the free-space resonance and settles at that frequency (1 GHz) at large distances. For the practical distances used in microwave medical imaging, such as the torso imaging as the topic of this work, the relation between the resonant frequency and antenna-reflector distance is as depicted in Fig. 7.1 (b).

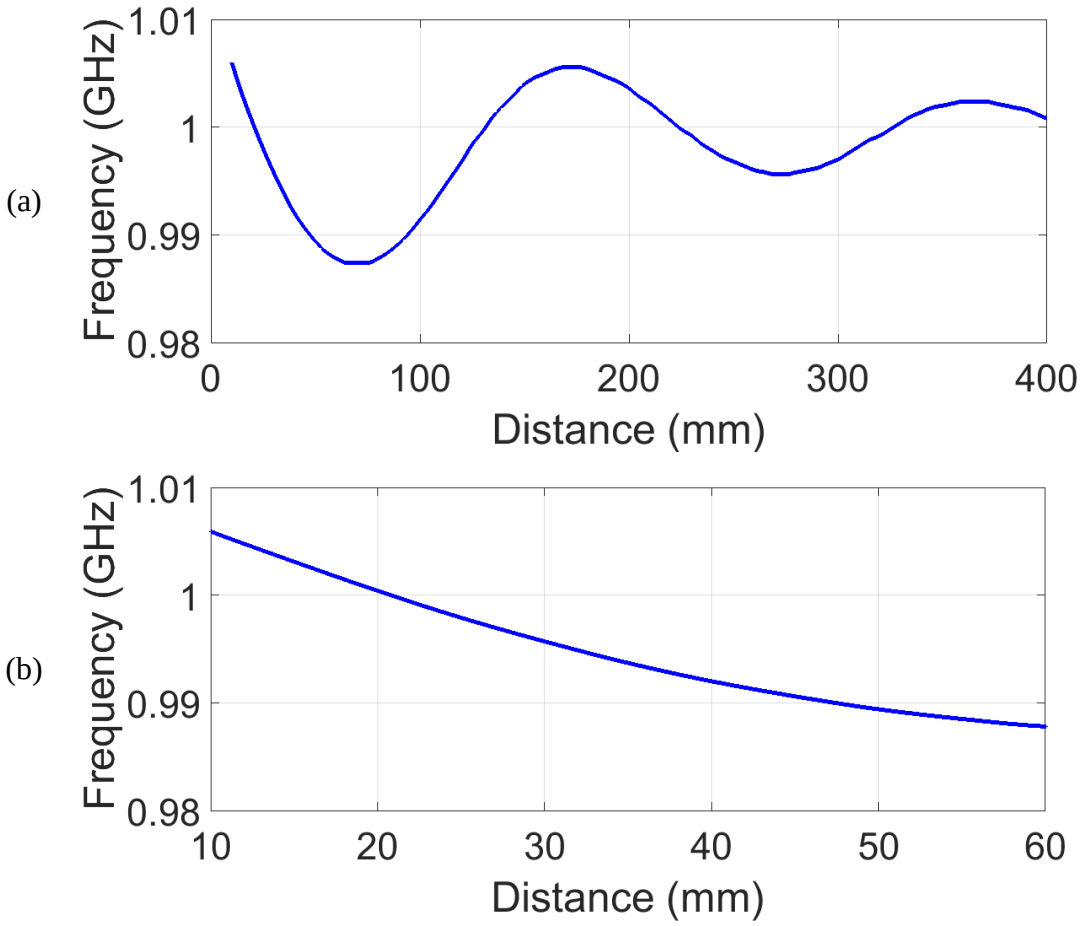

Fig. 7.1. (a) Calculated resonant frequency of an antenna operating in the dipole mode with antenna-ground plane distance, and (b) zoomed-in plot of (a) to include the distances of interest in microwave torso imaging.

To verify the abovementioned notion, a printed dipole antenna with free space resonant frequency of 1 GHz is simulated in HFSS at different distances from a realistic human torso model. The resonant frequency variation is presented in Fig. 7.2. The general trend of variation for the practical antenna-object distances in torso imaging agrees well with the calculations (Fig. 7.1 (a)). However, the resonant frequency depicted in Fig. 7.2 at specific distances do not have the same calculated values shown in Fig. 7.1 (b) as for that figure, the object was assumed a perfect reflector.

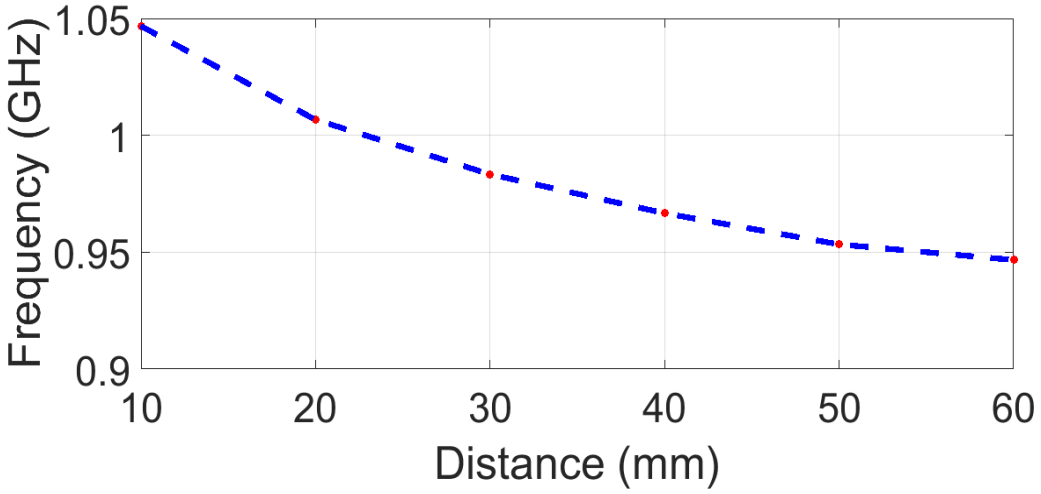

Fig. 7.2. Measured resonant frequency of antenna operating in the dipole mode with antenna-torso distance for the practical distances used in torso imaging.

In microwave medical imaging, the inverse calculation of (7.1)-(7.12), i.e. to find the distance from the resonant frequency, is needed. However, the inverse solution of (7.1)-(7.12) or another similar analysis for a specific antenna results in a transcendental (non-algebraic) equation, which is multivalued due to the sine and cosine integral functions. We can adopt a simpler approach for the inverse solution to (7.1)-(7.12). First, we use them to find the general relation between the antenna's resonant frequency and the antenna-object distances for the practical range of distances used in the imaging scenario as shown in Fig. 7.1 (b) for torso imaging. The results indicate a quadratic relation between the resonant frequency and distance. Hence, the minimisation problem (7.12) can be replaced with a quadratic polynomial function:

$$d = a_0 f_r^2 + a_1 f_r + a_2 \tag{7.13}$$

where f_r is the resonant frequency, and $a_{j\ (j\ =\ 0\ to\ 2)}$ are constants to be found. To determine the quadratic constants a_j, the function needs to be trained in a full-wave simulation environment that includes the antenna array and a realistic model of the imaged object such as the torso.

In microwave medical imaging, an array of antennas surrounds the imaged object to image a cross section of the object. Knowing the location of the imaging antennas, the imaged object's boundary can be estimated using (7.13) for all of the array elements around the object. Calculating the quadratic parameters for all antennas may slightly enhance the estimation, but at the cost of conducting too many calculations/measurements to obtain the fitted functions for all of the antennas. On the other hand, the human torso is not flat of course; therefore, using a simple flat boundary for parameters estimation causes some avoidable deterioration in the accuracy. As a compromise solution, the calculated parameters of one antenna in front of the torso are used for all other antennas. In this case, a set of points with an equal number of antennas is generated. Connecting all of those points in the imaging domain creates the estimated boundary of the object. However, due to the limited number of imaging antennas, the estimated points may not cover the entire boundary of the object. Therefore, the extended virtual array technique, which is explained in Chapter 5, is utilised to increase the number of estimated points to achieve a uniform sampling across the entire boundary. The resonant frequency of the predicted signals at virtual locations of the virtual array with more elements than the real one are detected and applied to (7.13) to find the distance between the antennas (including real and virtual ones) and the boundary of the imaged object. Using the virtually augmented boundary points provides an approximately uniform boundary estimation across the entire object's circumference without using additional real antennas.

In the abovementioned technique, the captured signals from simulations are used in both the antenna's parameters calculation and the object's boundary detection procedures. However, due to the possible difference in the resonant frequency of the simulated and manufactured antennas, the obtained function from simulations cannot be directly used for the measured data. Therefore, the signal calibration process explained in Chapter 6 is used to align the measured data to the simulation signals. Finally, the resonant frequencies of the calibrated signals by (6.13) are applied to (7.13) to estimate the boundary of the imaged subject in experiments.

To create two or three-dimensional images, the estimated boundary is applied to a microwave imaging algorithm. In that regard, the wave propagation model is upgraded to a two-layer model in which the first layer is the air gap between the antenna and the skin, and the second layer consists of other tissues inside the imaged object:

$$I(x,y) = \frac{1}{{N_a}^2} \left\| \sum_{k=1}^{Nf} \sum_{j=1}^{Na} \sum_{i=1}^{Na} S\left(rx_i, tx_j, f_k\right) J_1^2(k_0 r_{0i} + k_{1i} r_{1i}) e^{-i2(k_0 r_{0i} + k_{1i} r_{1i} + \varphi)} \right\| \qquad (7.14)$$

where, the single average wavenumber in (3.18) is replaced by k_{0i}, the vacuum wavenumber and $k_{1i} = 2\pi f(\varepsilon_{1i}\mu)^{1/2}$, and the wavenumber in the imaged object from the view point of ith antenna. r_{0i}

and r_{1i}, the distance from receiver to the skin and from the skin to the scatterer are also added to the algorithm.

7.2 Validation and Results

7.2.1 Simulations

The collected data from the simulation setup for the microwave torso imager system, which is explained in Chapter 6 and shown in Fig. 6.8 are used to test the proposed method. Using the proposed function (7.13), simulations are conducted for different distances between the antenna and the torso to determine the parameters a_j. The highest resonant frequency of the imaging antenna (1.2 GHz as depicted in Fig. 6.4 b) is used in the boundary detection process as the antenna operates in the dipole mode at that frequency. The obtained reflection coefficients for different distances are shown in Fig. 7.3. As shown, the reflection coefficient shifts with the change of distance between the antenna and the torso, so that the minimum value of the reflection coefficient moves from high frequencies to low frequencies when the distance increases. The resonant frequencies at which minimum values of the backscattered signals occur (red dots in Fig. 7.3) are recorded and utilised to fit the function to those data.

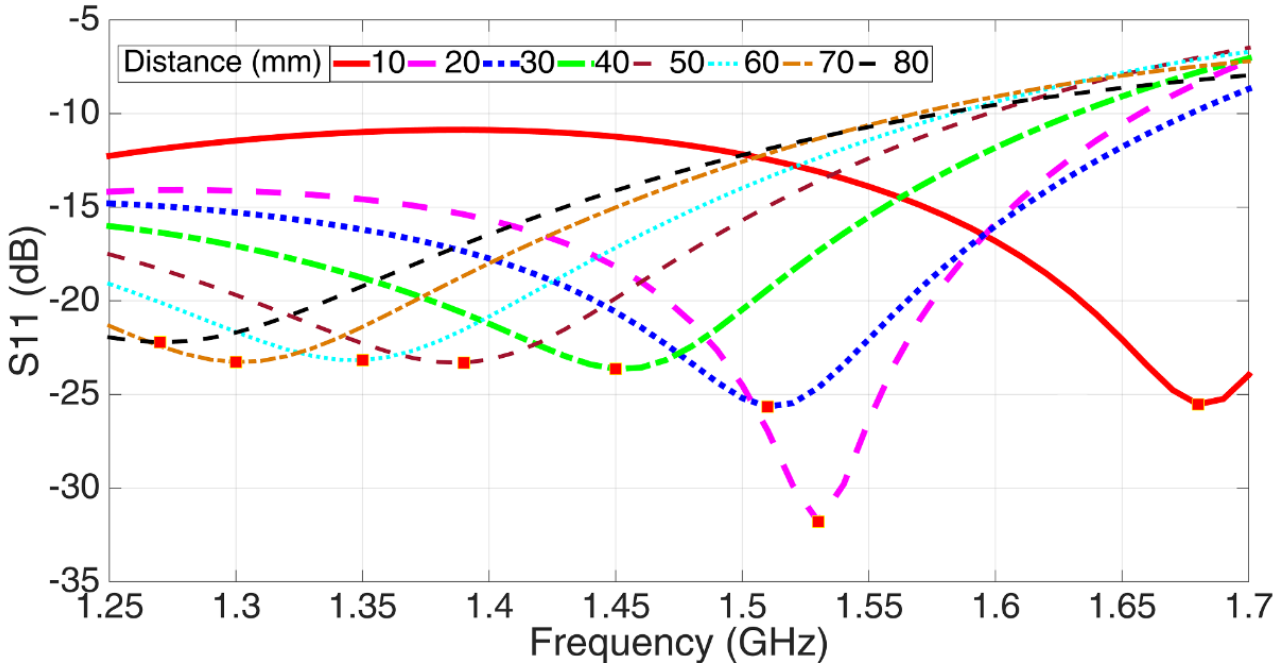

Fig. 7.3. Scattering parameters of the imaging antenna when facing the imaged object located at different distances.

To study the effect of different skin thicknesses, tissue types and boundary curvature on the performance of the antenna, the simulations are repeated for antenna #3 and #5 that face different curvatures and thicknesses of the skin. The fitted functions compared to the obtained simulated data

are shown in Fig. 7.4. It is clear from Fig. 7.4 that the aforementioned factors within the realistic range of values do not significantly affect the antenna's resonant frequency. Hence, the calculated quadratic parameters of one of the antennas can be used for all of the antennas to speed up the boundary estimation procedure without adversely affecting the estimation accuracy. It should also be noted that with the utilized antenna, the quadratic function fits to the recorded data quite well of antenna-torso distances up to 100 mm. Hence, the proposed method can detect the boundaries within that designed range, 10-100 mm, which is a reasonable range for the torso imaging system.

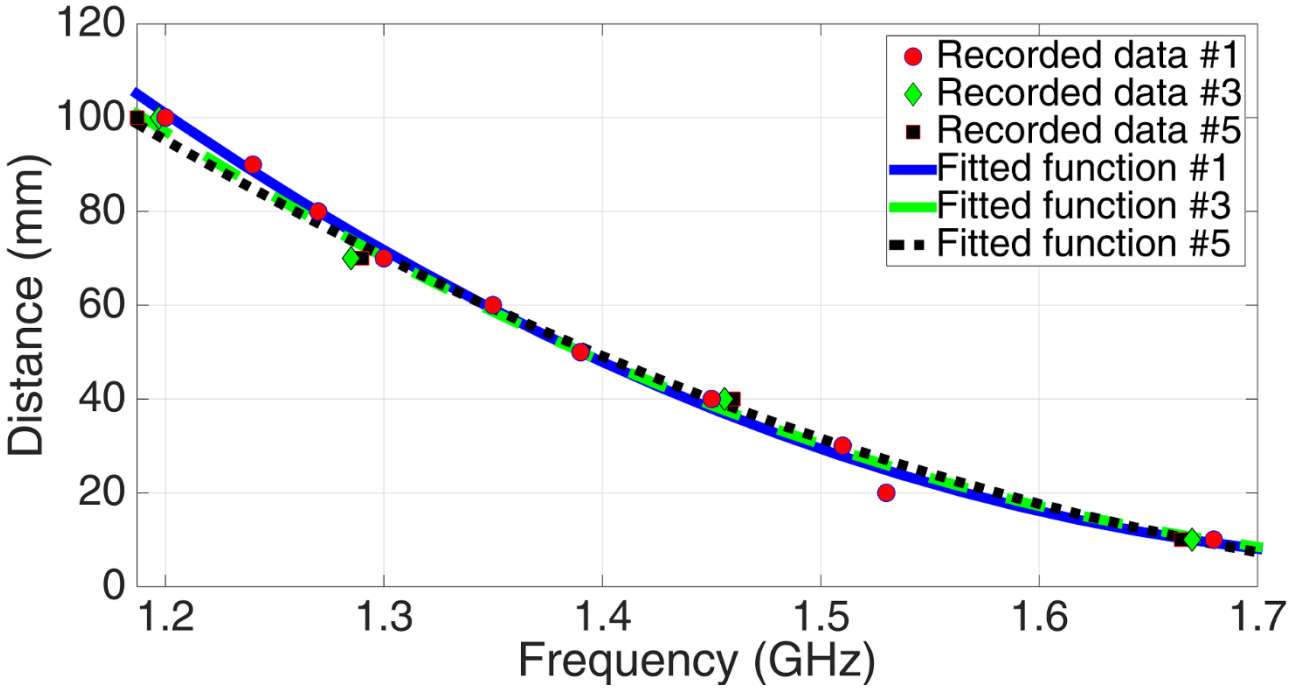

Fig. 7.4. The distance between the antenna and skin as a function of resonance frequency.

To get more estimated points on the boundary of the torso, the explained virtual array method is used to expand the recorded data from the 12-element array to 24, and 36-element virtual array distributed around the torso uniformly. The frequency-domain received signals by the 12-element array are used in (5.6) to generate the required S-parameters. The generated virtual signals along with the collected ones are then applied to (7.13) to estimate the distance between each antenna and the skin, and hence create the torso boundary. Fig. 7.5 shows the constructed boundary of the torso using the proposed boundary identification method with 12 real elements, 24 and 36 virtual antennas. According to Fig. 7.5, the torso boundaries can be reasonably detected using the proposed method. There are some errors in the boundary estimation of the locations where the antennas are not perpendicular to the skin and hence the electromagnetic wave is not directly reflected back to the antenna. However, increasing the number of imaging antennas by the virtual technique improves its accuracy in estimating the entire boundary.

(a)

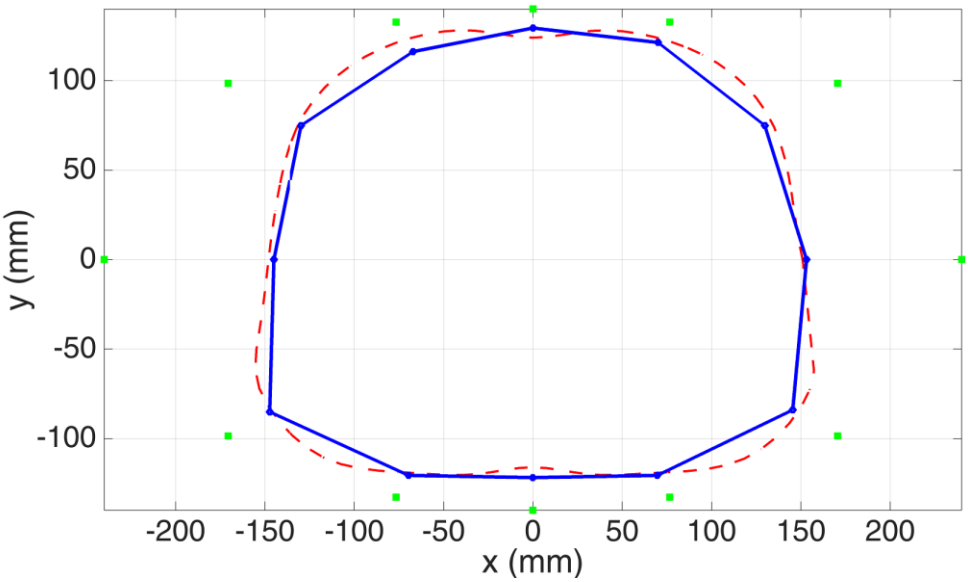

e_{max}=11.4mm

e_{avg}=6.5mm

(b)

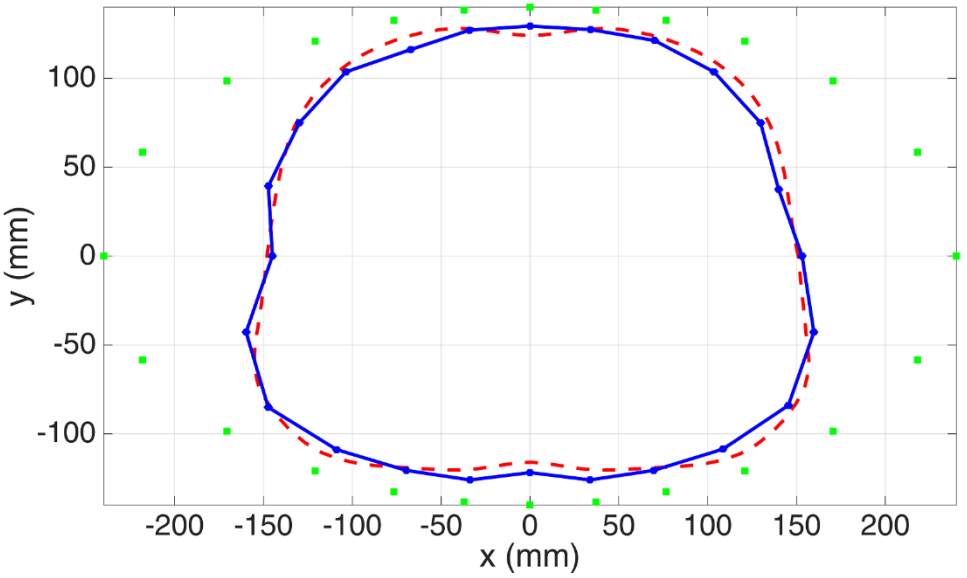

e_{max}=11.4mm

e_{avg}=6.5mm

(c)

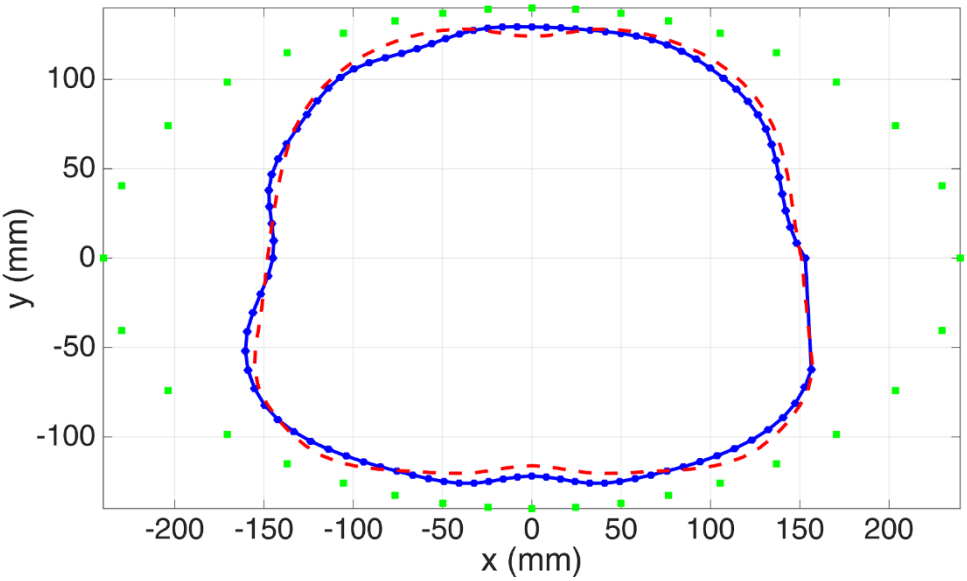

e_{max}=11.4mm

e_{avg}=6.5mm

Fig. 7.5. Constructed surface with (a) 12 real antennas, (b) 24, and (c) 36, virtual antennas. Blue solid lines show the estimated boundary location; red dashed lines show the exact boundary of the torso and green squares show the location of the antennas.

To quantify the accuracy of the estimated boundaries, the estimation error as a difference between the estimated and actual torso boundaries are calculated and shown beside images in Fig. 7.5 where, e_{max} and e_{avg} represent the maximum and the average errors of the estimated torso boundaries. The maximum estimation error for twelve, 24 and 36 antennas are 11.4, 7.9 and 7.7 mm, respectively. It is clear from the calculated values of Fig. 7.5 that increasing the virtual antennas decreases the error. However, there is no significant improvement in the estimation accuracy when increasing the virtual elements from 24 to 36. Increasing the number of antennas significantly means that neighbouring antennas get closer to each other and they get the same information about the boundary of the imaged domain. In other words, using 24 virtual antennas from 12 real antennas give the best possible improvement in the boundary detection with minimum computational efforts.

To examine the effect of the boundary estimation on the imaging results, the proposed method is applied to the modified radar-based multistatic imaging algorithm (7.14). In this analysis, an unhealthy case (lung cancer) is emulated by inserting a 1 cm-radius sphere of blood inside the torso phantom. Fig. 7.6 shows the reconstructed images using the conventional one-layer model (imaging the whole domain) and the two-layer model with the proposed boundary estimation method (only imaging the object after detecting its boundary), for two different target locations. According to Fig. 7.6, the proposed method can successfully improve the image quality and detection accuracy. It is clear from Fig. 7.6 (a) and (b) that using one-layer model, i.e. without knowing boundaries of the torso, causes wrong detections with false and ghost targets. On the other hand, Fig. 7.6 (c) and (d) illustrate that applying the estimated torso boundary to the imaging algorithm provides highly accurate detections with no ghost targets. Moreover, those results show that the radar imaging algorithm is not overly sensitive to the small amount of boundary estimation errors. As depicted in Table 7.1, knowing the assumed target size and locations, the quality of the images is improved significantly.

Table 7.1. Image quality without and with boundary detection using the proposed method

Method	*SNR* (dB)	Δ (mm)	Figure
Without (case 1)	7.01	13.12	Fig. 7.6 (a)
Without (case 2)	3.34	19.90	Fig. 7.6 (b)
With (case 1)	12.08	2.10	Fig. 7.6 (c)
With (case 2)	11.50	6.91	Fig. 7.6 (d)

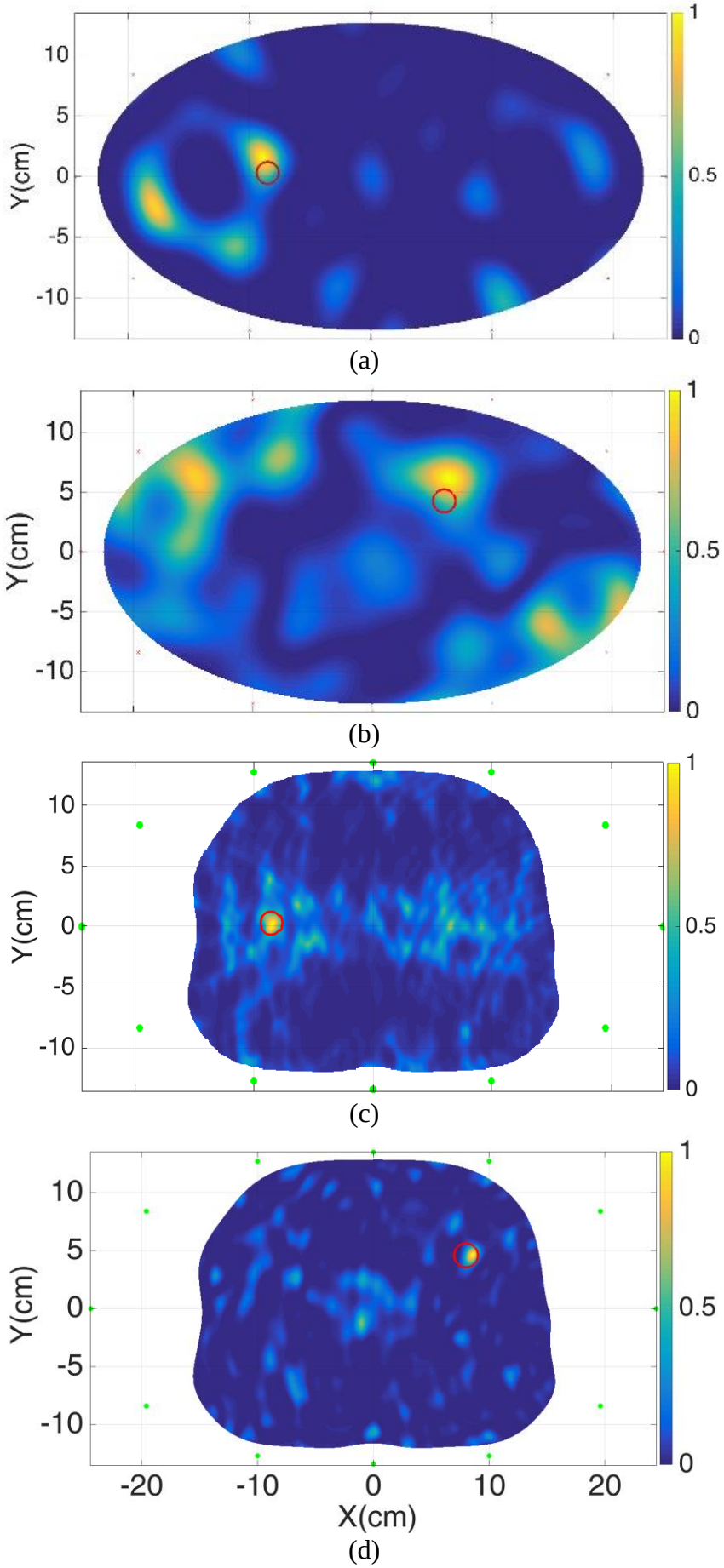

Fig. 7.6. Reconstructed images (a), (b) without, and (c), (d) with boundary estimation.

7.2.2 Human Test Results

Experiments using the torso imaging system explained in Chapter 6 were conducted to validate the method. To analyse the performance of the proposed method, it is tested on healthy subjects (Fig. 7.7). All of the tests were conducted in accordance with the guidelines and protocols approved by the Ethics Committee of The University of Queensland, Australia with the approval number of 2017000185 and under an unrestrained environment where the effects of subject's movement and breathing, and external noise are included in the measurements. The collected data are calibrated using (6.13) and then used in (7.13) to find the boundary of the subjects under test. To de-identify the studied cases, the obtained results from two random human subjects are depicted in Fig. 7.8. As it is clear from Fig. 7.8, the proposed method can clearly estimate the boundary of human subjects. However, it is extremely difficult to measure the exact location of the entire boundary of the subjects while being scanned inside the imaging system. Hence, we asked one of the subjects to stay in a fixed position, while one antenna is moved in a normal direction to the torso to change its distance from the torso skin from 10 mm to 100 mm. The signals are measured for every 10 mm intervals and the proposed method is used to estimate the distances. The bar-chart of Fig. 7.9 shows that the proposed method can accurately determine the distance between the antenna and the subject with sub-errors. The average and the maximum distance estimation errors are 5 mm and 6 mm respectively, which is within the range of the calculated values of the simulation results (Fig. 7.5).

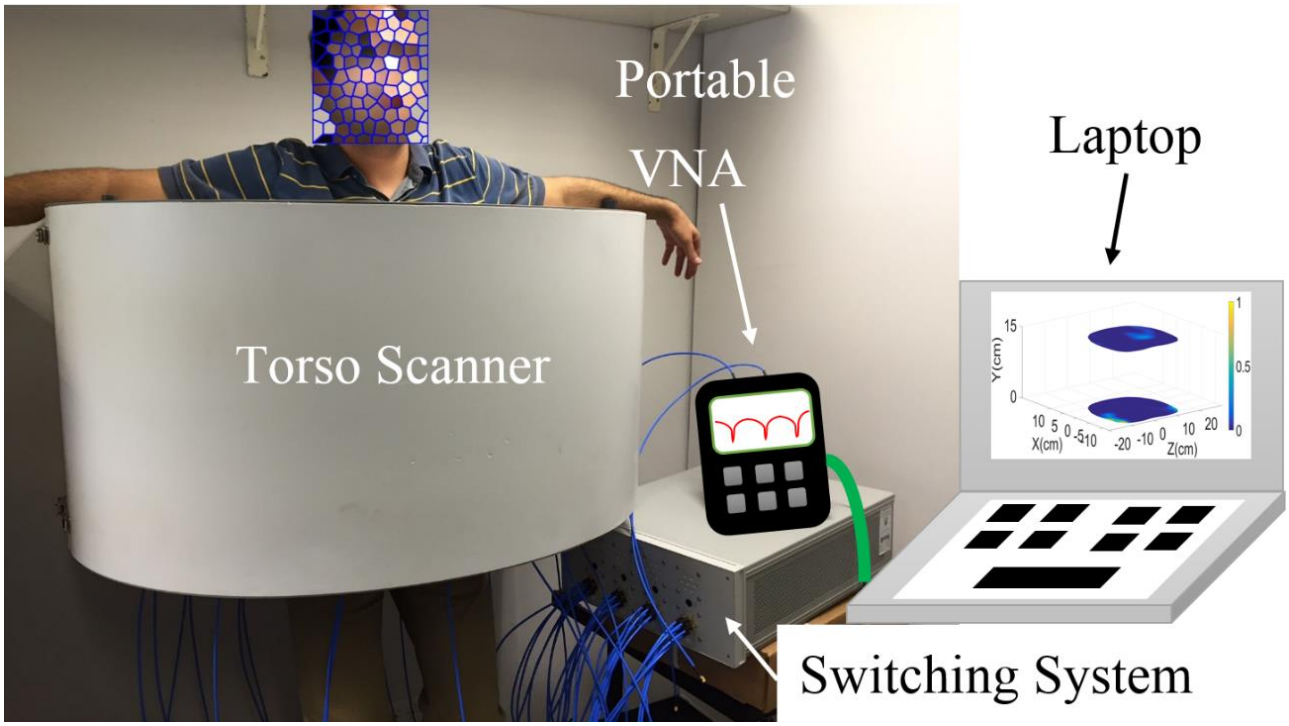

Fig. 7.7. Torso scanner system.

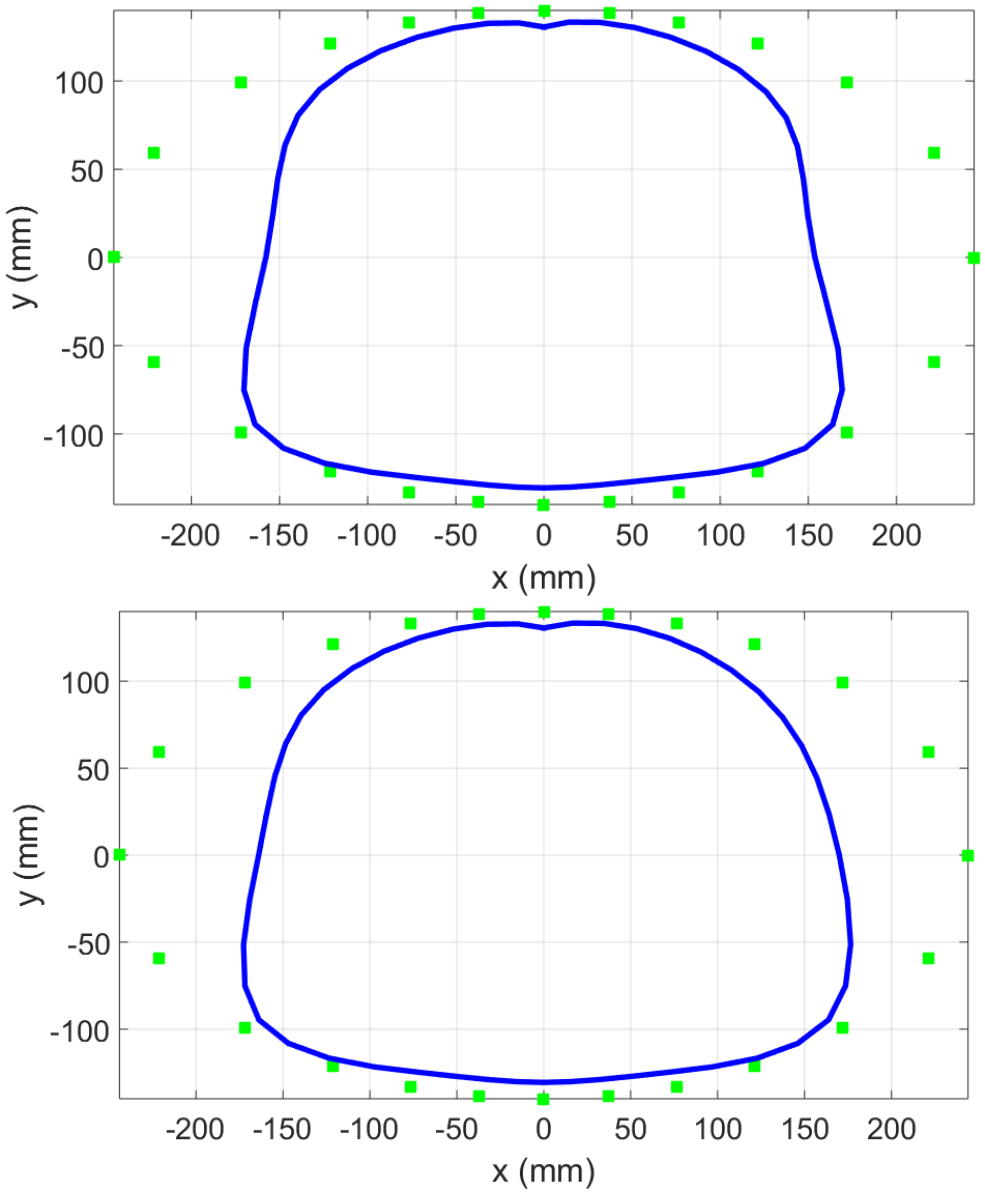

Fig. 7.8. Constructed surfaces for human subjects.

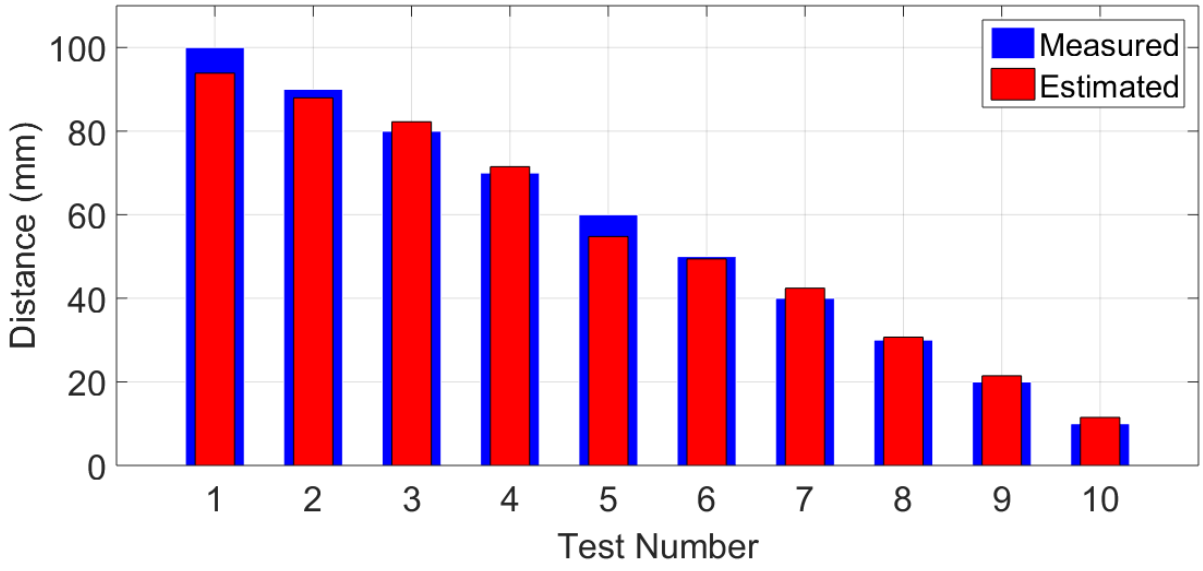

Fig. 7.9. Comparison between the estimated and exact distances in experiments.

7.3 Comparison

To compare the proposed method with existing boundary estimation methods, the 2D time-domain approach [101] is used to process the same simulated datasets. The time-domain method uses matched-filter approach from space-time beamforming technique to estimate the propagation time from each antenna position to the skin surface. Then piecewise-surface-fit method is used to generate approximately uniform distributed points over the surface. Fig. 7.10 shows the obtained boundaries using the aforementioned method to process the simulated data collected from 12 antennas. It is obvious from Fig. 7.10 that the matched-filter approach (blue solid line) cannot accurately generate the torso boundary, especially at highly curved sections of the torso, where there is a thicker layer of skin than the other parts of the processed torso model. A thicker layer of skin causes more delays in the electromagnetic wave propagation and hence wrong distance estimations by the time-domain based methods. The maximum and average estimation errors for the matched-filter method are compared with the proposed method when 24 virtual antennas from 12 antennas (the best compromise between quality of image reconstruction and simplicity of implementation) are used. The results are listed in as shown in Table 7.2. It is quite clear that the proposed method can accurately detect the boundary of the torso in the same simulated environment with significantly less estimation errors than the matched-filter method.

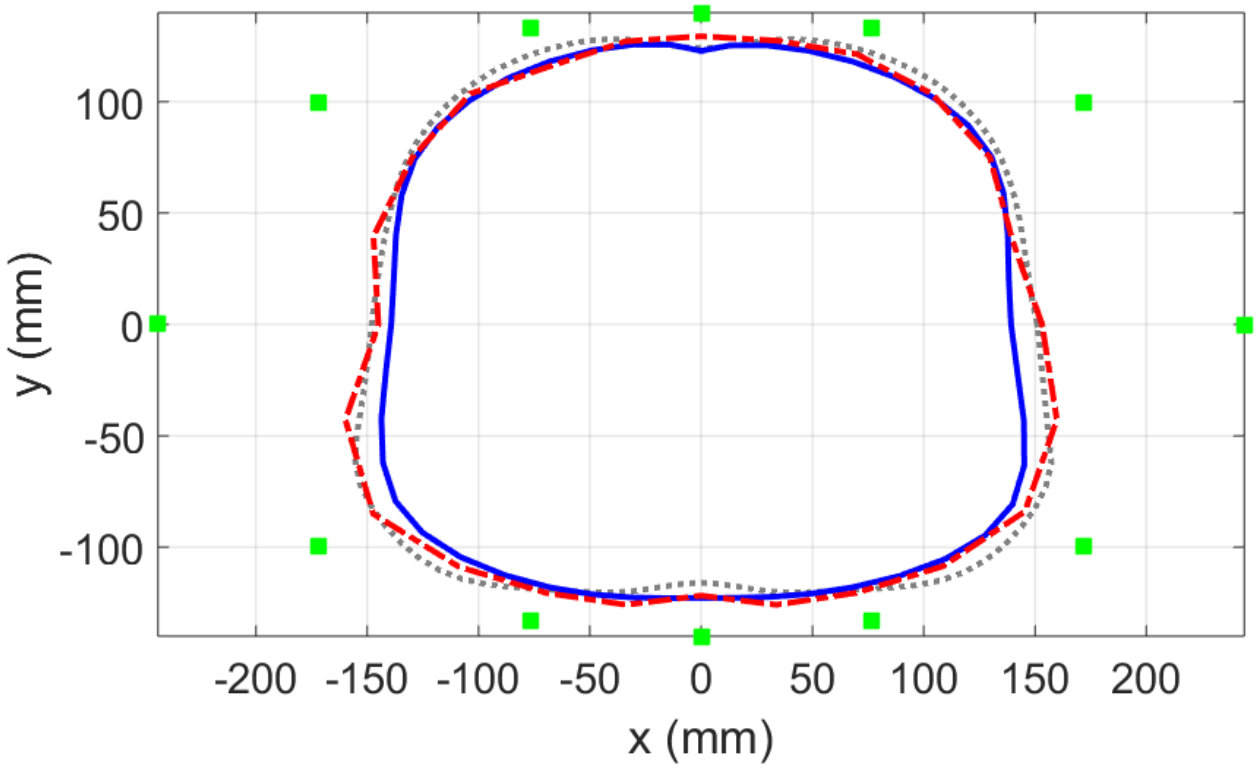

Fig. 7.10. Estimated torso boundary by matched-filter method (blue solid line), using 12 antennas and proposed method (red dashed line), using 24 virtual antennas extracted from 12 antennas. Grey dotted line shows the exact boundary of the torso.

Table 7.2. Boundary estimation errors using matched-filter and proposed methods

Method	Maximum error (mm)	Average error (mm)
Matched-filter	15.6	6.9
Proposed	7.9	3.7

To compare the effect of estimation errors generated from the proposed and the matched-filter methods, the estimated boundary using the matched-filter method is also applied to the same frequency-based imaging algorithm. The resultant image using 24 virtual antennas after applying the estimated boundary of matched-filter method is shown in Fig. 14. It is clear that introducing an inaccurate boundary to the imaging algorithm can lead to detection errors and ghost targets. Comparing the reconstructed images of the proposed method (Fig. 7.6 (c)) and the matched-filter method (Fig. 14) shows that using the proposed method can lead to more accurate detections with less ghost targets than using the matched-filter method on the same dataset.

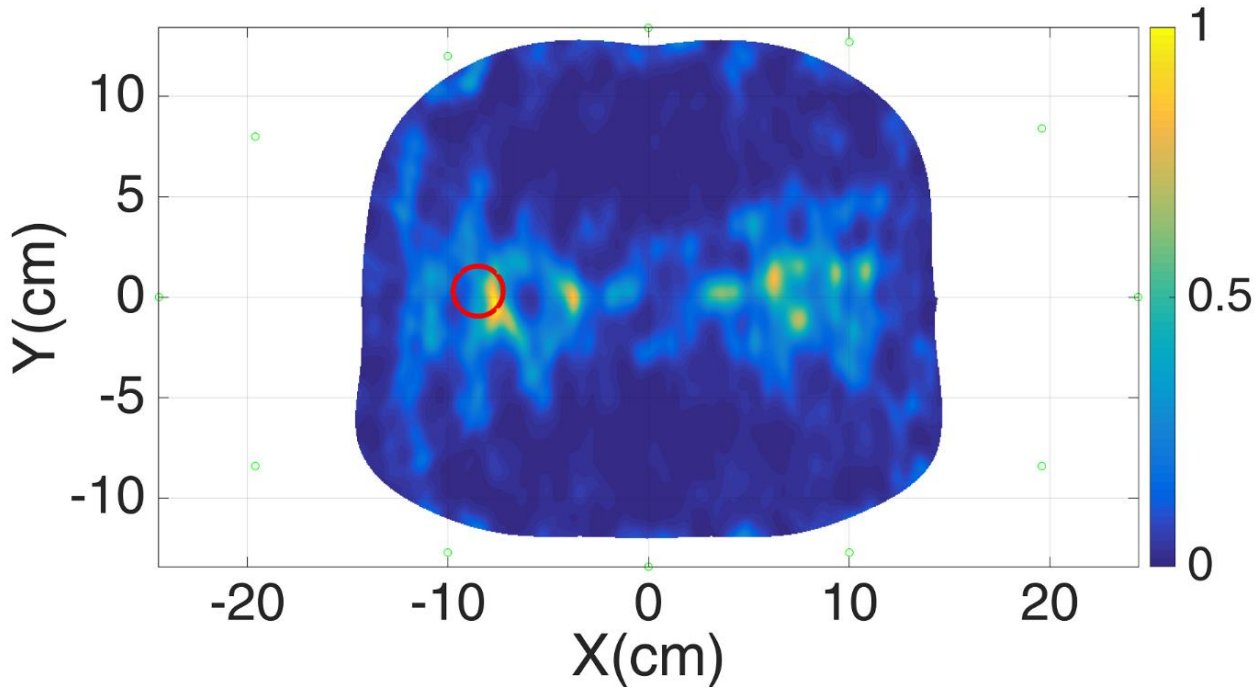

Fig. 7.11. Estimated torso boundary by matched-filter method (blue solid line), and proposed method (red dashed line). Grey dotted line shows the exact boundary of the torso.

7.4 Summary

A boundary identification method of an imaged object in microwave medical imaging has been introduced. It utilizes the variations in the resonant frequency of the imaging antennas with the distance from the imaged object to estimate its location and boundaries. For more accurate estimation, the virtual antenna array concept is integrated with the distance estimation function to create a uniform boundary estimation across the entire object's circumference. The proposed method has been successfully verified via simulations and experiments on healthy human subjects in a torso imaging system. It has also been shown that the proposed method is more accurate than existing time-domain based methods. The proposed method can estimate the boundary of the imaged object without using additional hardware in a fast manner using the same data acquired for imaging. The estimation of the three-dimensional surfaces of the imaged objects can be obtained by scanning the entire object using multiple rings of antennas.

8 CONCLUSION

In the previous chapters of this thesis, the outlined research aims in Section 1.3 are fulfilled by developing new techniques to overcome the shortcomings of existing microwave medical imaging algorithms. To that end, a comprehensive study of the current microwave imaging algorithms has been provided in Chapter 2. Study of the literature shows that the current techniques are developed based on the time-of-travel of electromagnetic wave, which makes those algorithms inaccurate in imaging of multilayer and heterogeneous imaged domains such as human head and torso. Other multi-stage techniques are also complex and time consuming. Therefore, a fast frequency-based processing and image reconstruction algorithm aimed for medical imaging purposes has been presented in Chapter 3.

The proposed algorithm consists of two steps. In the first step, the signal clutter originated from the skin reflections are mitigated and the second step of the algorithm involves using the first kind of first order Bessel function in the frequency domain to calculate power distributions inside the imaged domain in a fast and consistent way. The fast computation, simplicity, and stability of the results are the main advantages of the proposed algorithm over the conventional ones. The proposed approach has been validated using realistic simulation and experimental environments. It has been shown that using a limited number of frequency samples, which meets Nyquist limit, can successfully detect abnormalities in the human body. The proposed quasi-real-time imaging technique needs less than two seconds to generate an image by using a general-purpose computer. It has also been shown that the proposed frequency domain method is faster, more accurate with better clutter rejection capability than existing time-domain methods.

To find the best solution for the clutter removal stage, a detailed study of existing clutter removal techniques has been performed in Chapter 4. The different clutter removal techniques have been

modified for multistatic frequency-based imaging to address the time-overlap problem of those methods. Based on the explored performance of different methods in the frequency domain, a hybrid technique, which combines the benefits of average subtraction and entropy-based filtering methods, has been proposed. In that method, the average value of the multistatic scattered signals was subtracted from them at each frequency sample to remove late-stage clutters, whereas an entropy-based method was applied to mitigate early-stage strong clutters. The performance of the proposed method has been tested on realistic head phantom. It has been shown that the proposed hybrid method can effectively remove the clutter and ghost targets by improving the performance of the adopted methods in the time domain.

For a better performance of the imaging algorithm and in order to overcome the problem of limited number of antennas in multistatic measurement setups, the concept of virtual antenna array to increase the effective number of antenna elements has been proposed in Chapter 5. In this regard, a spatial interpolator has been designed to predict the received signals at the location of the virtual-elements using the recorded signals by a limited number of real antennas. Consequently, the virtual-array signals were processed by the proposed frequency-based-imaging algorithm to produce more accurate detections. Using quantitative metrics, it has been shown that the constructed images from the extended virtual-array are more accurate than the images created only from the real antennas. It has been also shown that a virtual-array that has twice the number of elements of the real array, which meet the minimum limit of degree-of-freedom of the problem, is enough to generate an accurate image with optimised computational resources. In comparison with existing correlation-based methods, the presented approach provided more accurate images.

Microwave-based imaging techniques, including the proposed frequency-domain algorithm in Chapter 3, require the dielectric properties of the imaged object as a priori information. To enhance the performance of the imaging algorithm and in order to make it useful for realistic scenarios, in which the dielectric properties of the imaging domain is unknown, a technique to determine the effective complex permittivity seen by each imaging antenna across the used frequency band of a multistatic imaging domain has been presented in Chapter 6. The method uses spatial statistical techniques to model the complex permittivity of the imaging domain as a function of scattering parameters. The proposed method does not require any predefined gap between the antennas and the imaged object, nor does it need the imaged object to be cantered within the imaging domain. Also, the method does not need to know boundaries of the imaged object. The proposed method has been tested on an elliptical shaped imaging domain to simulate a realistic scenario in which the distance between the antennas and the imaged object, such as the human torso, is not uniform. The

results demonstrated significant improvements in image quality and detection accuracy compared to conventional average-permittivity methods.

To further improve the performance of the frequency-based imaging algorithm, the boundaries of the imaged object has been introduced to the imaging algorithm in Chapter 7. Introducing the information about the boundaries of the imaged object into the imaging algorithms leads to an enhanced performance by reducing the reconstruction volume and hence computational time and improving the accuracy of the propagation models used in radar-based imaging techniques. However, such information about the antenna-imaged object distance in a clinical environment is an uncontrolled parameter, not exactly known and difficult, if not impossible, to measure. Review of previous literature on the boundary estimation methods revealed that existing methods use additional devices like laser sensors to accurately detect the surface of the imaged object, which complicates the imaging system. In addition, those methods suffer from patient movement/breathing during the two separate microwave and laser scans. Therefore, a method for boundary identification at the same time of imaging and using the same data captured for imaging has been presented in Section 7.1. The method uses the antennas' resonant frequency shifts due to the distance between the antenna and the imaged object. It has been shown that the proposed technique is quite fast, as it does not need additional devices for the accurate boundary estimation. The method has been tested via simulations and human trials using the torso imaging system. The included results in imaging a lung cancer case indicated that the accurate detection of the torso boundary improves microwave images.

For the future work, it is necessary to test the proposed methods on unhealthy cases. Therefore, clinical prototypes for the microwave head and torso imaging systems of the UQ microwave research group are under construction. In the meanwhile, a more efficient implementation of the proposed imaging algorithm is being investigated. It is also required to extend the proposed methods to be used for 3D imaging. To that end, multilayer imaging of the imaged object using multiple antenna array rings across the third dimension of the imaged object is proposed. In that case, additional research is needed to find the required distance between any two scans. Finally, it is required to obtain an efficient method to interpolate the multiple scans to create 3D images.

9 REFERENCES

[1] P. Palmer, G. Hanson, and J. Honeyman-Buck, Diagnostic imaging in the community, a manual for clinics and small hospitals: Pan-American Health Organization World Health Organization, 2012.

[2] World Health Organization. Global Tuberculosis Report 2012. www.who.int/tb/publications/global_report/en/.

[3] B. Bouhemad, M. Zhang, Q. Lu, JJ. Rouby, Clinical review: Bedside lung ultrasound in critical care practice. *Crit. Care*, vol. 11, no. 1, pp. 205, 2007.

[4] N.D. Zasler, D.I. Katz, and R.D. Zafonte, *Brain Injury Medicine: Principle and Practice*, 2nd ed., New York, NY: Demos Medical, 2013.

[5] L. E. Larsen and J. H. Jacobi, "Microwave Scattering Parameter Imaging of an Isolated Canine Kidney," *Medical Physics*, vol. 6, pp. 394–403, 1979.

[6] L. Jofre, M. S. Hawley, A. Broquetas, E. de los Reyes, M. Ferrando and A. R. Elias-Fuste, "Medical imaging with a microwave tomographic scanner," IEEE Transactions on Biomedical Engineering, vol. 37, no. 3, pp. 303-312, March 1990.

[7] S. Y. Semenov, R. H. Svenson, A. E. Boulyshev, A. E. Souvorov, V. Y. Borisov, Y. Sizov, A. N. Starostin, K. R. Dezern, G. P. Tatsis and V. Y. Baranov, "Microwave Tomography: Two-Dimensional System for Biomedical Imaging," *IEEE Trans. Biomed. Eng.*, vol. 43, pp. 869–877, Sep. 1996.

[8] S. Y. Semenov, R. H. Svenson, A. E. Boulyshev, A. E. Souvorov, A. G. Nazarov, Y. E. Sizov, V. G. Posukh, A. Pavlovsky, P. N. Repin and G. P. Tatsis, "Spatial Resolution of Microwave Tomography for Detection of Myocardial Ischemia and Infarction Experimental Study on Two-Dimensional Models," *IEEE Trans. Microwave Theory Tech*., vol. 48, pp. 538–544, Apr. 2000.

[9] P. M. Meaney, M. W. Fanning, D. Li, S. P. Poplack and K. D. Paulsen, "A Clinical Prototype for Active Microwave Imaging of the Breast," *IEEE Trans. Microwave Theory Tech*., vol. 48, pp. 1841–1853, Nov. 2000.

[10] D. Andreuccetti, R. Fossi and C. Petrucci: "An Internet resource for the calculation of the dielectric properties of body tissues in the frequency range 10 Hz - 100 GHz". Website at http://niremf.ifac.cnr.it/tissprop/. IFAC-CNR, Florence (Italy), 1997. Based on data published by C. Gabriel et al. in 1996.

[11] M. Lazebnik, D. Popovic, L. McCartney, C. B. Watkins, M. J. Lindstrom, J. Harter, S. Sewall, T. Ogilvie, A. Magliocco, T. M. Breslin, W. Temple, D. Mew, J. H. Booske, M. Okoniewski, and S. C. Hagness, "A large-scale study of the ultrawideband microwave dielectric properties of normal, benign and malignant breast tissues obtained from cancer surgeries," *Physics in Medicine and Biology*, vol. 52, no. 20, pp. 6093–6115, 2007.

[12] T. M. Grzegorczyk, P. M. Meaney, P. A. Kaufman, R. M. diFlorio-Alexander and K. D. Paulsen, "Fast 3-D Tomographic Microwave Imaging for Breast Cancer Detection," in *IEEE Transactions on Medical Imaging*, vol. 31, no. 8, pp. 1584-1592, Aug. 2012.

[13] W. C. Chew and J. H. Lin, "A frequency-hopping approach for microwave imaging of large inhomogeneous bodies," IEEE Microw. Guided Wave Lett. , vol. 5, no. 12, pp. 439–441, Dec. 1995.

[14] A. Fhager, P. Hashemzadeh, and M. Persson, "Reconstruction quality and spectral content of an electromagnetic time-domain inversion algorithm," *IEEE Transactions on Biomedical Engineering*, vol. 53, no. 8, pp. 1594–1604, 2006.

[15] M. Jalilvand, W. Chuanren, J. Schmid, and T. Zwick, "Quantitative imaging of numerically realistic human head model using microwave tomography," *Electron. Lett.* , vol. 50, no. 4, pp. 255-256, Feb. 2014.

[16] S.Y. Semenov, "Microwave-tomographic imaging of the high dielectric-contrast objects using different image-reconstruction approaches," *IEEE Trans. Microw. Theory Techn.*, vol. 53, no. 7, pp. 2284 – 2294, Jul. 2005.

[17] A.H. Golnabi, P.M. Meaney, and K.D. Paulsen, "Tomographic Microwave Imaging with Incorporated Prior Spatial Information," *IEEE Trans. Microw. Theory Techn.*, vol. 61, no. 5, pp. 2129-2136, May 2013.

[18] Q. H. Liu, Z. Q. Zhang, T. Wang, J.A. Bryan, G.A. Ybarra, L.W. Nolte, and W.T. Joines, "Active microwave imaging. I. 2-D forward and inverse scattering methods," *IEEE Trans. Microw. Theory Techn.*, vol. 50, no. 1, pp. 123-133, Jan. 2002.

[19] A. E. Souvorov et al., "Microwave tomography: a two-dimensional Newton iterative scheme," *IEEE Trans. Microw. Theory Techn.*, vol. 46, no. 11, pp. 1654-1659, Nov 1998.

[20] P. Meaney, E. Demidenko, N. Yagnamurthy, D. Li, M. Fanning, and K. Paulsen, "A two-stage microwave image reconstruction procedure for improved internal feature extraction," Medical Physics, vol. 28, no. 11, pp. 2358–2369, 2001.

[21] J. De Zaeytijd, A. Franchois, C. Eyraud, and J.-M. Geffrin, "Full-wave three-dimensional microwave imaging with a regularised Gauss-Newton method – theory and experiment," IEEE Transactions on Antennas and Propagation, vol. 55, no. 11, pp. 3279–3292, 2007.

[22] G. Bozza, C. Estatico, A. Massa, M. Pastorino, and A. Randazzo, "Short-range image-based method for the inspection of strong scatterers using microwaves," IEEE Transactions on Instrumentation and Measurement, vol. 56, no. 4, pp. 1181–1188, 2007.

[23] H. Harada, D. J. N. Wall, T. Takenaka, and M. Tanaka, "Conjugate gradient method applied to inverse scattering problem," IEEE Trans. Antennas Propag., vol. 43, no. 8, pp. 784–792, Aug. 1995.

[24] S. Caorsi, A. Massa, and M. Pastorino, "A computational technique based on a real-coded genetic algorithm for microwave imaging purposes," IEEE Trans. Geosci. Remote Sens., vol. 38, no. 4, pp. 1697–1708, Jul. 2000.

[25] L. Guo and A. M. Abbosh, "Optimisation-Based Confocal Microwave Imaging in Medical Applications," in *IEEE Trans. Antennas Propag.*, vol. 63, no. 8, pp. 3531-3539, Aug. 2015.

[26] P. Rocca, M. Benedetti, M. Donelli, D. Franceschini, and A. Massa, "Evolutionary Optimisation as applied to inverse problems," Inverse Probl. , vol. 25, pp. 1–41, 2009.

[27] W. C. Chew and Y. M. Wang, "Reconstruction of two-dimensional permittivity distribution using the distorted Born iterative method," *IEEE Trans. Med. Imag.*, vol. 9, no. 2, pp. 218–225, Jun. 1990.

[28] L. Guo and A. M. Abbosh, "Microwave Imaging of Nonsparse Domains Using Born Iterative Method With Wavelet Transform and Block Sparse Bayesian Learning," IEEE Transactions on Antennas and Propagation, vol. 63, no. 11, pp. 4877-4888, Nov. 2015.

[29] R. G. Baraniuk, "Compressive sensing," IEEE Signal Process. Mag., vol. 24, no. 4, pp. 118–124, Jul. 2007.

[30] P. M. van den Berg and R. E. Kleinman, "A contrast source inversion method," Inverse Problems, vol. 13, no. 6, pp. 1607–1620, 1997.

[31] H. Feng, V. Galdi, and D. A. Castanon, "An object-based contrast source inversion method for homogeneous targets," Subsurface Sensing Technologies and Applications, vol. 4, no. 4, pp. 355–374, 2003.

[32] A. Abubakar, S. Semenov, V. G. Posukh, and P. M. van den Berg, “Application of the multiplicative regularised contrast source inversion method to real biological data,” Proceedings of the IEEE MTT-S International Microwave Symposium, 2005, vol. 2005, pp. 1319–1322, 2005.

[33] D. S. Shumakov; N. K. Nikolova, “Fast Quantitative Microwave Imaging With Scattered-Power Maps,” IEEE Transactions on Microwave Theory and Techniques, vol. PP, no. 99, pp.1-11.

[34] M. Pastorino, Microwave Imaging. Hoboken: J. Wiley, 2010.

[35] E. Fear and M. Stuchly, “Microwave system for breast tumor detection,” IEEE Microwave and Guided Wave Letters, vol. 9, no. 11, pp. 470–472, 1999.

[36] E. C. Fear, X. Li and S. C. Hagness, “Confocal Microwave Imaging for Breast Cancer Detection: Localisation of Tumors in Three Dimensions,” *IEEE Trans. Biomed. Eng*., vol. 49, pp. 812–822, Aug. 2002.

[37] X. Li, S.C. Hagness, “A confocal microwave imaging algorithm for breast cancer detection,” *IEEE Microw. Compon. Lett., IEEE* , vol. 11, no. 3, pp. 130-132, March 2001.

[38] E. C. Fear, J. Bourqui, C. Curtis, D. Mew, B. Docktor and C. Romano, "Microwave Breast Imaging With a Monostatic Radar-Based System: A Study of Application to Patients," in *IEEE Trans. Microw. Theory Techn*., vol. 61, no. 5, pp. 2119-2128, May 2013.

[39] R. Nilavalan, A. Gbedemah, I.J. Craddock, X. Li, and S.C. Hagness, “Numerical investigation of breast tumour detection using multistatic radar,” Electron. Lett., vol. 39, no. 25, pp. 1787-1789, Dec. 2003.

[40] J. Bond, X. Li and S. C. Hagness, “Microwave Imaging via Space-Time Beamforming for Early Detection of Breast Cancer,” *IEEE Trans. Antennas Propagat*., vol. 51, pp. 1690–1705, Aug. 2003.

[41] X. Li, S. K. Davis, S. C. Hagness, D. W. van der Weide and B. D. Van Veen, “Microwave Imaging via Space Time Beamforming: Experimental Investigation of Tumor Detection in Multilayer Breast Phantoms,” *IEEE Trans. Microwave Theory Tech*., vol. 52, pp. 1856–1865, Aug. 2004.

[42] M. O'Halloran, E. Jones, M. Glavin, “Quasi-Multistatic MIST Beamforming for the Early Detection of Breast Cancer,” *IEEE Trans. Biomed. Eng*., vol. 57, no. 4, pp. 830-840, 2010.

[43] Y. Xie, B. Guo, L. Xu, J. Li, and P. Stoica, “Multistatic Adaptive Microwave Imaging for Early Breast Cancer Detection,” *IEEE Trans. Biomed. Eng*., vol. 53, no. 8, pp. 1647-1657, 2006.

[44] M. Klemm, I. Craddock, J. Leendertz, A. Preece, and R. Benjamin, “Radar-based breast cancer detection using a hemispherical antenna array—Experimental results,” IEEE Trans. Antennas Propag., vol. 57, no. 6, pp. 1692–1704, Jun. 2009.

[45] M. Klemm, J. A. Leendertz, D. Gibbins, I. J. Craddock, A. Preece, and R. Benjamin, "Microwave radar-based differential breast cancer imaging: Imaging in homogeneous breast phantoms and low contrast scenarios," *IEEE Trans. Antennas Propag.*, vol. 58, no. 7, pp. 2337–2344, Jul. 2010.

[46] D. Byrne and I. J. Craddock, "Time-Domain Wideband Adaptive Beamforming for Radar Breast Imaging," *IEEE Trans. Antennas Propagat*., vol. 63, no. 4, pp. 1725-1735, April 2015.

[47] M. Persson, A. Fhager, H.D. Trefna, Y. Yinan T. McKelvey, G. Pegenius, J.-E Karlsson, and M. Elam, "Microwave-Based Stroke Diagnosis Making Global Prehospital Thrombolytic Treatment Possible," *IEEE Trans. Biomed. Eng*., vol. 61, no. 11, pp. 2806-2817, Nov. 2014.

[48] N. Ghavami, G. Tiberi, D.J. Edwards, and A. Monorchio, "Microwave Imaging Through a Mode-Matching Bessel Functions Procedure," *IEEE Trans. Microw. Theory Techn.*, vol. 61, no.8, pp. 2753-2760, Aug. 2013.

[49] M. Chiappe and G. L. Gragnani, "An analytical approach to the reconstruction of the radiating currents in inverse electromagnetic scattering," *Microw. Opt. Technol. Lett.*, vol. 49, no. 2, pp. 354-360, 2007.

[50] R. Solimene and A. Cuccaro, "Front Wall Clutter Rejection Methods in TWI," *IEEE Geosci. Remote Sens. Lett.,* vol. 11, no. 6, pp. 1158-1162, Jun. 2014.

[51] A. Zadehgol and A.C. Cangellaris, "Isotropic Spatial Filters for Suppression of Spurious Noise Waves in Sub-Gridded FDTD Simulation," *IEEE Trans. Antennas Propag.*, vol. 59, no. 9, pp. 3272-3279, Sept. 2011.

[52] T. Tu, C. Chen and C. Chang, "A noise subspace projection approach to target signature detection and extraction in an unknown background for hyperspectral images," *IEEE Trans. Geosci. Remote Sens.*, vol. 36, no.1, pp. 171-181, Jan. 1998.

[53] S. Mustafa, B. Mohammed, and A.M. Abbosh, "Novel Preprocessing Techniques for Accurate Microwave Imaging of Human Brain," *IEEE Antennas Wireless Propag. Lett.*, vol. 12, no. 1, pp. 460-463, 2013.

[54] P. Kosmas, C. Rappaport, "Time reversal with the FDTD method for microwave breast cancer detection," IEEE Trans. Microw. Theory Techn., vol. 53, no. 7, pp. 2317-2323, July 2005.

[55] A. Ishimaru, "Wave Propagation and Scattering in Random Media," New York: Academic Press, 1978.

[56] R. Kress, "Inverse obstacle scattering with modified or reduced data," In Scattering Theory and Biomedical Engineering Modelling and Applications, Dassios et al., ed. Singapore: World Scientific, 2000, pp. 10-18.

[57] R.P. Millane and J.L. Eads, “Polynomial approximations to Bessel functions,” IEEE Trans. Antennas Propag., vol.51, no.6, pp.1398-1400, June 2003.

[58] A.T. Mobashsher and A.M. Abbosh, “Slot-Loaded Folded Dipole Antenna With Wideband and Unidirectional Performance for L-Band Applications,” IEEE Antennas Wireless Propag. Lett., vol. 13, no. 1, pp. 798-801, 2014.

[59] A. T. Mobashsher and A.M. Abbosh, “Three-Dimensional Human Head Phantom with Realistic Electrical Properties and Anatomy, IEEE Antennas Wireless Propag. Lett., vol. 13, no. 1, pp. 1401-1404, 2014.

[60] A.T. Mobashsher, A.M. Abbosh, and Y. Wang, “Microwave System to Detect Traumatic Brain Injuries Using Compact Unidirectional Antenna and Wideband Transceiver With Verification on Realistic Head Phantom,” *IEEE Trans. Microw. Theory Techn.,* vol. 62, no. 9, pp. 1826-1836, Sept. 2014.

[61] S.A. Rezaeieh, A. Zamani, A.M. Abbosh, “Three Dimensional Wideband Antenna for Head Imaging System with Performance Verification in Brain Cancer Detection,” *IEEE Antennas Wireless Propag Lett*, Available IEEE Xplore, 2014

[62] http://www.kyotokagaku.com/products/detail03/pdf/ph-1_catalog.pdf, accessed March 2015.

[63] M. Sarafianou, I.J. Craddock, T. Henriksson, “Towards Enhancing Skin Reflection Removal and Image Focusing Using a 3-D Breast Surface Reconstruction Algorithm,” *IEEE Trans. Antennas Propag.*, vol. 61, no. 10, pp. 5343-5346, Oct. 2013.

[64] Z. Wanjun, F. Chin, “Entropy-Based Time Window for Artifact Removal in UWB Imaging of Breast Cancer Detection,” *IEEE Signal Process. Lett.*, vol. 13, no. 10, pp. 585-588, Oct. 2006.

[65] Y. Zhang, P. Candra, W. Guoan, X. Tian, “2-D Entropy and Short-Time Fourier Transform to Leverage GPR Data Analysis Efficiency,” *IEEE Trans. Instrum. Meas.*, vol. 64, no. 1, pp. 103-111, Jan. 2015.

[66] M.A. Elahi, A. Shahzad, M. Glavin, E. Jones, M. O'Halloran, “Hybrid Artifact Removal for Confocal Microwave Breast Imaging,” *IEEE Antennas Wireless Propag. Lett.*, vol. 13, pp.149-152, 2014.

[67] M. Fallahpour, J. T. Case, M. T. Ghasr, R. Zoughi, “Piecewise and Wiener Filter-Based SAR Techniques for Monostatic Microwave Imaging of Layered Structures,” *IEEE Trans. Antennas Propag.*, vol. 62, no. 1, pp. 282-294, Jan. 2014.

[68] A. Yamani, “A novel pulse-echo technique for medical three-dimensional imaging,” *IEEE Trans. Med. Imag.*, vol. 16, no. 6, pp. 938-942, Dec. 1997.

[69] Y. S. Yoon and M. Amin, “Spatial filtering for wall clutter mitigation in through-the-wall radar imaging,” *IEEE Trans. Geosci. Remote Sens*., vol. 47, no. 9, pp. 3192–3208, Sep. 2009.

[70] R.G Baraniuk, P. Flandrin, A.J.E.M. Janssen, O.J.J. Michel, "Measuring time-frequency information content using the Renyi entropies," *IEEE Trans. Inf. Theory*, vol. 47, no. 4, pp. 1391-1409, May 2001.

[71] R.K. Amineh, J.J. McCombe, A. Khalatpour, N.K. Nikolova, "Microwave Holography Using Point-Spread Functions Measured With Calibration Objects," *IEEE Trans. Instrum. Meas.*, vol. 64, no. 2, pp. 403-417, Feb. 2015.

[72] A. Nevis, "Image characterization and target recognition the surf zone environment," *Proc. of SPIE*, Vol. 2765, 46-58, 1996.

[73] F. Gao, B. D. Van Veen, and S. C. Hagness, "Sensitivity of the distorted born iterative method to the initial guess in microwave breast imaging," in *IEEE Trans. Antennas Propag.*, vol. 63, no. 8, pp. 3540–3547, 2015.

[74] P. M. Woodward, D. W. Fry and W. Higinbotham, "Probability and Information Theory with Applications to Radar," Norwood, MA: Artech House, 1953.

[75] O. M. Bucci, and T. Isernia, "Electromagnetic inverse scattering: Retrievable information and measurement strategies," *Radio Science*, vol. 32, no. 6, pp. 2123-2137, Nov-Dec, 1997.

[76] O. M. Bucci, L. Crocco, R. Scapaticci, and G. Bellizzi, "On the Design of Phased Arrays for Medical Applications," *Proceedings of the IEEE*, vol. 104, no. 3, pp. 633-648, Mar, 2016

[77] R. J. Mailloux, *Phased Array Antenna Handbook*. Norwood, MA: Artech House, 1994.

[78] L.I. Vaskelainen, "Virtual array synthesis method for planar array antennas," in *IEEE Trans. Antennas Propag.*, vol. 46, no. 3, pp. 391-396, 1998.

[79] P. Hyberg, M. Jansson, B. Ottersten, "Array interpolation and bias reduction," in *IEEE Trans. Signal Processing*, vol. 52, no. 10, pp. 2711-2720, 2004.

[80] H. Kuoye, B. Qian. T. Weixian, W. Yanping, H. Wen, "Statistical Analysis of the Effects of Virtual Element Position Errors on Airborne Down-Looking LASAR 3-D Imaging," in *Geoscience and Remote Sensing Letters, IEEE*, vol. 12, no. 9, pp. 1888-1892, 2015.

[81] K. E. Browne, R. J. Burkholder and J. L. Volakis, "Through-Wall Opportunistic Sensing System Utilising a Low-Cost Flat-Panel Array," *IEEE Trans. on Antennas Propag.*, 59(3): 859-868, March 2011.

[82] G. L. Charvat, L. C. Kempel, E. J. Rothwell, et al, "A Through-Dielectric Ultrawideband (UWB) Switched-Antenna-Array Radar Imaging System," *IEEE Trans. on Antennas Propag.*, 60(11): July 2012.

[83] B. D. Rao and K. V. S. Hari, "Performance Analysis of Root-MUSIC," *IEEE Trans. Acoustics Speech and Signal Processing*, 1989.

[84] B. Friedlander, A. Weiss, “Direction finding using spatial smoothing with interpolated arrays,” *IEEE Trans. Aero. Elec. Sys.*, vol. 28 no. 2, pp. 574-587, 1992.

[85] Y.-S. Yoon and M. G. Amin, “High-resolution through-the-Wall radar imaging using beamspace MUSIC,” *IEEE Trans. Antennas Propag.*, vol. 56, no. 6, pp. 1763–1774, Jun. 2008

[86] D. Pinchera, M.D. Migliore, G. Panariello, “A Virtual Subarray Architecture for Imaging Radar,” in *IEEE Trans. Antennas and Propagation*, vol. 62, no. 10, pp. 5171-5179, 2014.

[87] J. P. C. Kleijnen, “Kriging Metamodeling in Simulation: A Review,” *European Journal of Operation Research*, vol. 192, no. 3, 2009, pp. 707-716.

[88] L. Lebensztajn, C.A.R. Marretto, M.C. Costa, J.L. Coulomb, “Kriging: a useful tool for electromagnetic device Optimisation,” in *IEEE Trans. Magnetics*, vol. 40, no. 2, pp. 1196-1199, 2004.

[89] S. Koziel, A. Bekasiewicz, I. Couckuyt, T. Dhaene, "Efficient Multi-Objective Simulation-Driven Antenna Design Using Co-Kriging," *IEEE Trans. Antennas Propag.*, vol. 62, no. 11, pp. 5900-5905, Nov. 2014.

[90] Tzong-Dar Wu, K. S. Chen, J. Shi and A. K. Fung, "A transition model for the reflection coefficient in surface scattering," *IEEE Trans. Geosci. Remote Sens.*, vol. 39, no. 9, pp. 2040-2050, Sep 2001.

[91] A. Papritz, A. Stein, "Spatial prediction by linear kriging", in *Spatial Statistics for Remote Sensing*, vol. 1, A. Stein, F. Van Der Meer, and B. Gorte Ed. Dordrecht: Springer Netherlands, 2002, pp. 83-113.

[92] C. K. I. Williams, “Prediction with Gaussian Processes: From Linear Regression to Linear Prediction and Beyond,” in Learning in Graphical Models, vol. 89, M.I. Jordan, Ed. Dordrecht: Springer Netherlands, 1998, pp. 599–621

[93] Slawomir Koziel, L. Leifsson, and Xin-She Yang, Simulation-Driven Design Optimisation and Modeling for Microwave Engineering. Imperial College Press: London, 2013.

[94] F. Wang and K. Sarabandi, “A physics-based statistical model for wave propagation through foliage,” IEEE Trans. Antennas Propag., vol. 55, no. 3, pp. 958–968, Mar. 2007

[95] Abramowitz, M. and Stegun, I. A. (Eds.). Handbook of Mathematical Functions with Formulas, Graphs, and Mathematical Tables, 9th printing. New York: Dover, pp. 878-879 and 883, 1972.

[96] L. Zhou, C. Huang, and Y. Su, “A fast back-projection algorithm based on cross correlation for GPR imaging,” IEEE Geosci. Remote Sens. Lett., vol. 9, no. 2, pp. 228–232, Mar. 2012.

[97] K. K. Knaell and G. P. Cardillo, "Radar tomography for the generation of three-dimensional images," in *IEE Proceedings - Radar, Sonar and Navigation*, vol. 142, no. 2, pp. 54-60, Apr 1995.

[98] K. Pearson, “Notes on regression and inheritance in the case of two parents," Proceedings of the Royal Society of London, vol. 58, pp. 240–242, June 1895.

[99] K. K. M. Chan, A. E. C. Tan, L. Li, and K. Rambabu, “Material Characterization of Arbitrarily Shaped Dielectrics Based on Reflected Pulse Characteristics,” *IEEE Trans. Microw. Theory Techn.*, vol. 63, no. 5, pp. 1700-1709, May, 2015.

[100] J. Bourqui and E. C. Fear, “System for Bulk Dielectric Permittivity Estimation of Breast Tissues at Microwave Frequencies,” *IEEE Trans. Microwave Theory Techn.*, vol. 64, pp. 3001-3009, 2016.

[101] D. W. Winters, E. J. Bond, B. D. Van Veen and S. C. Hagness, “Estimation of the Frequency-Dependent Average Dielectric Properties of Breast Tissue Using a Time-Domain Inverse Scattering Technique,” in *IEEE Trans. Antennas Propag.*, vol. 54, no. 11, pp. 3517-3528, Nov. 2006.

[102] M. Sarafianou et al., "MUSIC processing for permittivity estimation in a Delay-and-Sum imaging system," *2013 7th European Conference on Antennas and Propagation (EuCAP)*, Gothenburg, 2013, pp. 839-842.

[103] B. J. Mohammed, K. S. Bialkowski and A. M. Abbosh, “Radar-based time-domain head imaging using database of effective dielectric constant,” in *Electronics Letters*, vol. 51, no. 20, pp. 1574-1576, 10 1 2015.

[104] B. Lavoie, M. Okoniewski, E. Fear, “Estimating the Effective Permittivity for Reconstructing Accurate Microwave-Radar Images,” *PLoS ONE*, vol. 11, no. 9, 2016.

[105] S. Salman, D. Psychoudakis and J. L. Volakis, “Determining the Relative Permittivity of Deep Embedded Biological Tissues,” in *IEEE Antennas Wireless Propag. Lett.*, vol. 11, pp. 1694-1697, 2012.

[106] M. A. Islam, A. Kiourti and J. L. Volakis, “A Novel Method of Deep Tissue Biomedical Imaging Using a Wearable Sensor,” in *IEEE Sensors J.*, vol. 16, no. 1, pp. 265-270, Jan.1, 2016.

[107] N. Cressie, “Statistics for Spatial Data,” in *Statistics for Spatial Data, Revised Edition*, Hoboken: Wiley, 1993.

[108] A. C. Aitken, “On Least-squares and Linear Combinations of Observations,” presented in *Proceedings of the Royal Society of Edinburgh*, no. 55, pp. 42–48. 1934.

[109] L. Tsang, K. H. Ding, S. Huang and X. Xu, “Electromagnetic Computation in Scattering of Electromagnetic Waves by Random Rough Surface and Dense Media in Microwave Remote Sensing of Land Surfaces,” in *Proc. IEEE*, vol. 101, no. 2, pp. 255-279, Feb. 2013.

[110] S. A. Rezaeieh, A. Zamani, K. S. Bialkowski, and A. M. Abbosh, "Novel Microwave Torso Scanner for Thoracic Fluid Accumulation Diagnosis and Monitoring," *Nature, Scientific Reports*, March 2017.

[111] V. Clemson, Y. Tang, J. Pyne, and R. Unal, “Efficient methods for sensitivity analysis,” *System Dynamics Review*, no. 11, pp. 31-49, 1995.

[112] T. C. Williams, J. Bourqui, T. R. Cameron, M. Okoniewski and E. C. Fear, “Laser Surface Estimation for Microwave Breast Imaging Systems,” in *IEEE Transactions on Biomedical Engineering*, vol. 58, no. 5, pp. 1193-1199, May 2011.

[113] T. Sakamoto and T. Sato, “A target shape estimation algorithm for pulse radar systems based on boundary scattering transform,” *IEICE Trans. Communun.*, vol. E87-B, no. 5, pp. 1357–1365, May 2004.

[114] D. W. Winters, J. D. Shea, E. L. Madsen, G. R. Frank, B. D. Van Veen and S. C. Hagness, “Estimating the Breast Surface Using UWB Microwave Monostatic Backscatter Measurements,” in *IEEE Transactions on Biomedical Engineering*, vol. 55, no. 1, pp. 247-256, Jan. 2008.

[115] C. A. Balanis, Antenna Theory Analaysis and Design, John Wiley & Sons, New York, NY, USA, 2nd edition, 1997.

10 APPENDICES

Appendix 1 142

APPENDIX 1

THE UNIVERSITY OF QUEENSLAND

Institutional Human Research Ethics Approval

Project Title:	Torso imaging using electromagnetic techniques
Chief Investigator:	Mr Ali Zamani, Dr Sasan Ahdi Rezaeieh
Supervisor:	Prof Amin Abbosh
Co-Investigator(s):	Dr Konstanty Bialkowski
School(s):	School of Biomedical Engineering
Approval Number:	2017000185
Granting Agency/Degree:	Endeavour Scholarship
Duration:	31st May 2019

Comments/Conditions:

- Application, 13/02/2017
- Protocol, 13/02/2017
- PICF, 13/02/2017

Note: if this approval is for amendments to an already approved protocol for which a UQ Clinical Trials Protection/Insurance Form was originally submitted, then the researchers must directly notify the UQ Insurance Office of any changes to that Form and Participant Information Sheets & Consent Forms as a result of the amendments, before action.

Name of responsible Committee:
University of Queensland Human Research Ethics Committee A
This project complies with the provisions contained in the *National Statement on Ethical Conduct in Human Research* and complies with the regulations governing experimentation on humans.

Name of Ethics Committee representative:
Professor Emerita Gina Geffen
Chairperson
University of Queensland Human Research Ethics Committee A
Registration: EC00456

G. Geffen

16/03/2017

Signature _____ Date _____